An investigation of the molecular properties of 1,1,1-trichloroethane using laser spectroscopy

M.B. Mametja

20971966

Dissertation submitted in partial fulfilment of the requirements for the degree *Master of Science* at the Potchefstroom campus of the North-West University

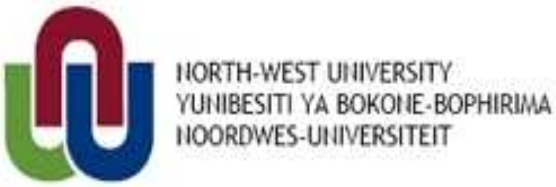

Supervisor: **Prof. C. A. Strydom**

Co-Supervisor: **Dr. A. du Plessis**

November 2008

Declaration

I……, hereby declare that the work contained in this dissertation is my own original work and that I have not submitted it at any other university.

Signature……..

Date……..

Abstract

FT-IR and FT-Raman spectra of 1,1,1-trichlorethane (CH_3CCl_3) were recorded in the regions 400 – 3500 cm^{-1} and 200 – 3500 cm^{-1} respectively. The observed vibrational numbers were analysed and assigned to different normal modes of vibration of the molecule. Density functional calculations were performed to support wavenumber assignment of the observed bands. The equilibrium geometry and harmonic wavenumbers of TCE were calculated with the DFT B3LYP method [Spartan, 2004]. The vibrational wavenumbers were compared with IR experimental data. The discrepancies between the calculated and observed spectra is that the rotational energy levels cause splitting or broadening of infrared absorbance peaks and this refinement was not included in the calculations using Spartan [2004]. Ultraviolet-visible absorption spectroscopy was used to determine the wavelength needed for excitation and ionization of TCE and it was confirmed that the absorption of energy by TCE is in the deep UV region.

The time of flight mass spectra of ion products formed from TCE were recorded after excitation by nanosecond and femtosecond laser pulses at various wavelengths and at various different conditions. The mass spectra obtained at different conditions with both lasers were compared in order to find information about ionization and dissociation of the molecule. The parent ion was not detected in either nanosecond or femtosecond experiments, probably due to the molecule being dissociated easily. The main difference between nanosecond and femtosecond laser pulse ionization of TCE is that more larger fragments are observed when using femtosecond laser pulses, due to ladder climbing being dominant, while ladder switching is dominant in the nanosecond regime.

Acknowledgements

I would like to thank the following people:

- Dr A. du Plessis and Prof C.A. Strydom, for their excellent supervision and guidance of this work and for the discussions which have contributed to the success of this project.
- Dr Hennie for many discussions about the experimental procedures and his patience.
- Mr Henk van Wyk for his help with operation of Nd:YAG and dye lasers.
- All my colleagues, particularly Brenda Pelle for continuous discussions we had about the experimental procedures of this work.
- Femtosecond science research group members who were always willing to help.
- My mother and Derick for their understanding and support.

This study was funded by National Laser Centre (NLC) at Council for Scientific and Industrial Research (CSIR) and National Research Foundation (NRF). The work formed part of a research project funded by the Pebble Bed Modular Reactor (PBMR) Pty Ltd.

Table of contents

Abbreviations

Symbols

TCE	1,1,1-Trichloroethane (CH_3CCl_3)
MTS	Methyltrichlorosilane (CH_3SiCl_3)
TATP	Triacetone triperoxide ($C_9H_8O_6$)
FTIR	Fourier Transform Infrared
IR	Infrared
NMR	Nuclear Magnetic Resonance
UV	Ultraviolet
UV-Vis	Ultraviolet-Visible
TOF	Time of Flight
TOF-MS	Time of Flight Mass Spectrometry/Spectrometer
DFT	Density Funtional Theory
HF	Hartree Fock
RHF	Restricted Hartree Fock
MP	Møller-Plesset perturbation theory
MM	Molecular Mechanics
MMFF	Merck Molecular Force Field
B3LYP	Becke 3-Parameter Lee Yang and Parr
STO	Slater-Type Orbital
LDA	Local Density Approximation
GC	Gradient Corrected
Nd:YVO4	Neodymium Doped Yttrium Vanadate
Nd:YAG	Neodymium Doped Yttrium Aluminium Garnet
BBO	β-Barium Borate

KDP	Potassium dihydrogen phosphate
OPA	Optical Parametric Amplifier
PBMR	Pebble Bed Modular Reactor, Pty Ltd
n	Number of molecules
h	Planck's constant
k	Calibration constant
v	frequency
λ	Lambda
μ	dipole moment
E	Energy of a photon
σ	sigma
π	pi
q	ion charge
N	Nitrogen
O	Oxygen
C	Carbon
H	Hydrogen
Cl	Chlorine
Ar	Argon
K	Potassium
Ti	Titanium
Cr	Chromium
N_2O	Nitrogen dioxide
NO	Nitrogen oxide
XeCl	Xenon chloride
KrF	Krypton Fluoride
XeF	Xenon Fluoride
ArF	Argon Fluoride

SiC	Silicon carbide
HCl	Hydrogen chloride (hydrochloric acid)
SiCl	Silicon chloride
CH	Carbon hydrogen
•OH	Hydroxyl
O_3	Ozone
He-Ne	Helium Neon
MgF_2	Magnesium Fluoride
CH_3CCl_3	1,1,1-Trichloroethane
$CHCl_3$	Trichloromethane (chloroform)
CH_3SiCl_3	Methyltrichlorosilane
CH_2Cl_2	Dichloroethene
CH_3Cl	Chloromethane
$CHFCl_2$	Dichloroflouromethane
Hg-Ar	Mercury Argon
DLaTGS	Deuterated L-alanine triglyrine sulphate
KBr	Potassium Bromide
InGaAs	Indium Gallium Arsenide
CaF_2	Calcium Fluoride

Units

amu	Atomic mass unit
µs	Microseconds
MHz	Mega hertz
Hz	Hertz
kHz	Kilo hertz
fs	Femtoseconds

ns	Nanoseconds
J	Joules
mJ	Milli Joules
µJ	Micro Joules
kPa	Kilo Pascal
eV	Electron volts
nm	Nanometre
cm	Centimetre
cm^{-1}	Per centimetre
µm	Micro metre
W	Watts
mW	Milli Watts
kW	Kilo watts
m	Meters
mm	Milli meters
kcal	Kilo Calories
kcal/mol	Kilo calories per mole
µm	Micro meter
m/z	Mass-to-charge ratios
K	Kelvin
V	Volts
°	Degree
Å	Angstrom

Chapter 1

Introduction

1.1. Aim of the study

The aim of this study is to improve our knowledge of the molecule 1,1,1-trichloroethane (CH_3CCl_3, abbreviated as TCE), and in particular its excitation, dissociation and ionization after laser irradiation. This information will be useful in future attempts to control these processes, using a technique called femtosecond laser pulse coherent control [Dantus and Lozovoy, 2004]. Additionally, this information may be useful in studies involving analytical detection of the molecule and its dissociation products, especially since this molecule has environmental relevance [Herbert *et al*., 1986].

TCE molecule is of interest here because it has a similar structure to methyltrichlorosilane (CH_3SiCl_3, abbreviated as MTS), which is the compound used in the chemical vapour deposition process of silicon carbide (SiC) onto the graphite layer of the Pebble Bed Modular Reactor (PBMR) kernel [ANON, 1999]. This dissertation forms part of a project aimed at the development of femtochemistry techniques, with the eventual aim being the potential improvement of PBMR processes [PBMR Technology Programme, 2008].

One such improvement involves the attempt to control the chemical vapour deposition process by means of which SiC is formed from MTS, in order to obtain selectively a specific structure of silicon carbide. This will result in an improved SiC coating and hence a safer PBMR nuclear energy process.

In order to improve our understanding of the molecular structure of the PBMR-relevant molecule MTS, the molecule TCE which has a similar structure as shown in figure 1.1, was chosen for comparative purposes and this molecule is the focus of this dissertation. A similar study has been undertaken in parallel to this study and focused on MTS [Pelle, 2008]. Some comparative results are included in this dissertation.

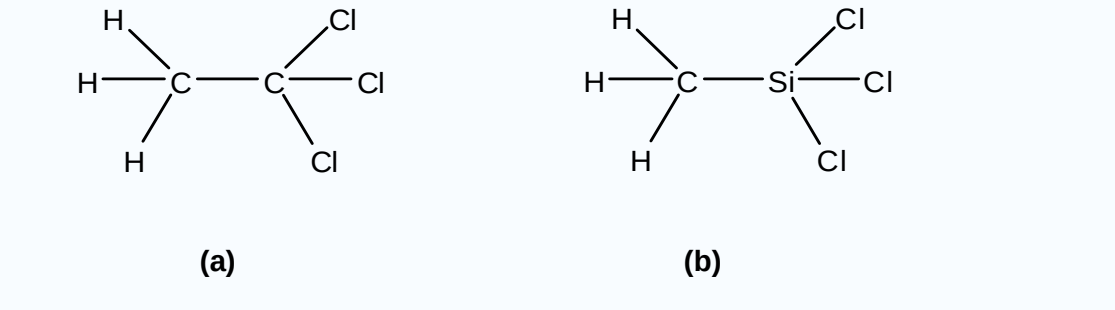

Figure 1.1: Molecular structure for (a) TCE and (b) MTS

Furthermore, since TCE is also known to be an ozone depleting substance and occurs in the upper atmosphere, studies of the photo-activation and subsequent decomposition thereof could benefit environmental research studies as well [Herbert *et al.*, 1986]. Most of TCE released into the environment remains in the atmosphere for long periods of time, even up to 6 years [Herbert *et al*., 1986]. TCE in air can travel to the ozone layer where it undergoes photolysis [McParland, 1995]. TCE will be oxidized, when entering the troposphere, to trichloroacetaldehyde by reaction with the free hydroxyl radicals produced by the action of solar UV light. The trichloroacetaldehyde is then further oxidized to trichloroacetic acid (scheme 1.1) [Muller *et al*., 1996]. In the stratosphere it is degraded by photochemical processes and liberates chlorine atoms. In water, degradation of TCE occurs via dehydrochlorination to hydrochloric acid and 1,1-dichloroethene. The 1,1-

dichloroethene hydrolysis to hydrochloric acid and ethanoic acid [Dobson, 1990]. The reaction rates are influenced by temperature and alkalinity [Dobson, 1990].

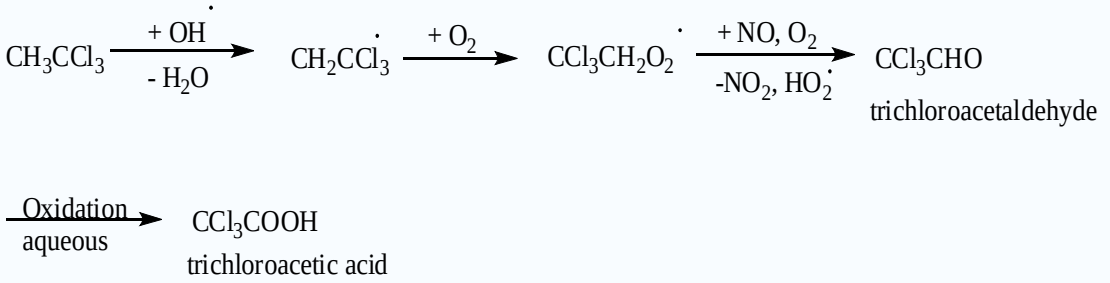

Scheme 1.1: Photo-oxidation of 1,1,1-trichloroethane [Muller *et al*., 1996]

Since TCE has appreciable tropospheric residence time, it is subjected to diffusion across the tropopause into the stratosphere [Gerkens and Franklin, 1989]. It transforms in the troposphere and during this transformation process approximately 15% migrates into the stratosphere where it is converted into chlorine atoms by short wavelength ultraviolet light. The chlorine atoms contribute to the degradation of the ozone layer [Gerkens and Franklin, 1989] as they react with the ozone molecules, taking up one of the oxygen atoms of an ozone molecule to form chlorine monoxide and ordinary molecular oxygen. The chlorine monoxide reacts further with oxygen and the net result is the depletion of ozone and atomic oxygen (scheme 1.2) [CIESIN, 1997]:

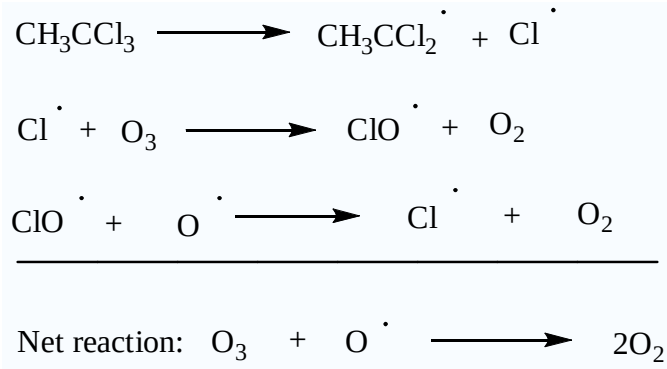

Scheme 1.2: Reaction of ozone with chlorine [CIESIN, 1997]

1.2. Methodology

The ultraviolet-visible (UV-Vis), mid-infrared (MIR), and Raman spectra of TCE were obtained using standard analytical techniques, and these were compared with the literature available and computational calculations carried out. These were all carried out in order to obtain accurate information on the electronic and vibrational frequencies through which the carbon-chloride bond may be activated or excited and the molecule thereby possibly decomposed. All these also aim to provide a better understanding of the molecular structure of TCE. Laser ionization time of flight mass spectroscopy was used to explore the ionization and dissociation characteristics of TCE in the gas phase using both nanosecond and femtosecond laser sources.

By using different physical ionization processes due to the different laser pulse durations, and by using different excitation wavelengths and other parameters, some conclusions may be made regarding the ionization and dissociation of TCE. Since this study is meant to be a first step towards control of chemical processes, and in particular dissociation, some results are presented showing how certain parameters

may influence and control the dissociation of the molecule into different fragments. This is meant as a characterization but will be useful in future studies in this field.

1.3. Background to PBMR relevance

TCE has a similar structure as MTS which is the precursor used in the deposition process of SiC. The SiC layer is one of the layers that are used to coat the PBMR kernel. There are four layers used to coat the kernel as shown in figure 1.2. The first layer is the porous carbon, followed by the thin pyrolytic carbon which is a dense form of carbon, a silicon carbide layer which is a strong refractory material, and another layer of pyrolytic carbon [ANON, 1999]. The layer that is of interest to us is the silicon carbide which provides a barrier that was designed to contain the fuel and fission products.

The chemical vapor deposition of SiC was studied by several authors. It was reported that during decomposition of MTS under chemical vapor deposition conditions, the products formed are HCl, SiHCl, SiCl, and CH, as well as some silanes [Osterhold *et al*., 1994]. Besmann and his co-workers [1992] reported that the products formed during decomposition of MTS were SiC and HCl. They did not mention the mechanism of pyrolysis of MTS. Thus the focus of Pelle's [2008] project was to study the potential mechanisms for the formation of SiC, including the dissociation of MTS.

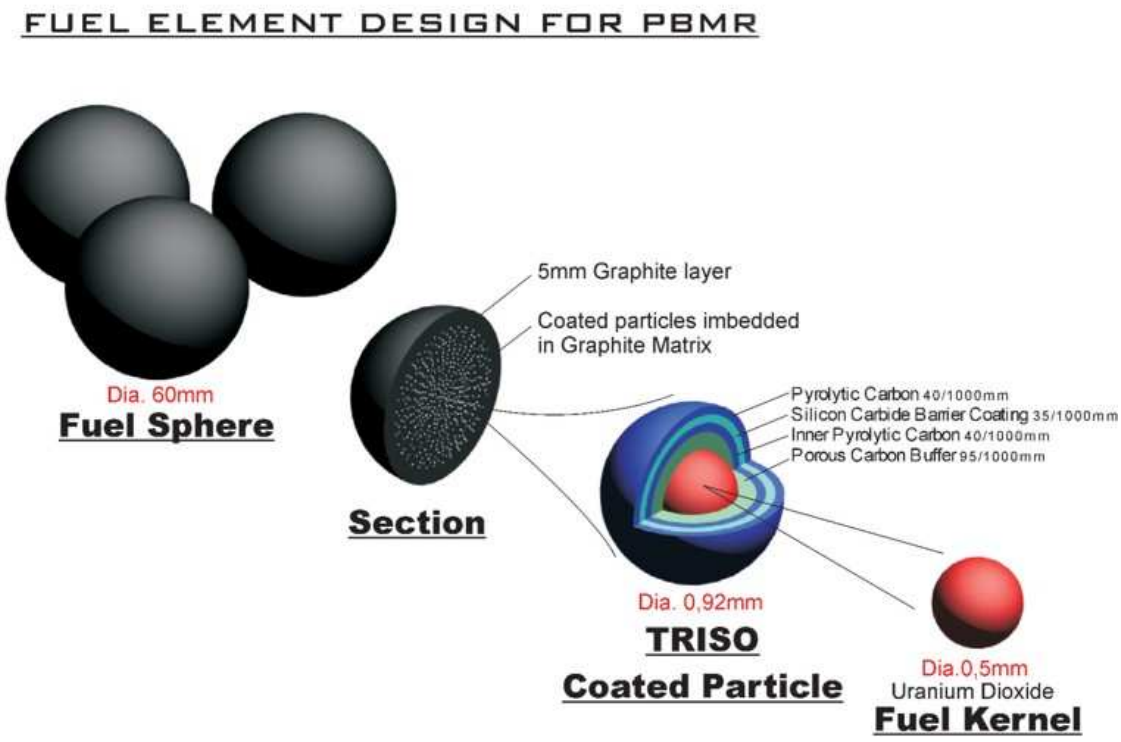

Figure 1.2: PBMR fuel kernel [ANON, 1999].

TCE and MTS molecules have similar structures with different bond lengths, except for the C-H bond. The bond lengths of the two molecules were determined by using ab initio calculation and they were compared with the published results as shown in table 1.1. Understanding how TCE behaves under laser excitation and identifying the products that form during ionization and dissociation will aid to understand how MTS will behave when it is irradiated and which products will form during the ionization and dissociation processes.

Table 1.1: Comparison of the structural parameters for TCE and MTS as observed in literature and as calculated with Spartan 2006 [Spartan, 2006] using the basis set as stated in the following table.

TCE			MTS		
Bonds (Å)	RHF/3-21G*	Venkateswarlu [1951]	Bonds (Å)	RHF/3-21G*	Qtaitat and Mohamad [1994]
C-C	1.53	1.53	Si-C	1.85	1.85
C-Cl	1.79	1.76	Si-Cl	2.03	2.04
C-H	1.08	1.09	C-H	1.08	1.08

1.4. Background to environmental relevance

Most halocarbon compounds in the atmosphere play a major role in the depletion of the ozone layer [Simon *et al*., 1988]. One of these is TCE, which is also known as methylchloroform. TCE has a longer residential time in the atmosphere, thus it can reach the stratosphere easily. In the stratosphere it is degraded by photodissociation processes to form free radical chlorine atoms [McParland, 1995]. The chlorine radicals formed are capable of depleting the stratospheric ozone [Dobson, 1990]. The loss of ozone in the stratosphere is usually due to the chlorine atom which is activated during the photodissociation process. Thus the absorption of the molecule has to be known with high accuracy.

Nayak and co-workers [1995] stated that it is important to know the UV absorption information of the halocarbon compounds which contributes towards ozone depletion in order to determine the altitude at which photodissociation occurs, and

subsequently the release of the chlorine atoms. The absorption information also helps in determining the lifetime of the compounds in the atmosphere. Most halocarbons containing hydrogen atoms such as $CHCl_3$, CH_2Cl_2, CH_3Cl, and $CHFCl_2$ may react with radicals such as •OH and may be destroyed in the troposphere [Simon *et al*., 1988]. The •OH radicals are produced by the action of solar UV light on H_2O and O_3 molecules [Dobson, 1990].

1.5. Dissertation Structure

This dissertation is structured as follows:

- Chapter 1 gives the aims, background to PBMR relevance, background to environment relevance and structure of the dissertation.
- Chapter 2 covers the molecular modeling of TCE.
- Chapter 3 describes and explains the background of techniques used to study TCE.
- Chapter 4 handles the literature background of TCE.
- Chapter 5 gives experimental procedures, results and discussions of the molecular spectroscopy performed.
- Chapter 6 describes the experimental procedures, results and discussions of the laser ionization time of flight mass spectrometry.
- Chapter 7 deals with conclusions and further work.

Chapter 2

Background of molecular modeling

2.1. Introduction

Molecular modeling is a collective term that refers to theoretical methods and computational techniques to model the behaviour, energies and spatial orientation of molecules [Spartan, 2004]. These techniques are used in the fields of computational chemistry, biology, and materials science for studying molecular systems ranging from small “simple” molecules to large biological molecules and material assemblies [Schlecht, 1998]. It also involves the use of computational methods for simulating and predicting the three-dimensional structures of molecules. Molecular modeling includes the use of graphical, mathematical or physical representations to help understand and interpret experimental results or predict the properties of molecules [Schlecht, 1998]. It focuses on obtaining results relevant to chemical problems, not on developing new theoretical methods. Molecular modeling in chemistry is a multi-step process similar to experimental chemistry [Sittert and Lachmann, 2007]. The first step is to define the problem. This is followed by building models to do calculations, and lastly analysing the results [Sittert and Lachmann, 2007]. This process can be repeated with improved parameters. The best suited theoretical model must be chosen for all the calculations. There are different types of models developed to calculate molecular structures and properties of atoms and molecules [Hinchliffe, 2003]. These are broken into two groups: quantum-chemical models, which are derived from the Schrödinger equation, and molecular-mechanics models.

The most well-known quantum-chemical methods used are Hartree-Fock molecular orbital models and semi-empirical molecular orbital models [Spartan, 2004]. The Hartree-Fock approach starts from the Schrödinger equation and then makes three approximations, namely the Born-Oppenheimer, Hartree-Fock and Linear combination of atomic orbitals approximations [Spartan, 2004]. Quantum chemical models are used to determine the energy, infrared spectra and properties such as dipole moment of molecules. These properties may be compared with the experimental data. The quantum-chemical models may also be applied to transition states.

Molecular mechanics models start from force field values, which are sets of parameters and functions describing the potential energy of a system of particles [Sittert and Lachmann, 2007]. To obtain the molecular structure, just as with a Lewis structure, molecules are made up from atoms, not nuclei and electrons as in the quantum chemical models [Spartan, 2004]. Quantum mechanical calculations use electron distributions, which mean that all properties such as electron densities, orbital shapes, atomic charges and polarities are calculated. This calculation cannot however be used to predict molecular shape and structures. Molecular mechanics is much simpler than solving the Schrödinger equation, but it requires large amounts of information about the structure of the molecule [Spartan, 2004]. Molecular mechanics finds an important role in molecular modeling as a tool to establish equilibrium geometries and conformations of large molecules. Molecular mechanics was developed out of a need to describe molecular structures and properties in a practical manner.

2.1.1. Theoretical models

All theoretical methods have limitations; therefore there is no specific method of calculation that is likely to be ideal for all applications. Different molecular mechanics and quantum chemical models will be discussed to determine which method of calculation is most suitable for the present study. The molecular mechanics models are restricted to determine geometries and conformational energy differences of compounds. Quantum chemical models provide energy data, infrared frequencies and properties such as dipole moments, which may be compared with experimental data, making it the most suitable for this study. The Hartree-Fock model is one of the models used to determine the equilibrium geometry and transition state of organic and main group inorganic molecules (except molecules with transition metals). Semi-empirical calculations give less detailed information because only the valence shell is used and ab initio calculation gives information about inner electron distribution; but these distributions have limited chemical relevance [Sittert and Lachmann, 2007].

2.1.1.1. Ab initio methods

The term “ab initio” is a Latin term for “from the beginning”. The name was given to computations which are derived directly from theoretical principles with no inclusions of experimental data [Young, 2001]. Methods that attempt to find solutions for the Schrödinger equation by Hartree-Fock methods and refinements of these methods are often called “ab initio”. In ab initio methods the energy distribution of every electron is calculated [Young, 2001]. Ab initio methods cannot be used for large molecules because of restrictions in the calculation speed of current computers.

The most common type of ab initio calculation is called the Hartree-Fock (HF) calculation. In the Hartree-Fock (HF) calculation there is a primary and secondary approximation. The primary approximation is called the central field approximation. This means that the Coulombic electron-electron repulsion is not really taken into consideration. However, its net effect is included in the calculation. The energies from HF calculations are always greater than the exact energy because of the central field approximation and tend to a limiting value called the Hartree-Fock limit. These energies are usually reported in Hartrees units [Young, 2001]. The second approximation in HF calculations is that the wavefunction must be described by some functional form. Functional form is only known exactly for a few one electron systems [Young, 2001].

Another type of an ab initio method is the Density Functional Theory (DFT), in which the total energy is expressed in terms of the total electron density rather than the wavefunction. Density functional theory (DFT) is a computational method that derives properties of the molecule based on a determination of the electron densities of the molecule [http://chemistry.ncssm.edu, 10 June 2007], where electron density is a physical characteristic of all molecules. DFT has three types of methods namely, local density approximation (LDA) method, gradient corrected (GC) method, and a hydrid method [Sittert and Lachmann, 2007]. The local density approximation (LDA) method is based on the properties of the electron density. This method assumes that the electron density of the molecule is uniform. The gradient corrected (GC) method accounts for the non-uniformity of the electron density. The GC method is also called a non-local method. Hydrid methods such as B3LYP attempt to incorporate some feature from ab initio methods (Hartree-Fock methods) with some of the improvements of DFT mathematics [http://chemistry.ncssm.edu, 10 June 2007]. These hydrid methods are combinations of the Hartree-Fock and DFT

approximations combined with a mathematical function to include electron correlation.

An advantage of the DFT method is that it scales three dimensionally (or N^3 where N is number of basis functions), whereas the Hartree-Fock method scales as N^4 [Spartan, 2006]. As a result DFT calculations are faster with better accuracy. DFT can also perform calculations on some molecules or systems (like transition metals) that are not possible with other ab initio methods. DFT methods overcome one of the disadvantages of ab initio methods (Hartree-Fock) that is the complete neglect of electron correlation [Spartan, 2006]. The DFT methods, such as B3LYP/ 6-31G*, is the most commonly used method for computational chemistry practitioners. It is considered as a standard model for many applications, especially for relatively small molecules. The DFT method was chosen for this study because it is fast and gives more accurate results.

Møller-Plesset perturbation theory is one of the ab initio methods used in the computational chemistry field [MP, 2007]. This method improves on the Hartree-Fock method by adding electron correlation effects by means of the Rayleigh-Schrödinger perturbation theory, usually to second (MP2), third (MP3) or fourth (MP4) order. MP2 order Møller-Plesset calculations are used for this study. These orders are the standard levels used in calculating small systems.

2.1.1.2. Semi-empirical methods

A semi-empirical calculation has the same general structure as HF calculation but needs some initial data. To correct for the errors introduced by omitting parts of the calculation, the method is parameterized by curve fitting to give the best possible

agreement with experimental data [Sittert and Lachmann, 2007]. Advantages of semi-empirical calculations include that they are faster, save computing costs and can be applied to larger molecules than ab initio methods [Spartan, 2004]. One of its disadvantages is that the results are less reliable. Semi-empirical calculations are not suitable for proper energy calculations. They give less information because it uses the valence shell electrons only [Sittert and Lachmann, 2007].

Molecular mechanics methods (one of the semi-empirical methods) are not suited to perform energy calculations. However, they can be used to get preliminary results in a short time and may be used as input for higher level calculations at a later stage [Spartan, 2006]. This method is used for calculating the geometry of larger molecules. The energy expression for the molecular mechanics method consists of simple classical equations (e.g. the harmonic oscillator equation) to describe the energy associated with bond stretching, bending, rotation and intermolecular forces (Van der Waals interactions and hydrogen bonding) [Spartan, 2006]. All of the constants in these equations are obtained from experimental data or an ab initio calculation. The disadvantage of this method is that there are many chemical properties that are not defined within the method, such as electronic excited states [Young, 2001].

2.1.2. Electron density

Electron density surfaces give the size and shape of the molecule or atom. Molecules and atoms are made up of positively-charged nuclei surrounded by negatively-charged electron clouds [Spartan, 2006]. The electron density surface is used to describe changes in bonding on moving from reactants to products through a transition state in a chemical reaction. For instance, for one of the decomposition

reactions of TCE, the C-Cl bond of the reactant is broken and the hydrogen migrates to form the hydrochloric acid (scheme 2.1 and electron density for this reaction in figure 2.1). The most electronegative atoms attract electrons more. The electron density increases around the more electronegative atom at the expense of the less electronegative atom [Spartan, 2004]. If it is concluded from the electron density distributions that the transition state resembles the reactant more than the product, an exothermic reaction is indicated [Spartan, 2006]. This implies that the energy of the product is lower than that of the reactant. The difference in bond stabilities of reactant and product is simply the difference in their total energies.

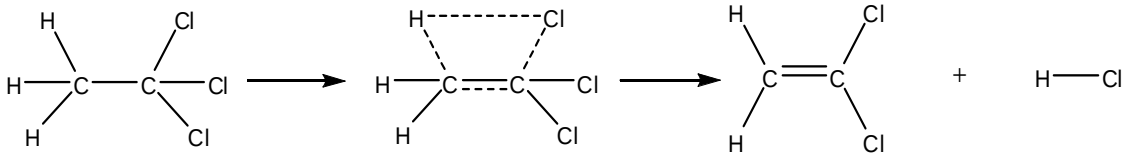

transition state

Scheme 2.1: A dissociation reaction of TCE

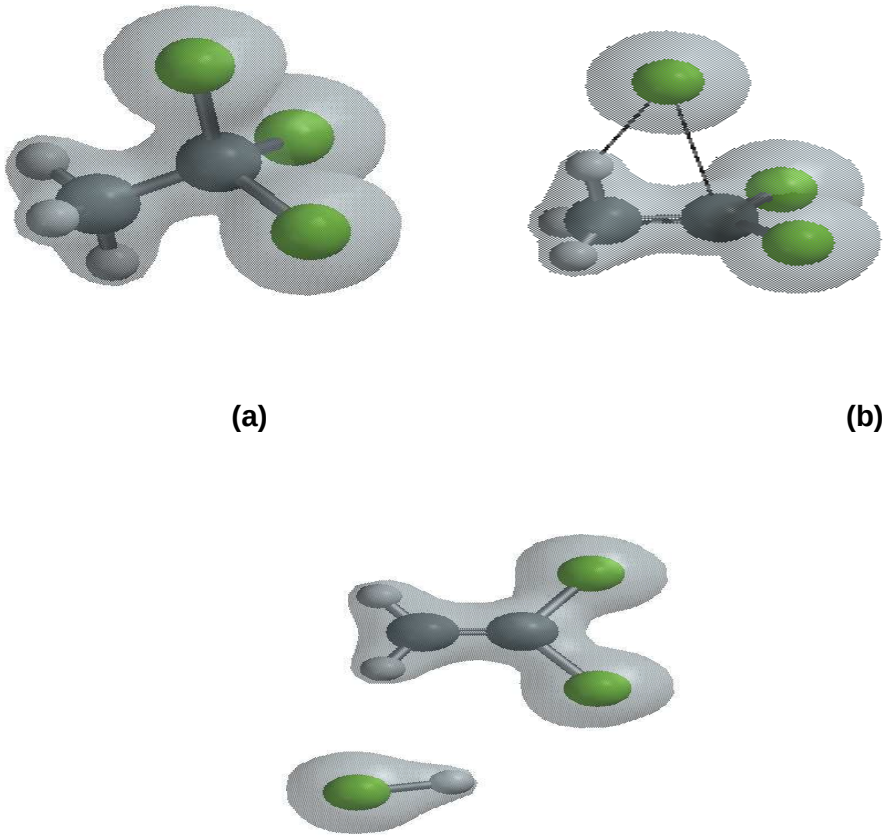

(a) **(b)**

(c)

Figure 2.1: Electron density surfaces for the reactant (a) 1,1,1-trichloroethane, (b) the transition state, and (c) the products, 1,1-dichloroethene and hydrochloric acid (c) [Spartan, 2006]. Green spheres = chlorine, dark grey sphere = carbon, and light grey sphere = hydrogen

2.1.3. Basis sets

Basis sets are the sets of one-electron wavefunctions used to build molecular orbital wavefunctions [Spartan, 2004]. Basis set names come from a specified field of quantum chemistry. There are different types of basis sets, namely, minimal basis sets (STO-3G), split valence basis sets (3-21G, 6-31G and 6-311G), polarization basis sets (6-31G*, 6-31G** and 6-311G*) and diffuse functions (6-31+G* and 6-31+G**) [Sittert and Lachmann, 2007].

The STO-3G basis set is a Gauss-type basis set that has been developed by combining three Gauss functions (3G) to substitute a Slater-type orbital (STO). It is the fastest but least accurate basis set in all cases. It is believed that a split valence basis set uses only one basis function for each core atomic orbital. 3-21G* is the simplest basis set that gives reasonable results. 6-31G* is an improvement of 3-21G* which adds polarization to all the atoms and improves the modelling of core electrons. 6-31G** adds polarization functions to hydrogens and it can improve the total energy of the system. 6-311G* adds more flexibility to the basis sets. 6-31+G* adds extra diffuse functions to heavy atoms and it can improve results for systems with large anions [Spartan, 2004]. The numbers “3” and “6” to the left of the “-“ in these basis sets’ names indicates that 3 and 6 functions are used to describe each inner shell atomic function. The number “21” and “32” to the right of the “-“ indicate that two groups of 2 and 1 and 3 and 1 functions are used to describe each valence shell atomic function. “G” is used to specify that the functions are Gaussian type functions, and “*” indicates that the additional valence functions (polarization functions) are supplied.

When selecting proper basis sets, knowledge of the content of the basis sets and the purpose of refinement is needed. The basis set 6-31G* is one of the most versatile basis sets with reasonable computing speed and results. In this study, selected basis sets are used based on results obtained.

2.2. Computational methods

All calculations were carried out using the Spartan ’06 package with the Molecular Mechanics (MM, restricted Hartree-Fock (RHF), second order Møller-Plesset perturbation (MP2) and Density Functional Theory (DFT) basis sets [Spartan, 2006; MP, 2007]. Geometries were fully optimized using Molecular Mechanics theory with

the Merck Molecular Force Field (MMFF94) basis set. The calculated structural parameters were determined by using Restricted Hartree-Fock (RHF/3-21G* and RHF/6-31G* basis sets) and Møller-Plesset (MP2/6-31G*) calculations; and are listed in table 2.1 and compared with those previously reported by Venkateswarlu [1951] and Ghosh *et al*. [1952]. The structural parameters reported by Venkateswarlu and Ghosh *et al*. were calculated from the rotational constants. Margulés *et al*. [2008] reported some of the parameters using the second order Møller-Plesset perturbation (MP2) method. Increasing level of basis sets for the MP2 method changes the parameter values. Therefore, for this study the 6-31G* basis set was used because it gave results that compare better with experimental values. Molecular properties for TCE were determined by using semi-empirical/PM3, Hartree-Fock/STO-3G and DFT-B3LYP/6-31G* methods.

Table 2.1: Comparison of structural parameters for TCE as calculated with Spartan 2006 using basis sets as stated in the table

	Literature		This study		
Parameters	Venkateswarlu [1951]	Ghosh *et al*. [1952]	RHF/3-21G*	RHF/6-31G*	MP2/6-31G*
Bond lengths					
C-C (Å)	1.53	1.55	1.53	1.52	1.52
C-Cl (Å)	1.76	1.77	1.79	1.78	1.78
C-H (Å)	1.09	1.09	1.08	1.08	1.09
Bond angles					
Cl-C-Cl (°)	109.5	110.2	109.1	109.1	109.1
H-C-H (°)	109.5	109.3	109.6	109.5	109.5

2.3. Results and discussion

2.3.1. Molecular properties

2.3.1.1. Structure of 1,1,1-trichloroethane

The calculated structural parameters with the RHF/3-21G*, RHF/6-31G* and MP2/6-31G* levels agree within 0.1° for H-C-H bond angles (table 2.1). For the C-C bond distance, a value of 1.53 Å was obtained with a smaller basis set (RHF/3-21G*). This value is comparable with the C-C bond of ethane, 1.53 Å [http://en.wikipedia.org, 05 May 2007]. The C-Cl bond length values of 1.79 Å and 1.78 Å are obtained with RHF/3-21G*, RHF/ 6-31G* and MP2/6-31G* levels. The calculated H-C-H bond angles (table 2.1) with RHF/3-21G*, RHF/6-31G* and MP2/6-31G* levels, are reasonably in agreement with the previously reported structure by Ghosh *et al*. [1952]. The H-C-H bond angles reported by Venkateswarlu agrees very well with that calculated using the RHF/6-31G* and MP2/6-31G* levels. These values are different from the H-C-H angle for ethane (107.7°) because, in the TCE molecule, one of the carbon atoms has chlorine atoms attached whereas, in the ethane molecule, all carbons are attached to hydrogen atoms. The C-Cl-C bond angle obtained by both Ghosh *et al*. and Venkateswarlu are in reasonable agreement with the calculated bond angles with all basis sets recorded in table 2.1. The C-H bond distances reported by both Ghosh *et al*. and Venkateswarlu are shorter by 0.01Å when compared to the one obtained by all other basis sets.

2.3.1.2. Infrared spectrum calculations

The reliable prediction of vibrational spectra is of considerable use in assigning the normal modes in a molecule. Computational methods can also be used to assign the bands of the spectra. Molecules vibrate (stretch, bend, twist, etc.) in response to their

absorbing infrared light even if they are cooled to absolute zero. This is the basis of infrared spectroscopy, where absorption of energy by molecules occurs when the frequency of molecular motions matches the frequency of the light. The use of a reliable quantum chemical method helps with the assignments. This can accurately determine the contribution of the different modes in an observed band. The vibrational spectrum of TCE has been studied and determined by different authors as will be discussed below for the gaseous, vapour and liquid phases.

The fundamental frequencies, of which all are active in the infrared region except the torsional vibration around the C-C axis, are computed with the B3LYP method for TCE and recorded in table 2.2. It is very difficult to obtain an accurate experimental value for torsional frequency in the gas phase because it has a very weak intensity. The torsional frequency is often determined in the solid state or from microwave relative intensity measurements. The DFT level of calculation provides accurate vibrational frequencies at low time cost and good results and are obtained with the B3LYP method and the small basis set, 6-31G* [Spartan, 2006].

Calculated and experimental FTIR spectra are given in figure 2.2 and 2.3. The calculated infrared spectrum frequencies with the B3LYP method and 6-31G* basis set level are in reasonable agreement with the presented experimental spectrum frequencies. When calculating the infrared spectrum of TCE, it was confirmed that there are three types of vibrations; namely A_1, A_2 and E. The torsional vibration was found at 321 cm^{-1}, which is in reasonable agreement with torsional vibration reported by Rush [1967] at 300 cm^{-1}. The discrepancies between the calculated and observed spectra is caused by the splitting of the rotational energy levels or broadening of infrared absorbance peaks and this refinement was not included in the calculations using Spartan [Spartan, 2004]. The experimental data was obtained at room temperature.

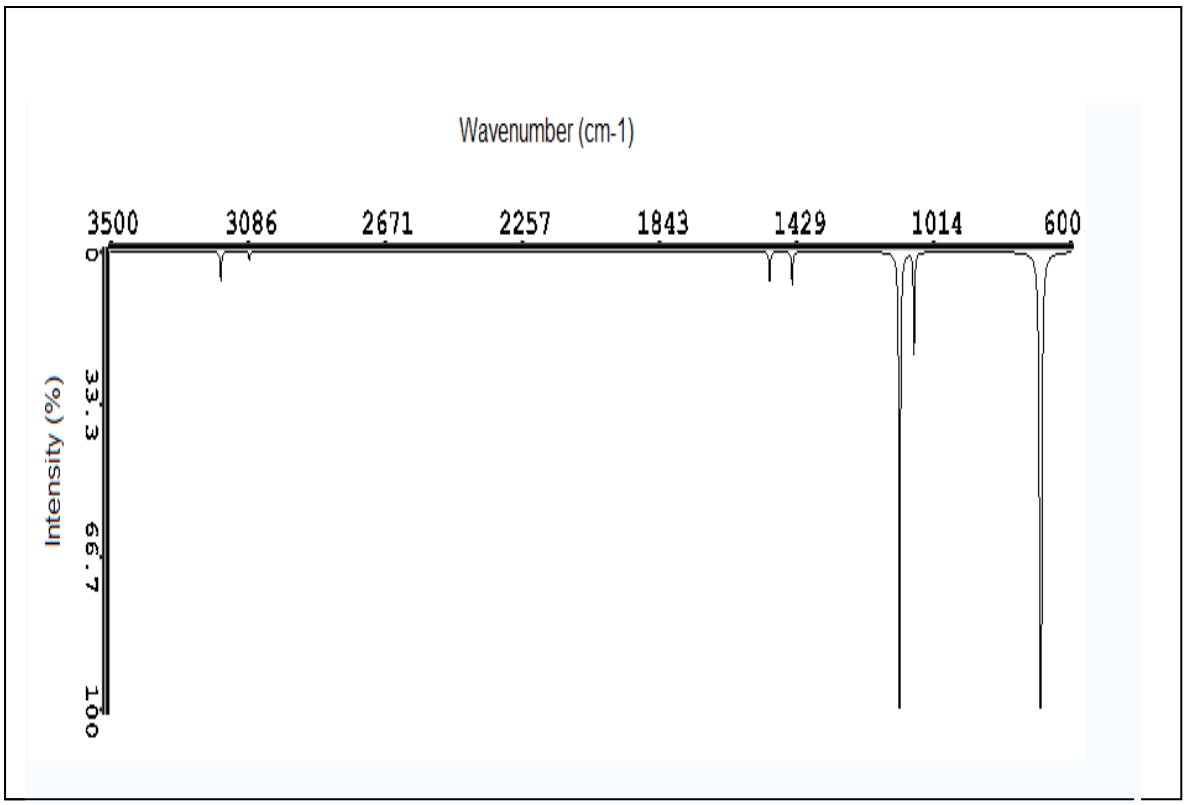

Figure 2.2: Calculated FTIR spectrum for TCE with B3LYP/6-31G* method

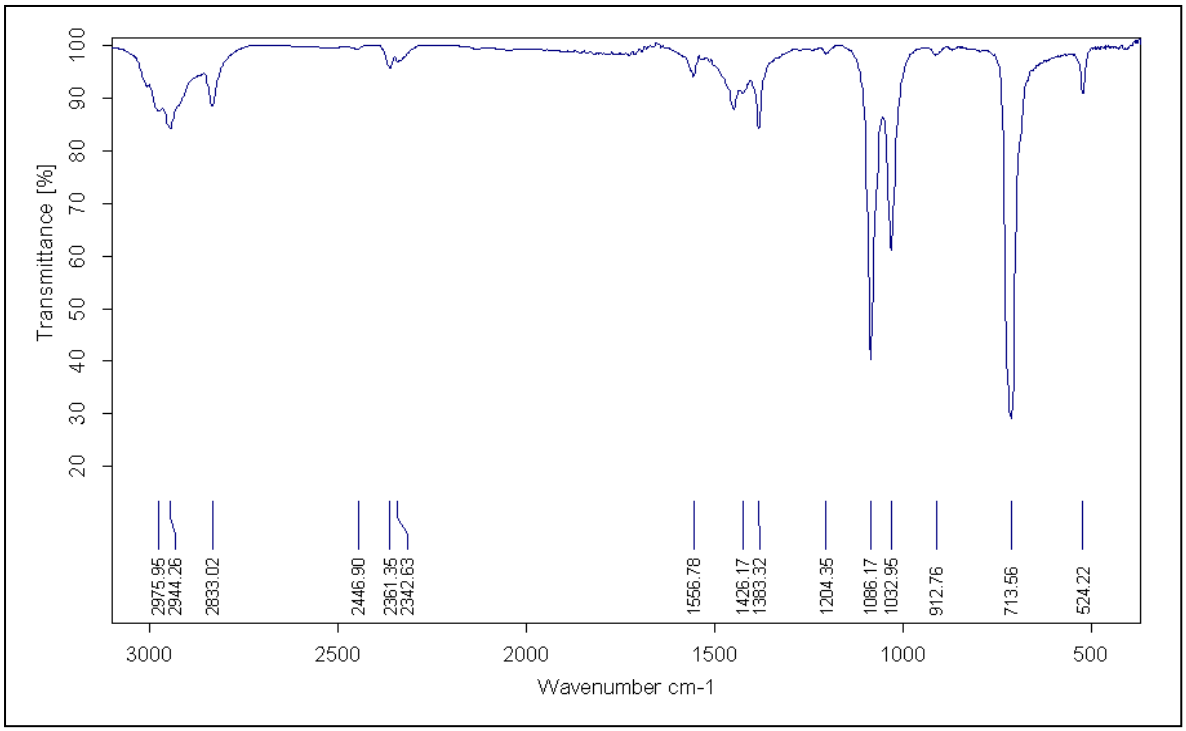

Figure 2.3: FTIR spectrum for liquid TCE measured on Bruker's VERTEX 70 FTIR spectrometer coupled to RAM II FT-Raman module

Table 2.2: Comparison of literature, observed and calculated infrared frequencies of TCE

Frankiss & Harrison [1975]	Observed	Calculated	Assignment	Description
		A_1 symmetric		
2939	2833	3082	v_1	C-H stretching
1378	1383	1442	v_2	CH_3 deformation
1070	1010	1073	v_3	C-C stretching
523	524	517	v_4	C-Cl stretching
344	-----	345	v_5	CCl_3 deformation
		E Asymmetric		
3002	2944	3168	v_7	C-H stretching
1445	1426	1510	v_8	CH_3 deformation
1083	1086	1117	v_9	CH_3 rocking
712	714	691	v_{10}	C-Cl stretching
344	-----	344	v_{11}	CCl_3 deformation
241	-----	239	v_{12}	CCl_3 rocking

2.3.1.3. Dipole moment

A fundamental requirement for infrared activity leading to absorption of infrared radiation is that there must be a net dipole moment during the vibration for the molecule under study. Therefore it is very important for us to calculate the net dipole moment of TCE. TCE has a tetrahedral structure around both carbon atoms and there is a single polar bond in the compound. This information confirms that TCE is a polar molecule. Any polar molecule by definition must have a dipole moment. A

larger dipole moment indicates large separation of charges. In figure 2.4 the left-hand side of the vector (yellow arrow) "+" refers to the positive end of the dipole. The atomic charge for C1 and Cl1 has negative values (C1 is -0.680 eV and Cl1 is -0.055 eV, calculated using B3LYP/6-31G* level) indicating that the atoms have an excess of electron density.

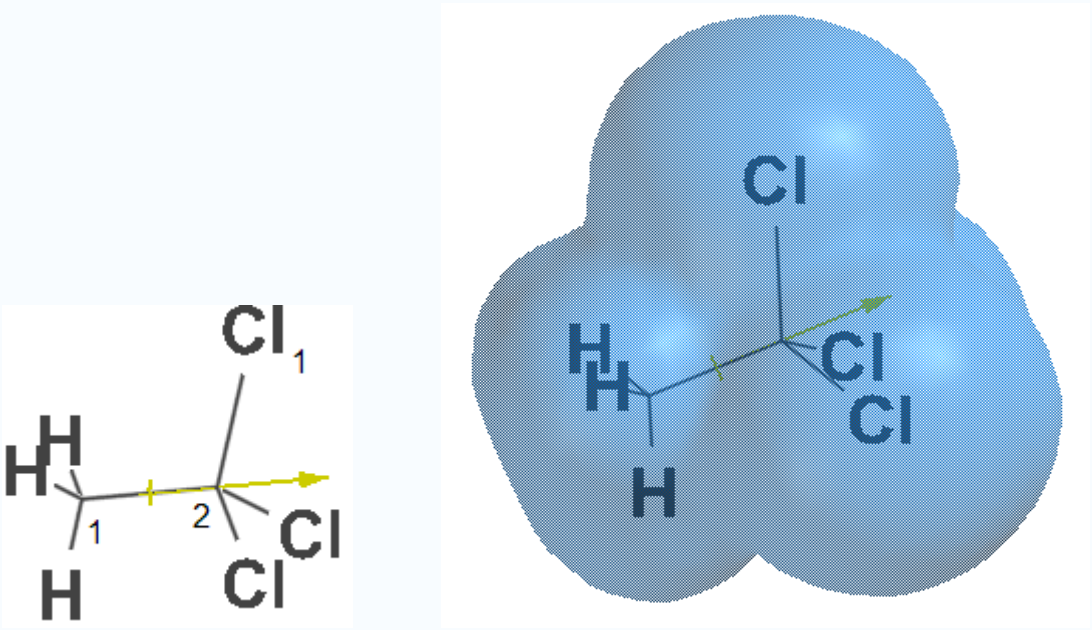

a **b**

Figure 2.4: (a) Direction of dipole moment (yellow arrow) for TCE and (b) dipole vector with electron density

The prediction of an accurate dipole moment is important because dipole moment is an indicator of the relative strength of the intermolecular forces (forces between different molecules). The experimental dipole moment μ for TCE is 1.76 Debye in the liquid phase [Gu *et al*., 2004]. Our calculated value at the B3LYP/6-31G* level is 2 Debye, which is in reasonable agreement with the results reported by Gu *et al*., by considering that the experimental data might have been reported with certain percentage errors. The change of the basis set or DFT method has little effect on this parameter.

Chapter 3

Background of techniques used

Most molecular structural studies are done by the methods of X-ray diffraction, standard spectroscopy and ab initio calculations. In this study, the structure and properties of the liquid and gaseous phase of TCE were studied using the methods of ab initio calculations, standard analytical spectroscopy techniques of FTIR, Raman and UV-Vis spectroscopy, and also by laser ionization time of flight mass spectrometry.

The standard analytical spectroscopy techniques of FTIR, Raman and UV-Vis spectroscopy were employed in this study to obtain information about the structure of TCE and to compare it to available literature and the ab initio calculations. This information can be used to determine the most suitable wavelengths needed to excite the molecule of interest. FTIR and Raman spectra of liquid TCE were obtained to confirm the vibrational assignments that were reported by different authors. The UV-Vis technique was also used for this study because it gave an absorption spectrum that helped in determining the wavelengths needed to most strongly absorb laser radiation and thereby more likely ionise and dissociate the molecule TCE.

In this study, ab initio calculations were done in order to determine the molecular structure of TCE. This includes calculations of molecular properties (structural parameters which are used to determine the bond lengths and angles), FTIR spectrum calculations for comparison with observed FTIR spectrum. Dipole moment of TCE was also calculated to indicate that the molecule has a net dipole moment.

Laser photoionization mass spectroscopy was the focus of this study, and in particular both nanosecond and femtosecond laser ionization were used. Mass spectroscopy in general is a powerful technique that has been used in a variety of fields in the past 30 years [Butler, 1999; Ledingham and Singhal, 1997]. It has been widely used in conjunction with laser sources for dissociation and ionization of gas phase molecules, either resonant or non-resonant [Ledingham and Singhal, 1997] and the subsequent detection of the atomic and molecular ions [Hua *et al*., 2008; Rozgonyi and Gonzalez, 2008]. This technique can be used to detect and accurately quantify trace quantities of atoms or molecules in a gas mixture [Ledingham and Singhal, 1997]. Alternatively, the technique can be used to study the properties of the atoms or molecules after laser excitation and ionization, for example to study bond breaking, dissociation or chemical reactions. This is the motivation for the use of this technique in the present study. Nanosecond and femtosecond laser systems were used in order to explore photoionization of the molecule TCE. A custom time of flight mass spectrometer was used to detect ions formed during the ionization and dissociation processes.

3.1. Molecular spectroscopy

Figure 3.1 shows the electromagnetic spectrum indicating the different regions. The electromagnetic spectrum ranges from short wavelengths (gamma and X-rays) to very long wavelengths (microwaves and radio waves). Figure 3.1 also demonstrates the relationships between wavelength, frequency and energy. The equations below show these relationships:

$v = c/\lambda$……(1)

$\Delta E = hv$..... (2)

where v is the frequency, λ is the wavelength, c is the light velocity, E is energy and h is Plank's constant.

Equation $v = c/\lambda$ demonstrates the relationship between frequency and wavelength which indicates that, when the frequency is increased, the wavelength decreases. Equation $\Delta E = hv$ implies that, for each frequency, there is a specific energy associated with it [http:www.chemguide.co.uk, 21 February 2008]. Therefore the energy associated with radiation of a particular frequency increases as the frequency increases.

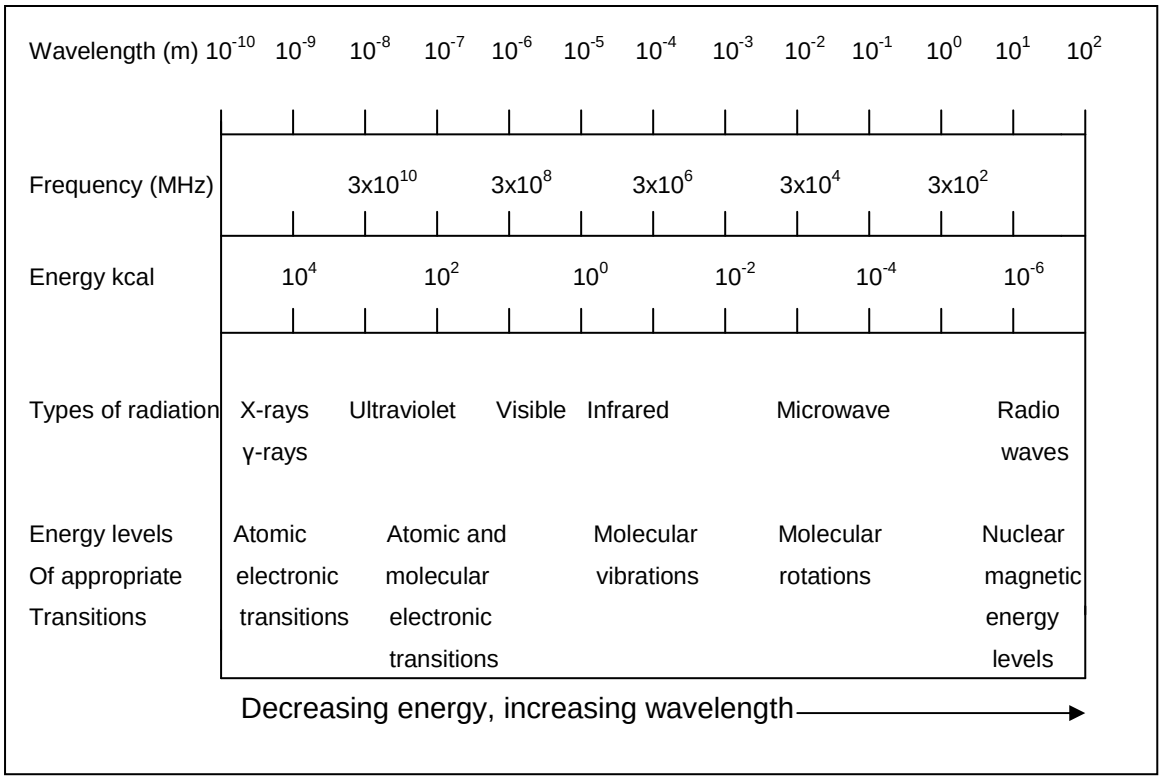

Figure 3.1: The electromagnetic spectrum [www.chemsoc.org, 28 March 2007]

3.1.1. FTIR and Raman spectroscopy

3.1.1.1. FTIR background

Infrared spectroscopy is used to determine the energy associated with the vibrations in molecules. This energy is determined by measuring the absorption of light that corresponds to the vibrational excitation of the molecule from the vibrational ground state to a vibrational excited state. The energy absorbed during irradiation of the sample corresponds to the amount necessary to increase the energy of a specific molecular bending or stretching vibration. For this absorption to occur there must be a change in dipole moment (polarity) of the molecule, indicating that the molecule must undergo a change in dipole moment in order to absorb infrared radiation [Spartan, 2004]. There is no net dipole moment in homonuclear species (such as O_2, N_2 or Cl_2) during vibrational or rotational excitations; therefore these species do not absorb in the infrared region [McMurry, 2000].

Infrared radiation lies between the visible and the microwave region in the electromagnetic spectrum as shown in figure 3.1. It is normally measured in frequency (Hz), wavenumber (cm^{-1}) or wavelength (nm) units. The far infrared region has a lower energy and it may be used for rotational spectroscopy measurements and crystal lattice vibrations [http://en.wikipedia.org, 12 June 2008]. The mid infrared region may be used to study the fundamental vibrations associated with the rotational-vibrational structure. This is mostly used as it is involved with molecular vibrations found in organic molecules. The gas infrared spectrum normally shows the rotational energy states, but rotation is highly restricted for liquid and solid phases. The near infrared region has higher energy and it can produce overtones or harmonic

vibrations [http://en.wikipedia.org, 12 June 2008]. Table 3.1 shows the ranges of infrared spectra.

Table 3.1: Infrared spectral regions [http://en.wikipedia.org, 12 June 2008]

Region	Wavelength (λ) range in μm	Wavenumber (υ) range in cm^{-1}
Near	0.6 to 2.5	15000 to 5000
Mid	2.5 to 50	4000 to 400
Far	50 to 100	400 to 10
Most used	2.5 to 15	4000 to 500

Infrared spectra normally do not display all absorption signals for 3N-6 or 3N-5 fundamentals, where N is number of atoms in a compound. The 3N-6 equation is for non-linear molecules and 3N-5 is for linear molecules. The number of observed absorptions may be less or more due to other vibrations being degenerate or the combination tones, and overtones of the fundamental vibrations. However, the number of observed absorptions may decrease due to molecular symmetry and selection rules [McMurry, 2000]. Molecular symmetry and selection rules will be described in detail in the following section of this chapter. The selection rule for infrared absorption is that the dipole moment of the molecule should change for a vibration to absorb infrared energy. The chart in figure 3.2 shows regions in the infrared spectrum in which various kinds of vibrational bands of different functional groups are observed. The section above the dashed line is for stretching vibrations and the one below the dashed line is for the bending vibrations.

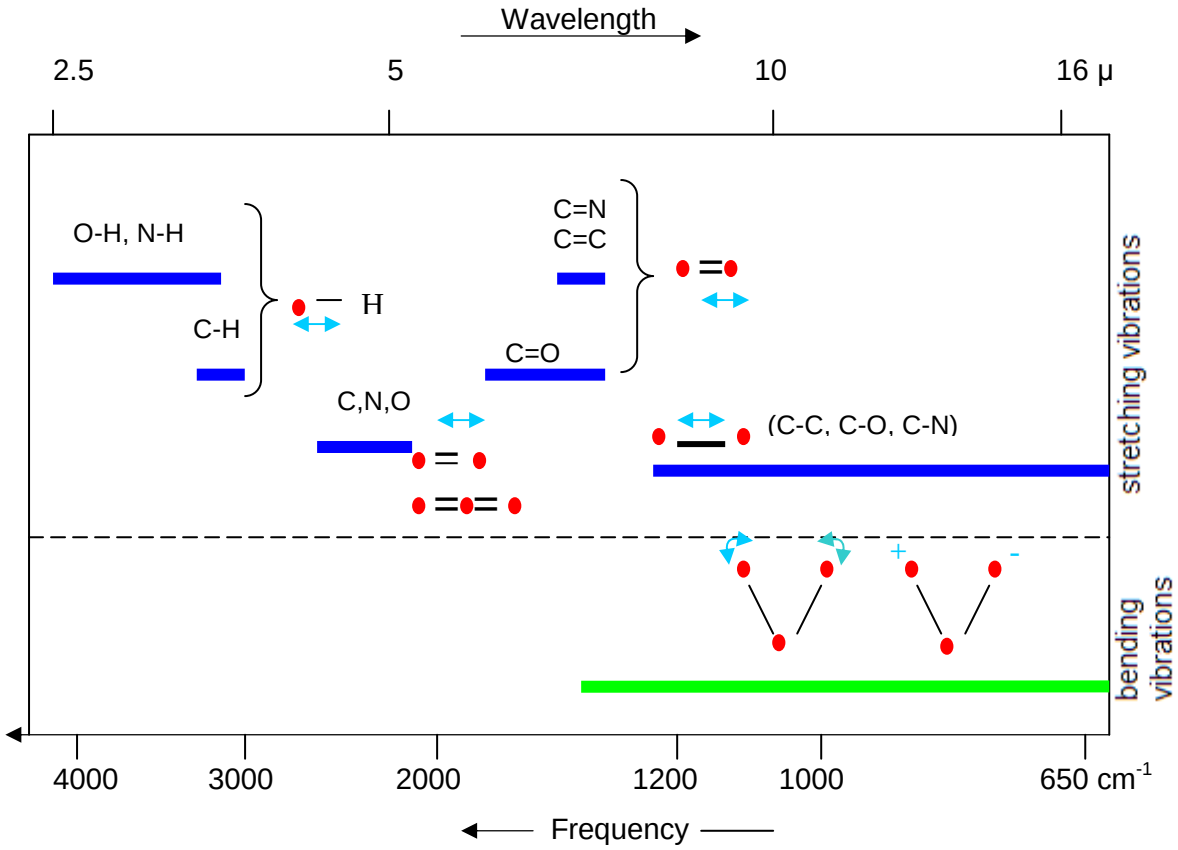

Figure 3.2: Regions in the infrared spectrum with various kinds of vibrational bands of different functional groups [http://www.cem.msu.edu, 10 June 2007]

An infrared spectrum has different types of bands which include fundamental vibrations, overtones, combination bands and skeleton vibrations (fingerprint). The fundamental vibrations are for functional groups. Overtones are normally at approximately twice (or more) the wavenumber of the fundamental vibrations and they are observed in the higher wavenumber region of the infrared spectrum. It corresponds to absorption of radiation corresponding to the change from the ground state to the second vibrational energy level. The overtone peaks are relatively weak as compared to the fundamental vibration peaks. The region of 1450 to 600 cm^{-1} is called the fingerprint region. The vibrational bands in the range of 4000 to 1450 cm^{-1} are in the fundamental frequency region and they are due to the stretching vibrations [McMurry, 2000]. Infrared spectra may be presented as transmittance or absorbance.

3.1.1.2. Raman background

Raman spectroscopy is a spectroscopic technique used to determine the vibrational and rotational modes within molecules. This is a complimentary technique to infrared spectroscopy and it is based on the Raman effect which is an inelastic collision between molecules and photons [http://www.raman.de, 16 April 2007]. Raman spectroscopy is used to identify the specific chemical species, determine molecular structure, to study the changes in chemical bonding, and for the identification of minerals. The intensities and wavelengths of Raman scattering from a laser source are measured in the visible, near infrared, or near ultraviolet region. Raman scattering means that the wavelength of monochromatic light is shifted by vibrations of molecules or crystal lattices [http://www.raman.de, 16 April 2007]. Figure 3.3 shows a schematic representation of the Raman scattering principle. The frequency of scattered radiation is analysed, the incident radiation wavelength is observed and a relatively small amount of inelastically scattered radiation at different wavelength is observed [http://www.andor.com, 28 March 2007].

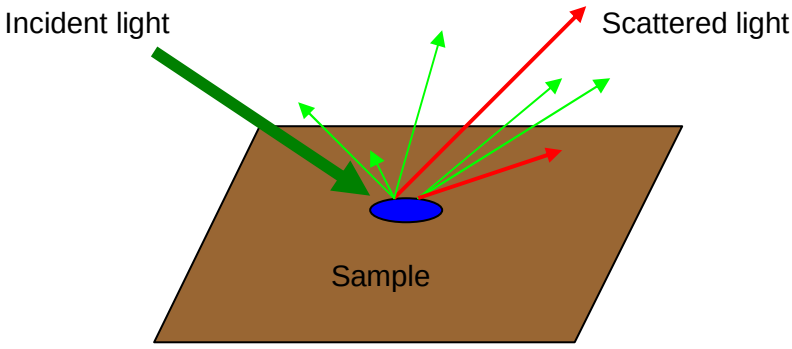

Figure 3.3: Schematic representation of the Raman scattering principle (Red arrows: Raman scattering and bright green arrows: Rayleigh scatter) [http://www.andor.com, 28 March 2007]

Elastic scattering is called Rayleigh scattering. In Rayleigh scattering the photon emitted has the same wavelength as the absorbed photon. Some photons are inelastically scattered with different wavelengths due to the influence of the molecular structure. The process is referred to as Stokes and anti-Stokes Raman scattering. For the Stokes Raman scattering the measured wavelength increases due to a decrease in the energy during collision, thus this is detected at longer wavelengths than the incident light. In anti-Stokes Raman scattering the measured wavelength decreases due to an increase in the energy during collision, thus this can be detected at shorter wavelengths. This anti-Stokes Raman scattering is only possible if the molecule is in an excited vibrational state before collision. Figure 3.4 shows the energy level diagram.

The thickness of the lines in figure 3.4 is proportional to the signal strength from the different transitions. Visible lasers, such as Ar+, K+, Nd:YAG, He-Ne, and diode, are used in Raman spectroscopy to excite the molecule to a higher energy level. The Nd:YAG laser was used in the Raman spectrometer for this study. A Raman spectrum is shown schematically in figure 3.5. Stokes Raman radiation and anti-Stokes radiation has less scattered radiation than incident radiation [http://www.andor.com, 28 March 2008].

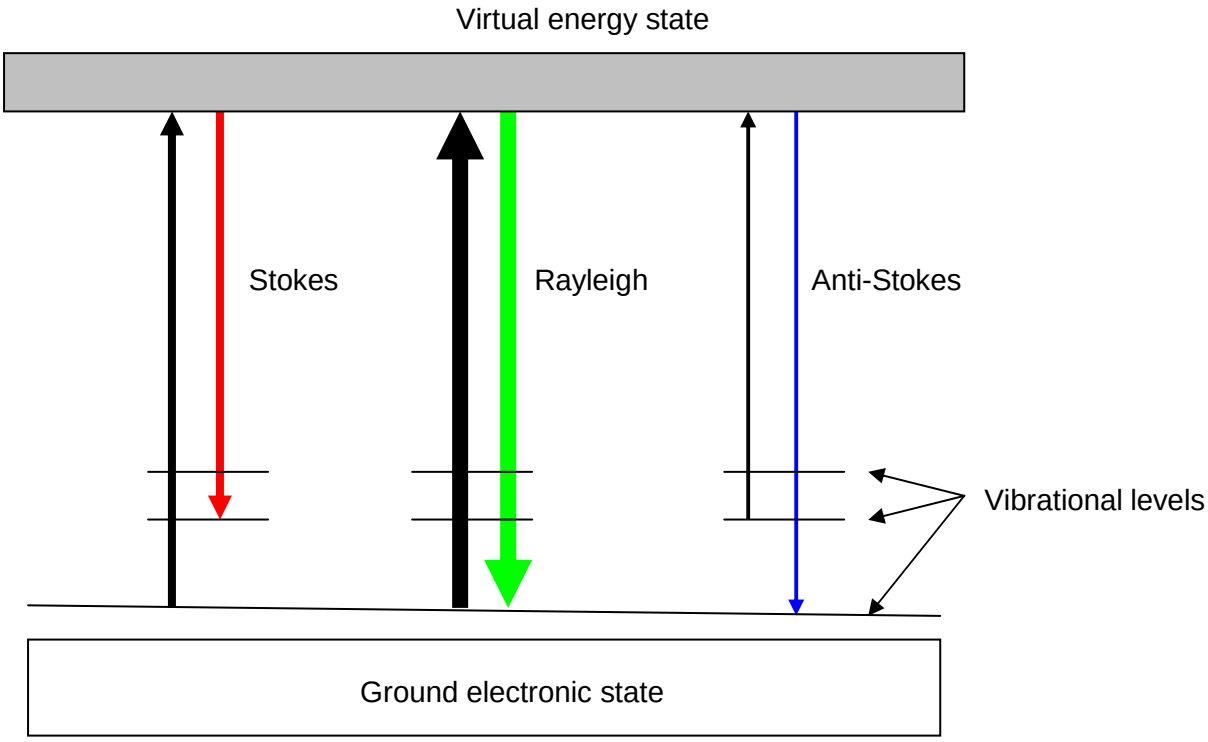

Figure 3.4: Schematic representation of the energy levels of Raman and Rayleigh scattering. Raman scattering takes place to the longer wavelengths (Stokes Raman scattering) and shorter wavelengths (anti-Stokes Raman scattering) [http://www.raman.de, 16 April 2007]

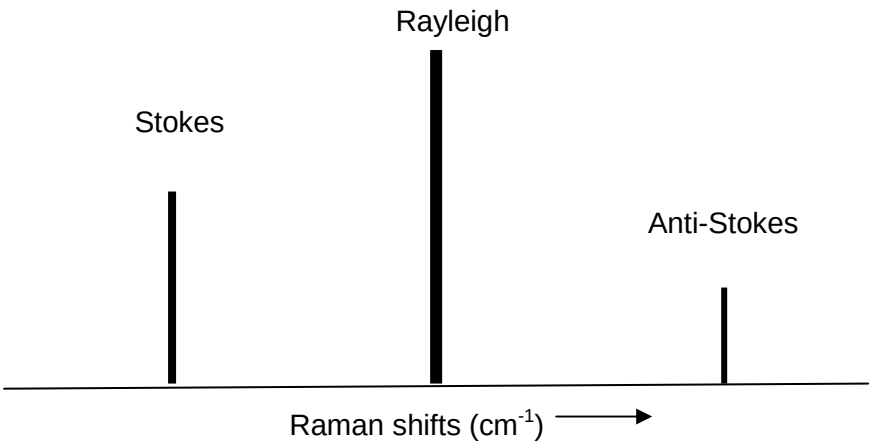

Figure 3.5: Comparison of intensities of lines in a Raman spectrum [http://www.andor.com, 28 March 2007]

3.1.2. Molecular vibrations

The vibrational modes have two categories which are stretching and bending vibrations. The stretching vibration may be symmetric or asymmetric. The bending vibration may be in-plane bending (rocking or scissoring) and out-of-plane bending (wagging or twisting) [McMurry, 2000]. Some vibrations are weak in infrared and strong in Raman spectra. As a general rule vibrations are strong in Raman spectra if the bond has a covalent character and strong in infrared spectra if the bond is ionic. The infrared and Raman spectroscopy are therefore complimentary tools for molecular structure studies. A net change in bond polarizability must be observed for a transition to be Raman active. Therefore, conclusions drawn from both Raman and infrared spectra are more reliable than those given by one spectrum. For example, very weak or missing fundamentals in the infrared spectrum may be present as strong bands in the Raman spectrum.

3.1.2.1. Selection rules for IR and Raman spectroscopy

To determine whether a specific vibration is active in the infrared and/or Raman spectra, the selection rules may be applied to each normal vibration. Molecular vibrations symmetric with respect to the centre of symmetry are not allowed for infrared spectra, whereas molecular vibrations that are asymmetric with regard to the centre of symmetry are not allowed in Raman spectra [McMurry, 2000]. This is called the rule of mutual exclusion. However, according to quantum mechanics principles a vibration is infrared active if the dipole moment is changing during the normal vibration and a vibration is Raman active if the polarizability is changing during the normal vibration. Therefore, infrared spectroscopy gives information about functional

groups and Raman spectroscopy contributes to the characterization of the carbon backbone of molecules. The amount of polarizability change determines the intensity and the vibrational level involved determines the Raman shift.

3.1.3. UV-Vis spectroscopy

UV-Vis spectroscopy is an analytical tool that is used for many reasons, including for assaying and identification of functional groups in molecules. It is used widely in chemical and biochemical laboratories for a variety of tasks, such as tracing metal content in alloys and determination of the concentration of solutions. It uses the light in the visible, near ultraviolet and near infrared wavelength ranges. In this wavelength range molecules typically undergo electronic and vibrational transitions.

3.1.3.1. UV-Vis absorption spectra

A UV-Vis spectrum is a graph of light absorbance versus wavelength in the UV and/or visible regions. An ultraviolet spectrum is recorded by irradiating the sample with UV light of continuously changing wavelength [McMurry, 2000]. When the UV wavelength corresponds to the energy needed to excite an electron to a higher electronic energy level, energy is absorbed. An absorption spectrum will show a number of absorption bands corresponding to different electronic energy levels of atoms in molecules. This spectrum can be recorded as absorbance or transmittance. Absorbance, A, is usually represented by the equation $\boldsymbol{A = log_{10}\, I_0/I}$, where $\boldsymbol{I_0}$ is the intensity of the light passing through the reference cell and $\boldsymbol{I}$ is the intensity of light passing through the sample cell [http:www.chemguide.co.uk, 22 February 2008]. The amount of the light absorbed depends on the number of molecules it interacts with.

Absorption of ultraviolet and visible radiation in molecules is restricted to certain functional groups (chromophores) that contain valence electrons of low excitation energy [http://teaching.shu.ac.uk, 28 March 2008]. Chromophores are groups that absorb light in a molecule [http://www.chemguide.co.uk, 26 February 2008]. There are different types of electronic transitions which can be considered in a spectrum but for this study only the electronic transition involving π, σ and n electrons are discussed. These transitions occur during the processes initiated in the molecule studied. Figure 3.6 shows the transitions involving π, σ and n electrons. The rule says that an electron can be promoted from the highest occupied molecular orbital (HOMO) to the lowest unoccupied molecular orbital (LUMO) and the resulting species is called an excited state.

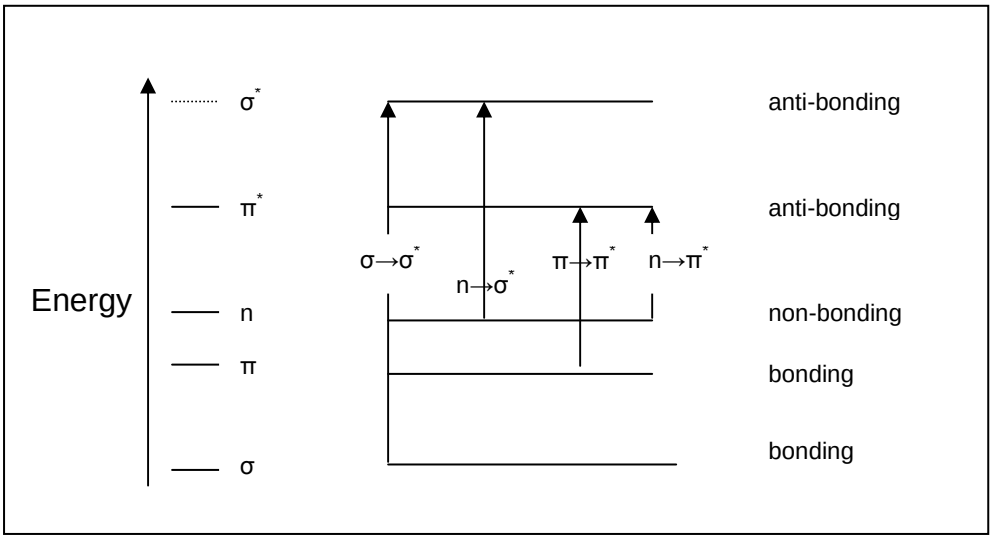

Figure 3.6: Energy level diagram showing transitions involving π, σ and n electrons [http://www.chemguide.co.uk, 25 February 2008]

According to the valence bond theory, figure 3.6 can be explained as follows: Valence electrons are found in three types of electron orbitals, namely: single bond, σ, bonding orbitals; double or triple bond, π, bonding orbitals; and non bonding orbitals (lone pairs). Sigma (σ) bonding orbitals are lower in energy than π bonding orbitals. They are also lower in energy than non-bonding orbitals [http://www.chemguide.co.uk, 25 February 2008]. When a bonding orbital is formed it is lower in energy than the energy of the original orbitals combined. When bonds are formed energy is released and the orbital becomes stable because of the attractions between the nuclei and the electrons.

An anti-bonding orbital is less stable than the original orbitals because there are no equivalent attractions, only the repulsion is obtained. The anti-bonding orbitals are normally empty and lower the stability of the molecule if they contain electrons. A transition occurs from the filled orbitals to the empty orbital, usually an anti-bonding orbital, σ^* or π^*, as in the figure 3.6, when electromagnetic radiation of the correct frequency is absorbed [http://www.chemguide.co.uk, 25 February 2008]. The gap between these levels determines the energy of the light absorbed. These gaps will be different in different molecules. $\sigma \rightarrow \sigma^*$ transitions show that an electron in a bonding σ orbital is excited to the corresponding anti-bonding orbital and the energy required may be large. Compounds with lone pairs (non-bonding electrons) are capable of $n \rightarrow \sigma^*$ transitions; this transition requires less energy than $\sigma \rightarrow \sigma^*$ transitions. Overlaps between s orbitals are called sigma (σ) orbitals and overlaps between p orbitals results in both sigma (σ) orbitals and pi (π) orbitals.

3.2. Laser background

The word LASER is an acronym that stands for Light Amplification by Stimulated Emission of Radiation [Telle *et al*., 2007]. Lasers are oscillators (generators or source of light) and not amplifiers (devices for increasing the strength of a signal). However, the physical process that occurs during laser action is stimulated emission which is amplified by using mirrors. A laser is a device used to excite atoms or molecules to give out energy as light in a specific way. The light given out will be at frequencies in either the infrared, visible, or ultraviolet regions of the electromagnetic spectrum [Siegman, 1986]. The two main components which are necessary for creating a laser are a gain medium and a resonator optical cavity (two mirrors). One mirror is fully reflective and the other mirror is partially reflective so that light can pass through [Australian Laser Manufacturer, 2006]. Energy is pumped into the gain medium by either a flash-lamp or another laser. This process excites electrons in atoms or molecules to excited states which subsequently relaxes back to the ground state through either stimulated emission or spontaneous emission. Since stimulated emission occurs mainly in the direction of incident photons, photons which bounce back and forth between the two mirrors are selectively amplified. Once the quantity of photons has increased sufficiently, a small quantity passes through the partially reflective mirror and the laser output is generated.

Lasers have the unique characteristic that is the light emitted from the laser can be monochromatic (one wavelength), coherent (all waves are in phase with one another), directional (output beam is narrow) and has a high intensity (large number of photons) [Telle *et al*., 2007]. All lasers have the following elements in common as shown in figure 3.7:

1) A laser medium, which is a collection of atoms or molecules that can be a solid, liquid, gas or semiconductor material able to be pumped to a higher energy state;

2) A pump source, which pumps energy into the laser medium. This source supplies energy from excitation from a lower to a higher level to create population inversion. The pump source can be optical, electrical, mechanical or chemical; and

3) A resonator, which consists of two mirrors. One mirror is fully reflective and the other one is partially reflective.

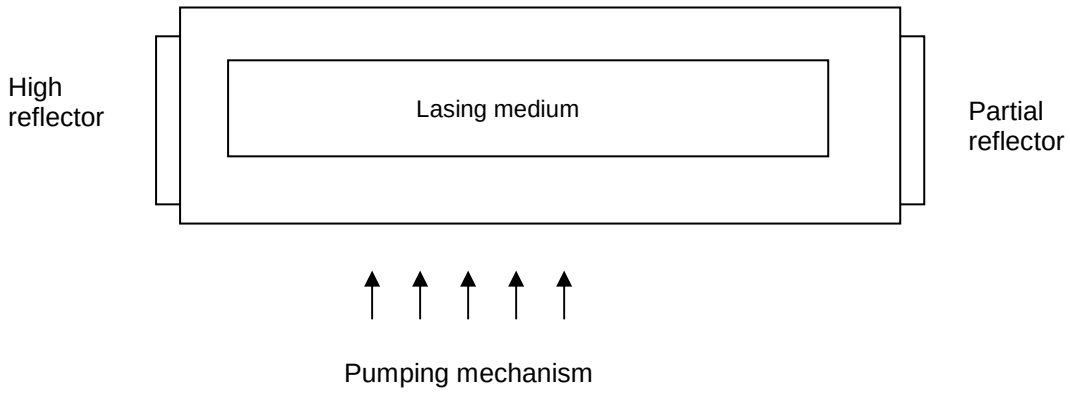

Figure 3.7: Schematic diagram of a basic laser [Telle *et al*., 2007]

A laser can be continuous or pulsed, which means that the laser output can be continuous and constant or there can be breaks in between pulses. Continuous lasers are useful in many applications but the peak power in a pulsed laser can be very large [Australian Laser Manufacturer, 2006] and this has unique advantages for this study. Laser spectroscopy is a research field in which lasers are used in combination with spectroscopic techniques to provide information about the interaction of coherent light with matter and in general has a high resolution and sensitivity. This field has led to advances in the precision with which spectral line frequencies can be measured, and this has significance to our understanding of basic atomic processes. A commercial Nd:YAG laser, an excimer-pumped dye laser

and femtosecond laser were chosen for this study because of their availability and their ability to ionize the molecule of interest.

3.3. Lasers used in this study

3.3.1. Nanosecond lasers

3.3.1.1. Neodymium: Yttrium Aluminium Garnet (Nd:YAG) laser

The Nd:YAG laser as shown in figure 3.8 is a solid state laser that is optically pumped using flash-lamps (xenon for pulsed laser and tungsten arc for CW) or laser diodes [Telle *et al*., 2007]. The Nd:YAG crystal is used as a lasing medium [http://www.phy.davidson.edu, 20 May 2008].

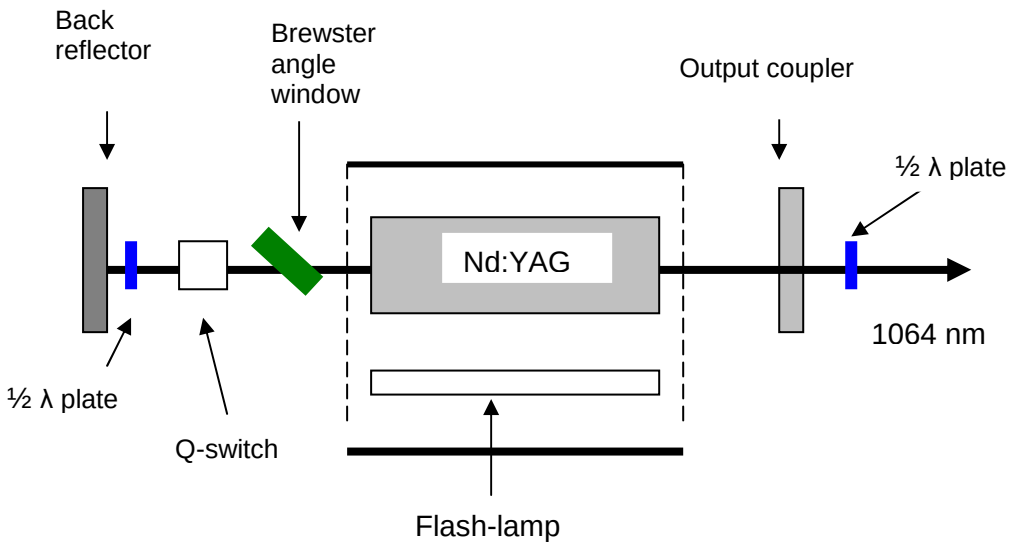

Figure 3.8: Schematic diagram of Nd:YAG laser [Telle *et al*., 2007]

The lasing medium operates as a four level gain medium system as shown in figure 3.9. Population inversion results when incident light on the Nd:YAG crystal is absorbed. The stimulated emission process starts when atoms/molecules at the upper energy level decay to the lower energy level; thus when electrons, as in figure 3.9, decay from E_2 to E_1 and the photons emitted have the same wavelength, direction and phase as a background photon. This stimulated emission in the Nd:YAG crystal is strongest in the infrared region with a wavelength of 1064 nm. There are also emission lines near 940, 1120, 1320 and 1440 nm [http://en.wikipedia.org, 20 May 2008]. The wavelength of 1064 nm can be frequency doubled, tripled and quadrupled (532, 355 and 266 nm) using suitable nonlinear crystals [http://www.rp-photonics.com, 17 June 2008]. The Nd:YAG lasers operate in pulsed or continuous modes. The output power of the continuous modes ranges from 0.1 to 100 W. For the pulsed mode the output energy depends on whether the laser is in Q-switch mode or normal pulse mode [Telle *et al*., 2007]. The typical output energy of pulsed Nd:YAG lasers with pulses durations of 100 to 1000 *μ*s range from 0.1 to 100 J per pulse and those with pulse durations of 10 to 20 ns range from 0.01 to 1 J per pulse [Telle *et al*., 2007].

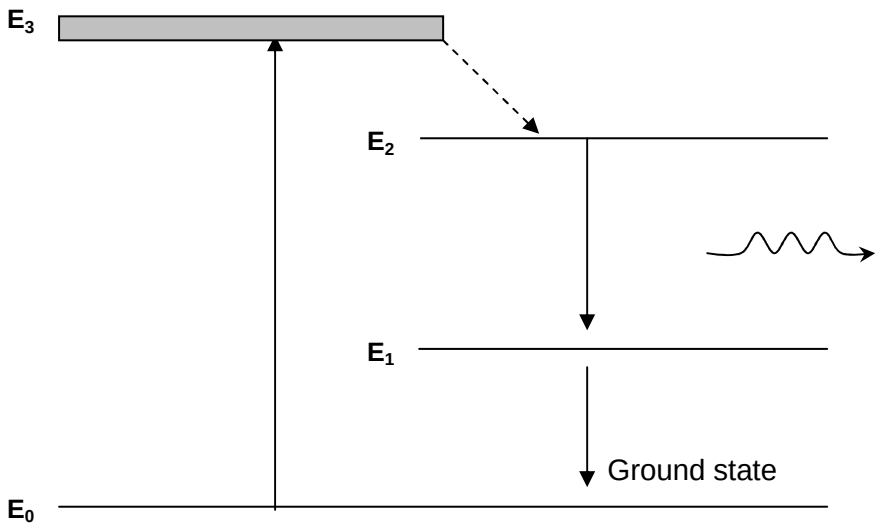

Figure 3.9: Four level system for the Nd:YAG laser [http://www.phy.davidson.edu, 20 May 2008]

3.3.1.2. Excimer laser

The excimer lasers are pulsed gas halide lasers with wavelengths in the ultraviolet region of the electromagnetic spectrum, although some may have wavelengths in the visible region [Livingstone, 2002]. They are typically pulsed with pulses of nanosecond durations [http://www.rp-photonics.com, 17 June 2008]. The excimer laser's gain medium is composed of a mixture of inert gasses, such as argon, xenon, krypton and reactive halogen gasses, such as fluorine, chlorine or bromine [http://www.rp-photonics.com, 17 June 2008]. This gain medium is pumped with a high voltage electric discharge or electron beam. The word excimer comes from the phrase excited dimer and it refers to a molecule which is bound (associative) in the excited state but dissociated (repulsive) in the ground state. Thus excimer molecules can be generated when HCl in helium gas reacts with Xe in the excited state to form XeCl. When the molecule decays to the ground state they dissociate to form Xe^* and Cl^*. The excimer laser transitions occur in ArF at 193 nm, KrF at 248 nm, XeCl at 308 nm and XeF at 353 nm [Livingstone, 2002]. Most excimer lasers are operated with a pulse repetition rate of 1 to 100 Hz and pulse durations of approximately 10 to 50 ns [http://www.rp-photonics.com, 17 June 2008]. Excimer lasers are used in a wide variety of different fields of research. For this work, the excimer laser shown schematically in figure 3.10 was used to pump a dye laser. The laser transition for the excimer laser used occurs in XeCl at 308 nm. This laser is a super radiant laser which means that there is little or no oscillation. The gases used in this laser are 5% hydrochloric acid in helium, argon and xenon, with total pressure of 124 kPa. The laser beam diverges strongly at short distance. To minimise divergence of the beam, a collimating lens is usually used.

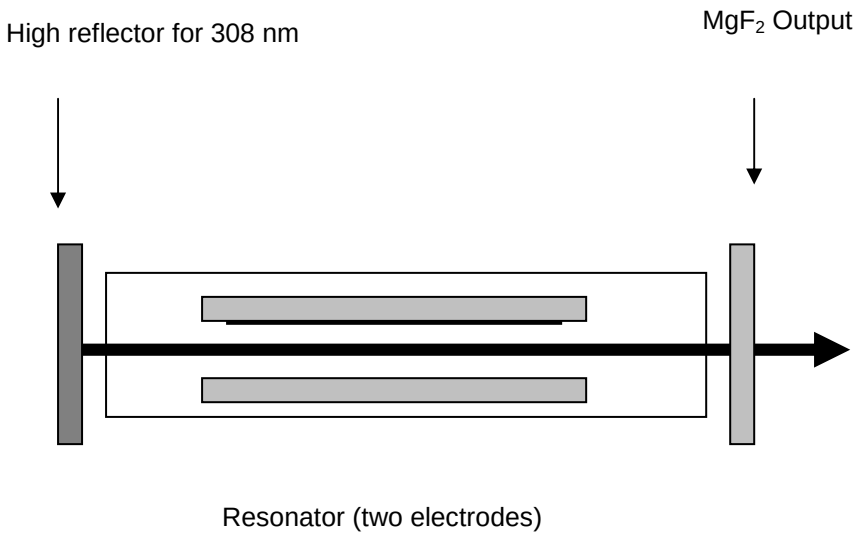

Figure 3.10: Schematic diagram for the excimer laser [Telle *et al*., 2007]

3.3.1.3. Dye laser

The dye laser is shown schematically in figure 3.11. This is a liquid state laser using an organic dye as lasing medium [Telle, *et al*., 2007]. The organic dyes are chosen according to the specific applications and are dissolved in a suitable solvent such as water, alcohol or glycol. Organic dyes have fluorescent bandwidths of 50 to 100 nm, which makes them suitable for generating tuneable laser radiation [http://en.wikipedia.org, 20 May 2008]. There is therefore a wide range of wavelengths possible using a dye lasing medium as compared to gases and solid state lasing mediums, and the dye laser is wavelength tuneable in a broad range [Le, 2002].

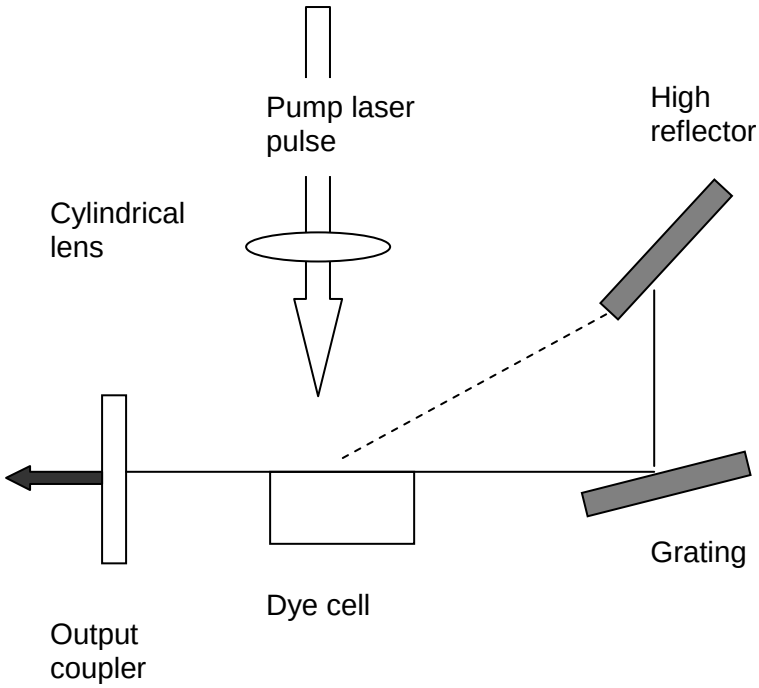

Figure 3.11: Schematic diagram of dye laser [Telle *et al*., 2007]

Liquid lasers have advantages and disadvantages. Its advantages are that it is widely tuneable and can have a very narrow laser bandwidth. The disadvantage is that they chemically degrade over time when pumped by ultraviolet light (they degrade and need replacement regularly) [Carley *et al.*, 2005]. A grating or a prism dispersive optical element is used in the laser cavity to perform selective tuning [http://en.wikipedia.org, 20 May 2008]. This tuning can give narrow line widths. A broad and continuous range of wavelengths can be produced in dye lasers and most of them are in the visible region. Dye lasers can be operated in pulsed, continuous or mode-locked modes. A flash-lamp or another laser (excimer, nitrogen, or frequency multiplied Nd:YAG lasers) can be used to pump the dye laser. The peak power for the dye laser depends on the dye used and the peak power is normally in the range of 10 to 20 kW [Le, 2002].

A dye laser is also a four level (shown in figure 3.12) energetic system [Telle *et al*., 2007]. The dye laser absorbs wavelengths of light which are shorter than those which it emits. Energy absorbed by the dye creates a population inversion; thus electrons

which are initially in the ground state are moved to the excited state until there are more excited state molecules than ground state molecules. Figure 3.12 also represents the energy level diagram for the dye laser.

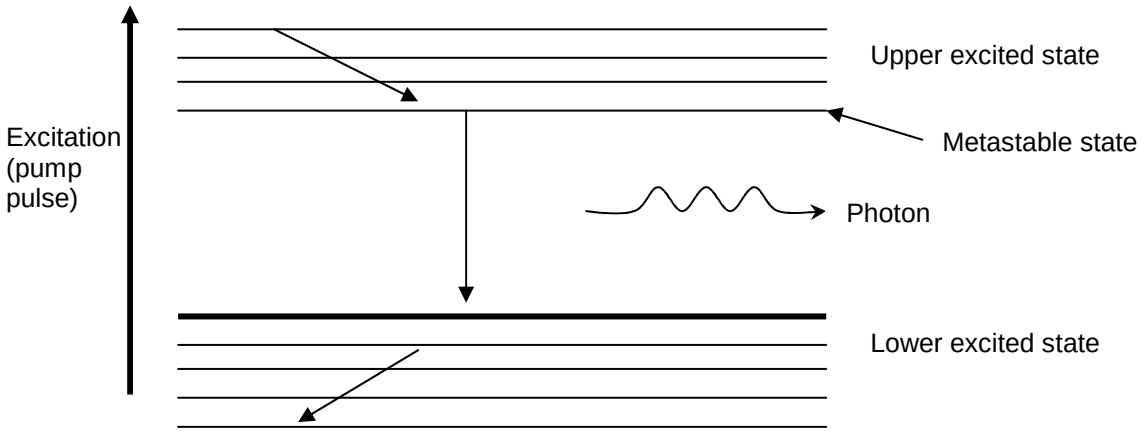

Figure 3.12: Energy level diagram of a dye laser [Le, 2002]

3.3.2. Femtosecond lasers

Femtosecond lasers, also known as ultra-fast lasers, producing short laser pulses, are used in many fields of research. Femtosecond lasers have extremely short pulse durations that allow the study and detection of very short-lived transient chemical reaction intermediates and transition states [Reid and Wynne, 2000]. Femtosecond lasers can be used to observe and control chemical reactions. Femtosecond lasers provide a light source with pulses in the same timescale as molecular vibrations. Thus molecules vibrate on a femtosecond timescale, hence a femtosecond light source is an ideal tool to observe chemical bond breaking and chemical bond formation [Carley *et al*., 2005]. Femtosecond laser research was started by the groups of Zewail years ago [Zewail, 1988].

Historically femtosecond laser sources used were dye lasers with gain media of 20 to 30 nm and approximately 30 fs pulses. The femtosecond light sources that are used currently are solid state lasers with gain media containing Ti^{3+}, Cr^{3+}, and Cr^{4+} doped in suitable crystals [Carley *et al*., 2005]. The femtosecond laser used for this study, which is shown in figure 3.13, uses a sapphire crystal doped with Ti^{3+} ions. The gain profile of this Ti:Sapphire laser ranges from 700 to 1000 nm but works best at approximately 800 nm [Gorjan, 2006]. For this work it was used at 795 nm. The amplifier that is usually used with the femtosecond laser for chemistry applications produces 1 mJ per pulse at a 1 kHz repetition rate with pulse duration between 20 and 100 fs. The technique used for this study was chirped pulse amplification producing 1 mJ pulses at a frequency of 10 Hz with duration of 120 fs.

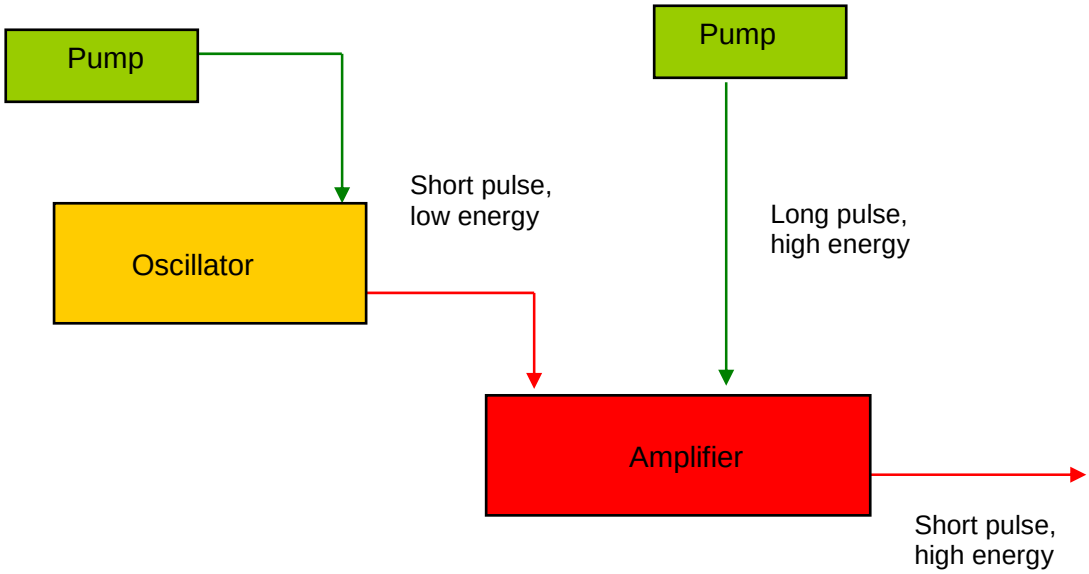

Figure 3.13: Schematic diagram of femtosecond laser system.

3.4. Time of flight mass spectrometry

Time of flight mass spectrometry (TOF-MS) is a method of separating ions of different masses based on the time needed for the ions to travel a fixed distance after

being accelerated in a potential field [http://www.fastcomtec.com, 09 June 2008]. The TOF-MS system shown in figure 3.14 is used to detect and measure the products (ions) obtained from the ionization and/or dissociation processes. In this study it was used in conjunction with nanosecond lasers (Nd:YAG laser and dye laser) and a femtosecond laser, where the laser radiation was used to ionize and/or dissociate the molecules. The laser parameters can be varied in order to investigate possible changes in the ionization and fragmentation ratios. There are four stages in the production and detection of ions within the time of flight mass spectrometer. These stages are: The production of ions from the sample in the ion source by using laser radiation, separation of the ions according to masses in the flight tube, detection of the number of ions of each mass produced in the detector, and collection of data to generate the mass spectra. These stages will be discussed separately in the next paragraphs.

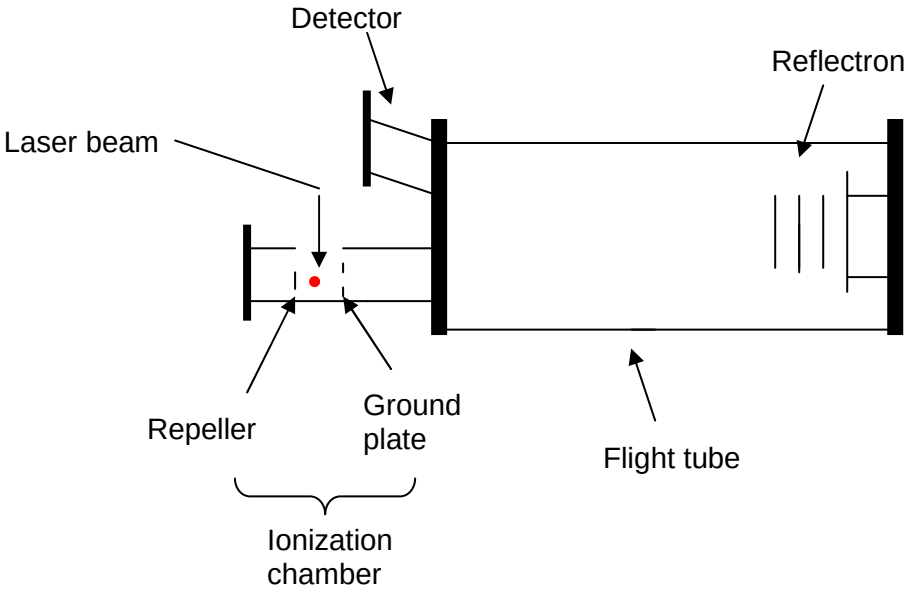

Figure 3.14: Schematic diagram of TOF-MS [http://elchem.kaist.ac.kr, 23 May 2008]

The time of flight mass spectrometer was introduced in the mid 1940's [Stephenson and McLuckey, 1996]. In the time of flight mass analyser, ions are accelerated by an

electric field in the ion source to the time of flight tube, to a kinetic energy of qV, where q is the ion charge and V is the applied voltage [http://elchem.kaist.ac.kr, 23 May 2008]. The electric field is defined by a voltage of the same polarity as the ions that will be recorded. These ions are then separated according to their mass-to-charge ratios (*m/z*) and then the time they took to reach the detector is measured. Ions with high mass-to-charge ratios will have a lower velocity and longer flight time than ones with low mass-to-charge ratio. The ions travel through the time of flight tube, from the ion source to the detector (a microchannel plate detector which consists of an array of glass capillaries (10-25 μm inner diameter) that are coated on the inside with an electron-emissive material) [http://elchem.kaist.ac.kr, 23 May 2008]. The reflectron redirects the ions back along the same flight tube at a different angle in order for the ions not to interfere with entering ions. The use of this reflectron increases the length of the total flight path and improves resolution by allowing more time for ions to separate with different mass-to-charge ratio [Yates, 1998]. The microchannel detector must be operated below 1 X 10^{-5} torr to avoid as many gas collisions as possible [http://elchem.kaist.ac.kr, 23 May 2008]. The detector records the charge induced or current produced when an ion hits the microchannel plate in the detector. The spectrum obtained can be shown on the oscilloscope, or recorded using data acquisition software and signal averager.

3.4.1. Ion production

Ions are produced by irradiating sample molecules with an ionization source such as an electron gun, or for this study, a pulsed laser [http://www.fastcomtec.com, 09 June 2008]. The laser energy is absorbed which causes the molecules to be excited, and to expel an electron. For all the ions to be analyzed clearly, they must be

simultaneously ejected from the ion source, which is achieved by using a pulsed laser.

3.4.2. Separation of ions

Ions are separated according to their mass-to-charge ratio in a vacuum environment in the flight tube. Different mass ions are accelerated to different velocities by the accelerating field, through a hole in the ground plate into the flight tube. Ions from the ion source enter the flight tube with the same kinetic energy and are separated inside the flight tube [http://elchem.kaist.ac.kr, 23 May 2008]. The flight tube must be pumped down to a good vacuum to prevent the ions, on the way to the detector, from colliding with background gas molecules. Thus the pressure in the flight tube must be lower than the pressure in the ion source.

3.4.3. Ion detection

Ions move along the flight tube to the reflectron where they are reflected back, move along the flight tube and eventually hit the detector. The ions are separated into individual packets by mass number. The detector will detect ions and produce an electric current from each bunch of ions, representing one mass, hitting the microchannel plate.

3.4.4. Function of the reflectron

The time of flight mass spectrometer has been known to have disadvantages in some configurations, for example having a low mass resolution under certain conditions [Cotter, 1997]. When ions are formed and a mass spectrum is observed,

there may under certain conditions be symmetrical peak tails around the expected peak due to the relatively large spatial distribution of the ion formation, which results in ions starting their flight journey at different positions, thus losing total mass resolution. However, mass resolution can be improved by incorporating reflectrons in the instrument. A reflectron is used to correct the kinetic energy distribution in the direction of ion flight [Ecelberger *et al*., 2004]. In the reflectron, an electrostatic field is used to reflect the ions towards the detector and, in this process, the faster ions of the leading edge of the peak travel further into the reflectron while the slower ions of the trailing edge of the peak do not move as far into the reflectron. This process results in a narrowing of the mass peaks if voltages are correctly applied to the reflectron plates.

Chapter 4

Literature background of 1,1,1-trichloroethane

4.1. FTIR and Raman spectra

There are several types of motions that contribute to the normal modes of vibration of molecules. For the molecule TCE, the vibrational modes are rocking (in-plane bending) and stretching vibrations, which are symmetric and asymmetric motions. The number of ways that the molecule can vibrate is related to the number of atoms and the number of bonds in the molecule. The number of normal vibrational modes of TCE is determined by using the equation 3N-6, where N is the number of atoms in the molecule. Since N=8 for TCE the number of vibrational modes of TCE is 18. This implies that 18 sets of absorption frequencies would be observed in the vibrational spectrum of TCE. However, several of the vibrations are degenerate, that is, the same amount of energy is required for some vibrations. Degenerate bands occur because TCE has one threefold axis. It should be noted that not all of the vibrations of the molecules produce infrared peaks due to the selection rules.

In most molecules the C-H bond stretching vibrations usually occur near 3000 cm^{-1} [McMurry, 2000]. The region from 1500 cm^{-1} to around 400 cm^{-1} is referred to as the fingerprint area, where C-C and C-Cl single bond vibrations occur if present in molecules. Usually fewer peaks are observed in an infrared spectrum than the calculated number of vibrational modes [McMurry, 2000]. Overtone peaks may be observed in the infrared spectrum. The overtone peaks normally occur at two or three times the frequency of a fundamental peak.

The infrared spectrum at ambient temperature of TCE in the liquid phase was previously measured and recorded in the range 200 to 3400 cm^{-1}, as summarized in table 4.1. Various authors found that TCE has three types of vibrations in the point group C_{3v}, which are A_1, A_2 and E. These types of vibrations were predicted by Herzberg [1945] and confirmed by Frankiss and Harrison [1975]. The bands that were observed by Frankiss and Harrison at 2939 and 3002 cm^{-1} were assigned to the symmetric and degenerate C-H stretching vibrations, v_1 (A_1) and v_7 (E) and the bands 1378 and 1445 cm^{-1} are assigned to the CH_3 deformation vibrations v_2 (A_1) and v_8 (E), respectively [Frankiss and Harrison, 1975]. The band at 1083 cm^{-1} corresponds to the degenerate CH_3 rocking vibration v_9 (E). The assignment of the A_1 and E fundamentals agrees with that of El-Sabban *et al*. [1951] and Stengle and Taylor [1970], but differs from that reported by Tanabe and Saeki [1972], who had assigned v_3 and v_{11} to bands at 1010 and 303 cm^{-1} respectively. The differences in v_3 and v_{11} values are possibly due to impurities.

The internal rotational or torsional vibration, v_6, is inactive as a fundamental in both the Raman and infrared regions. The torsion vibration was found to be active only in the solid state at 290 cm^{-1}. This result was confirmed by the far-infrared technique [Durig *et al*., 1971]. Rush found the peak for torsional oscillation of the methyl group at approximately 300 cm^{-1} [Rush, 1967]. Frankiss and Harrison [1975] showed that the torsion is also active in the Raman spectrum for the solid state at 4K as a weak band at 282 cm^{-1}.

Table 4.1: Infrared wavenumbers (cm^{-1}) of liquid phase TCE

Frankiss & Harrison [1975]	Tanabe & Saeki [1972]	Stengle & Taylor [1970]	Assignment	Description
		A_1 symmetric		
2939	2951	2943	v_1	C-H stretching
1378	1386	1384	v_2	CH_3 deformation
1070	1010	1070	v_3	C-C stretching
523	526	525	v_4	C-Cl stretching
344	344	343	v_5	CCl_3 deformation
		E Asymmetric		
3002	3013	3009	v_7	C-H stretching
1445	1455	1444	v_8	CH_3 deformation
1083	1088	1079	v_9	CH_3 rocking
712	724	711	v_{10}	C-Cl stretching
344	303	343	v_{11}	CCl_3 deformation
241	239	238	v_{12}	CCl_3 rocking

Raman spectra of the liquid phase of TCE were studied by various authors. Evans and Bernstein [1955] observed 10 active fundamental vibrational frequencies as recorded in table 4.2. The absence of v_{11} is believed to be caused by degeneracy with v_5. Thus an overlap between v_5 and v_{11} at 343 cm^{-1} was observed [Evans and Bernstein, 1955]. The assignments made by Stengle and Taylor [1970] compared excellently with the assignments made by Evans and Bernstein [1955]. Therefore all previously reported assignments of the vibrational frequencies of TCE agree reasonably with each other as shown in table 4.2.

Table 4.2: Active Raman absorption wavenumbers (cm^{-1}) of liquid phase TCE

Evans and Bernstein [1955]	Stengle and Taylor [1970]	Frankiss and Harrison[1975]	Prystupa *et al*.,[1989]	Assignments
2943	2938	2940	2939	v_1
1378	1384	1380	1375	v_2
1067	1071	1070	1072	v_3
521	525	523	521	v_4
343	343	346	340	v_5
3005	3009	3005	3003	v_7
1436	1444	1448	1444	v_8
1081	1079	1082	1085	v_9
712	711	710	710	v_{10}
343	343	341	341	v_{11}
239	238	241	238	v_{12}

4.1.1. Molecular symmetry

Molecular symmetry places significant limitations on possible electronic and vibrational energy levels and on chemical reactions involving breaking and forming of bonds. A symmetry operation is an action that leaves an object the same after it has been carried out [Herzberg, 1945]. Typical molecular symmetry operations include rotations, reflections and inversions of parts of the molecule. There is a corresponding symmetry element for each symmetry operation, which is the point, line, or plane with respect to which the symmetry operation is performed. Molecules

are classified according to their symmetries. The name of the group to which a molecule belongs is determined by the symmetry elements it possesses [Atkins and De Paula, 2002]. The various experimental tools that are utilised to solve structural problems in chemistry, such as Raman, FTIR, Nuclear Magnetic Resonance (NMR), magnetic measurements, and the diffraction methods (such as electron, X-ray and neutron diffraction), are based on symmetry considerations. Thus the concept of symmetry, as applied to molecules, is very important.

The axis of symmetry is determined by n, where the molecule is invariant when it is rotated by 360°/n. Therefore TCE has a 3-fold axis of symmetry, or a C_3 axis. Rotating TCE by 120° (C_3) will move Cl_2 into position of Cl_3 (figure 4.1).

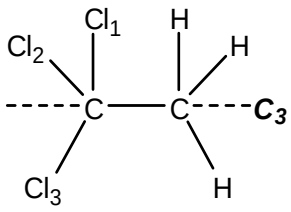

Figure 4.1: Molecular structure for TCE showing C_{3v} symmetry [Herzberg, 1945]

The direction of the C_3 axis is taken as horizontal, so a symmetry plane perpendicular to it is a vertical plane, σ_v, hence adding to the C_3 operation a vertical mirror plane, σ_v, and this forms the group termed C_{3v} [Herzberg, 1945]. Hence TCE belongs to the symmetry group, C_{3v}, with a staggered conformation (this is the most stable conformation with all three C-H and three C-Cl bonds as far away from each other as possible), see figure 4.2; as revealed by studies done by Frankiss and Harrison [Frankiss and Harrison, 1975].

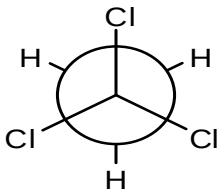

Figure 4.2: Staggered conformation for TCE

The symmetric elements of TCE are two 3-fold axis C_3 (2 x C_3), three planes of symmetry (3 X σ_v), and the symmetry operation of identity, I. The predicted symmetry types for TCE by Herzberg [Herzberg, 1945] are shown in table 4.3. There are two species of non-degenerate vibrations, both symmetric with respect to C_3 – one is symmetric with respect to the three planes σ_v, the other is asymmetric. They are called A_1 and A_2. The predicted symmetry by Herzberg was verified by several authors and confirmed in the present study. TCE has three types (species) of vibrations, which are A_1, A_2 and E. It has 18 normal vibrations. Of the twelve fundamental frequencies, five are totally parallel symmetric vibrations with species A_1, six perpendicular doubly degenerate vibrations with species E, which are allowed by selection rules in both Raman and infrared spectra, and one torsional vibration with species A_2, which is forbidden in both Raman and Infrared spectra [Frankiss and Harrison, 1975].

Table 4.3: Symmetry types (species) for the point group C_{3v} [Herzberg, 1945]

C_{3v}	I	$2C_3(z)$	$3\delta_v$	
A_1	+1	+1	+1	T_z
A_2	+1	+1	-1	R_z
E	+2	-1	0	T_x, T_y, R_x, R_y

4.2. UV absorption spectrum

UV absorption cross sections of TCE in vapour, gas and liquid phases have been measured by Vanlaethem-Meurée *et al*.[1979] and Nayak *et al*. [1995] in the wavelength interval of 180 - 240 nm, 160 - 240 nm and 235 - 260 nm. The temperature ranges used were 210 - 295 K and 220 - 330 K. Vanlaethem-Meurée *et al*. and Nayak *et al*. were interested to determine the lifetime of this molecule in the atmosphere and to know at which wavelength photolytic decomposition occurs. The wavelength and temperature dependency of the ultraviolet absorption cross section can be important in determining not only atmospheric lifetime of compounds, but also the altitude at which photodecomposition (and hence chlorine release to the atmosphere) occurs. The term cross section is used in physics to quantify the probability of particle-particle interaction, scattering, photo-absorption, etc.

Table 4.4 shows the results obtained by Nayak *et al.* [1995]; Vanlaethem-Meurée *et al.* [1979]*;* and Hubrich and Stuhl [1980]. The results reported by Nayak *et al.*, and Vanlaethem-Meurée *et al.* are in good agreement as shown in figure 4.3. This figure shows that absorption cross section decreases with increasing wavelength. Thus the absorption cross section is relatively small at longer wavelengths. The spectrum reported by Nayak *et al*. and Vanlaethem-Meurée *et al*. was measured at 295 K and the one reported by Hubrich and Stuhl was measured at 298 K. The gas phase absorption spectrum reported by Hubrich and Stuhl was thoroughly degassed at reduced temperature before it was used [Hubrich and Stuhl, 1980]. Figure 4.4 is a comparison of the liquid and gas phase absorption spectra [Nayak *et al*., 1995]. The liquid phase results reported were converted into effective gas phase cross sections using a wavelength shift procedure described and verified by Hubrich and Stuhl [Hubrich and Stuhl, 1980].

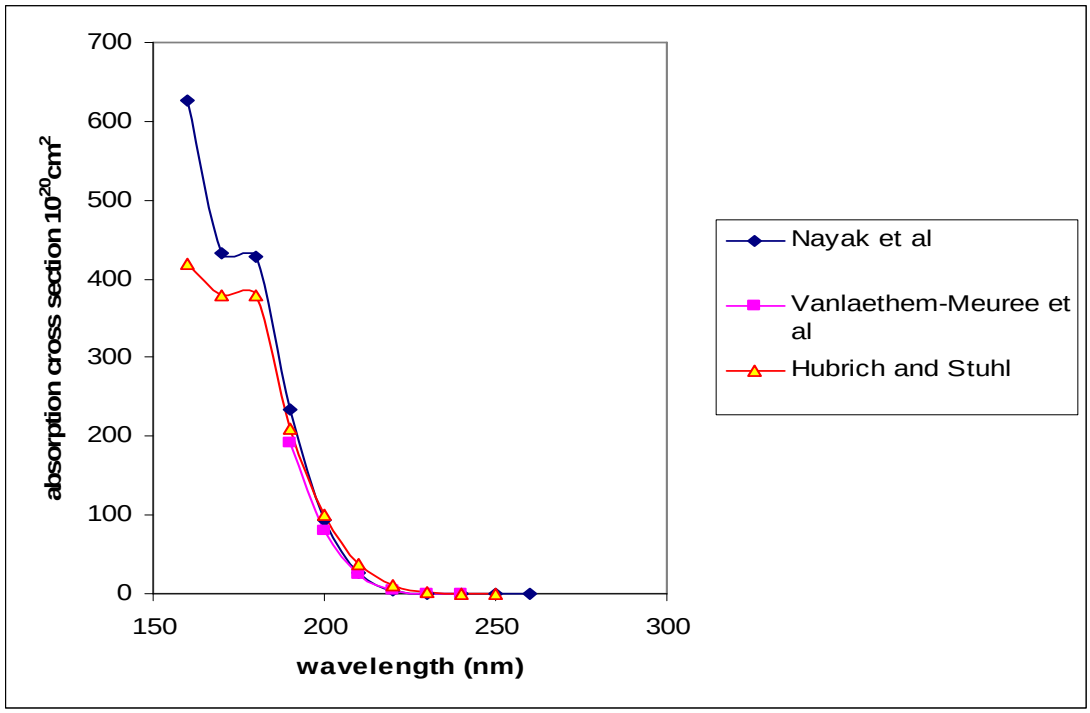

Figure 4.3: The gas phase absorption cross section of TCE: Comparison of values of Nayak *et al*. [1995], Vanlaethem-Meuree *et al*. [1979], Hubrich and Stuhl [1980]

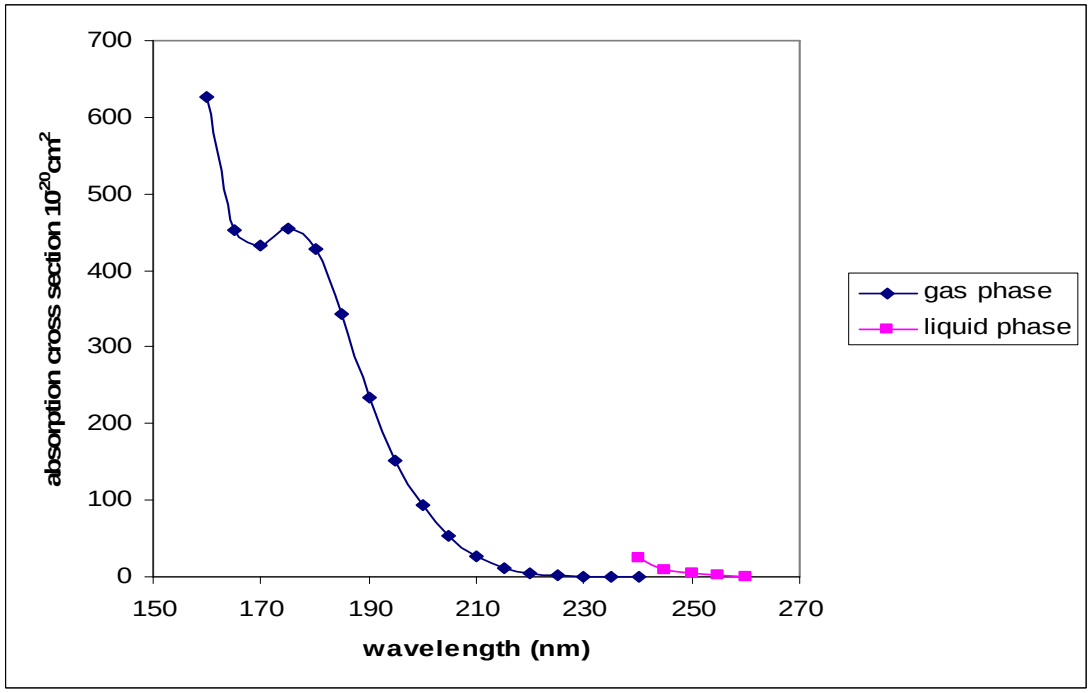

Figure 4.4: Absorption spectrum of TCE in the gas and liquid phase (liquid phase spectrum was measured from 240 to 260 nm) [Nayak *et al*., 1995].

Table 4.4: Gas phase absorption cross sections of TCE at different temperatures

Wavelength (nm)	Absorption cross section (x 10^{-20} cm^2)		
	σ_n (295K)	σ_v (295 K)	σ_h (298 K)
160	626		420
170	432		380
180	429		378
190	235	192	210
200	94.2	81.0	101
210	27.0	24.0	38.7
220	4.79	4.15	10.3
230	0.734	0.700	1.75
240	0.119	0.102	0.211
250	0.0156		0.0412
260	0.00232		

σ_n = cross section value for Nayak *et al*. [1995], σ_v reported by Vanlaethem-Meurée *et al.* [1979], and σ_h by Hubrich and Stuhl [1980].

4.3. Thermal decomposition of TCE

The thermal decomposition of TCE was investigated by Barton and Onyon [1950]. It was pointed out that saturated chlorinated hydrocarbons undergo thermal decomposition to the corresponding olefin or chloro-olefin and hydrogen chloride by two homogeneous mechanisms which are radical and unimolecular mechanisms. The authors expected the pyrolysis of TCE to proceed via a chain mechanism. The expected reactions are given in equations (1) and (2). TCE decomposed in the temperature range 635.7 to 707.0 K to give dichloroethene and hydrogen chloride.

The authors mentioned that the decomposition of TCE was not studied from a stoichiometric point of view; however, they expected the first stage to be represented by (1) and the second stage, which is much slower, by (2).

$CH_3CCl_3 \rightarrow CH_2{=}CCl_2 + HCl$ (1)

$CH_2{=}CCl_2 \rightarrow CH{\equiv}CCl + HCl$ (2)

The decomposition may proceed via at least two mechanisms but only the chain mechanism will be described as it seems to be the preferred mechanism [Barton and Onyon, 1950].

The initiation process may occur through three processes:

$CH_3CCl_3 \rightarrow \bullet CH_3CCl_2 + \bullet Cl$ (3)

$CH_3CCl_3 \rightarrow \bullet CH_3 + \bullet CCl_3$ (4)

$CH_3CCl_3 \rightarrow \bullet CH_2\,CCl_3 + \bullet H$ (5)

Of these equations (5) can be excluded on energetic grounds, thus the calculated activation energies for the three processes, assuming zero activation energy for the reverse reaction and with no allowance for substitution as compared with ethane and ethyl chloride, are (3) 80 kcal/mol (4) 85 kcal/mol. and (5) 97 kcal/mol [Steacie, 1946]. The succeeding reactions of the methyl and trichloromethyl radicals produced as in equation (4) are indicated below:

$\bullet CH_3 + CH_3CCl_3 \rightarrow CH_4 + \bullet CH_2CCl_3$

$\bullet CCl_3 + CH_3CCl_3 \rightarrow CHCl_3 + \bullet CH_2CCl_3$

followed by

$\bullet CH_2CCl_3 \rightarrow CH_2{=}CCl_2 + Cl$

The chain propagation steps may be represented by:

$\bullet Cl + CH_3CCl_3 \rightarrow HCl + \bullet CH_2CCl_3$ (6)

$\bullet CH_2CCl_3 \rightarrow CH_2{=}CCl_2 + Cl$ (7)

The termination process comprises interaction between a chlorine atom and the large chlorine containing radical; in the case of TCE this would imply [Barton and Onyon, 1950]:

$CH_2CCl_3 + \bullet Cl \rightarrow$ products (non-radical)

4.4. Laser photoionization mechanisms

Laser mass spectrometry has been used to dissociate or ionise molecules for number of years. During the multiphoton ionization, there are two mechanisms for fragmentation of molecules [Ledingham and Singhal, 1997]. The first mechanism is called dissociation followed by ionization or ladder switching. This means that the molecule can absorb one or more photons to reach a dissociative state below the ionization level. If the laser pulse length is longer than the lifetime of the state, the fragments formed during the process can ionise or fragment further depending on the laser intensity. The second mechanism is called ionization followed by dissociation or ladder climbing [Ledingham and Singhal, 1997]. If the laser pulse length is shorter

than the lifetime of the state the ionization level will be reached and the ion state can absorb further photons and subsequently can fragment into ions and neutrals. The ladder climbing mechanism is associated with picosecond and femtosecond pulses [Codling and Frasinski, 1993]. The ladder switching mechanism is associated with nanosecond pulses. These two mechanisms compete with each other but ladder climbing becomes dominant with decrease in pulse width, such as is the case for lasers with femtosecond or picosecond pulse widths.

Several authors used femtosecond and nanosecond laser pulses for different applications [Ledingham and Singhal, 1997]. Mullen and co-workers [2006] has used femtosecond and nanosecond laser pulses to extend the available methods used to detect the triacetone triperoxide (TATP) molecule. These two laser systems gave different results. The femtosecond laser system showed the parent ion signal with number of TATP decomposition products such as the acetyl ion and acetone ions. The parent molecule was not observed when using the nanosecond laser system. It was also concluded that there was no wavelength dependence observed in the femtosecond regime. However, the mechanism by means of which the TATP mass spectra were generated is not clear. The authors concluded that there might be a number of mechanisms active that contributed to the observed spectra of the TATP. In a review that was written by Ledingham and Singhal [1997] it was stated that it is not advisable to use the ladder switching mechanism for analytical purpose but it is believed to be suitable for molecular dissociative studies. Thus the current study used a similar experimental setup stated in the paper written by Mullen and co-workers [2006] to compare the results obtained when using different pulses.

Chapter 5

Experimental procedures, results and discussions for FTIR, Raman and UV-Vis techniques

5.1. Experimental procedures

All measurements were taken at room temperature. A Liquid sample of TCE was obtained from BDH Chemical Ltd., Poole, England, with maximum impurities of 0.1%. It was used without further purification. The cuvettes used for all the measurements were 1 cm quartz cuvettes and they are designed so that the light beam travels a distance of 1 cm through the contents.

5.1.1. FTIR absorption spectrometer

The instrument used to record FTIR and Raman spectra was Bruker's VERTEX 70 FTIR spectrometer coupled to a RAM II FT-Raman module. The FTIR spectrum was recorded in the region 400 to 3500 cm^{-1}. An empty cuvette was used to record background reference before conducting the experiment. The spectral resolution was 4 cm^{-1} and the number of scans collected per spectrum were 32. A deuterated L-alanine triglyrine sulphate (DLaTGS) detector with potassium bromide (KBr) windows was used, as well as a KBr beam splitter. Data was collected using Bruker optics software, OPUS 35, to obtain the spectrum.

5.1.2. FT- Raman absorption spectrometer

The Raman spectrum was recorded in the region 200 to 3500 cm^{-1}. A Nd:YAG laser at 1064 nm with laser power of 100 mW was used to excite the molecule. This laser power can be reduced to get a better spectrum if there is too much noise on the spectrum. Liquid nitrogen was used to cool the indium gallium arsenide detector (InGaAs) for approximately 30 minutes. The beam splitter used was calcium fluoride (CaF_2). The sample was placed in a cuvette in the Raman instrument for measurements. Only Raman Stokes lines were obtained for this study. The same software mentioned for the FTIR data collection was used. The spectral resolution was 4 cm^{-1}.

5.1.3. A single beam UV-Vis absorption spectrometer

The UV-Vis spectrometer was calibrated by measuring the absorption spectrum of a standard Hg-Ar lamp. The UV spectrum of TCE in liquid phase in the range 200 to 900 nm has been obtained using the USB-ISS-UV-Vis Integrated Sampling Systems Lamp source and the USB2000 spectrometer from Ocean Optics. The spectrometer was interfaced to a computer with a USB 2.0 port. The USB-ISS-UV-Vis Integrated Sampling Systems Lamb source has a direct attached sample holder and deuterium tungsten halogen light source combinations for the 1 cm square cuvette. The deuterium lamp was for the UV part of the spectrum and a tungsten halogen lamp for the visible region. The light source range is 200 to 2000 nm. The detector used in this spectrometer was a CCD array detector. The data on the reference was taken first, followed by the data on the sample. The absorbance of the analyte was determined by taking the difference between the data obtained for the reference and the sample. Thus the absorption spectrum of TCE was obtained by subtracting the data of the

reference from the data of the sample. Origin software was used to process data for generation of the spectrum.

5.2. Results and discussions

5.2.1. Infrared spectrum

The experimental vibrational wavenumbers for TCE were determined by FTIR and FT-Raman measurements at room temperature. The normal modes of the molecule were assigned and summarized in table 5.1. The results were compared with previously reported results. Computational methods were also used to assign the bands on the spectrum (see section 2.3.1.2). The observed FTIR spectrum for TCE is shown in figure 5.1. The FTIR spectrum was calculated using DFT at the B3LYP/ 6-31G* level of computation and the wavenumbers are recorded in table 5.1. The computed spectrum is shown in section 2.3.1.2 and it was compared with the observed spectrum. The peaks observed at 1557, 2361, 2343 and 1204 cm^{-1} are due to impurities. The peaks at 2833 and 2944 cm^{-1} are assigned to the symmetric and degenerate C-H stretching vibrations, v_1 (A_1) and v_7 (E) and the peaks at 1383 and 1426 cm^{-1} are assigned to the CH_3 deformation vibrations, v_2 (A_1) and v_8 (E), respectively. A peak at 1086 cm^{-1} corresponds to the degenerate CH_3 rocking vibration, v_9 (E). The peaks were observed from 400 to 3500 cm^{-1} because the instrument cannot detect anything below 350 cm^{-1}. All recorded and previously reported normal modes are in reasonable agreement with each other.

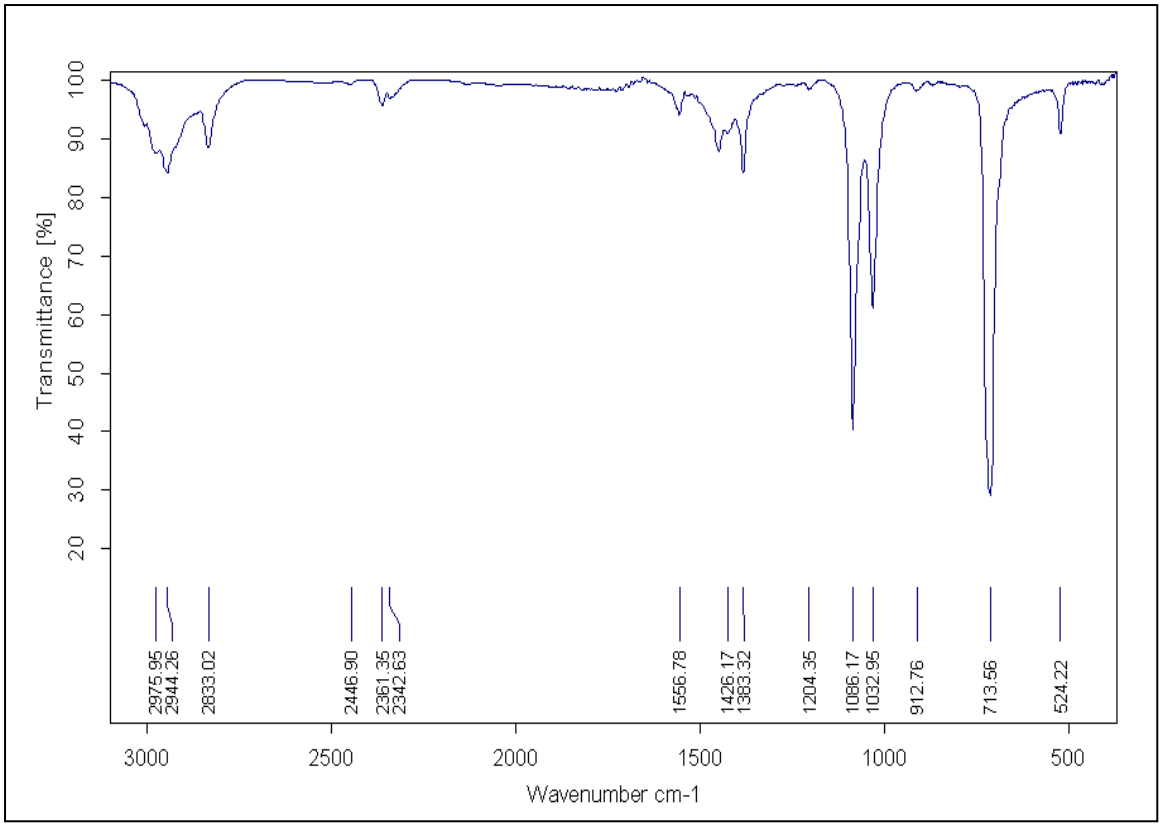

Figure 5.1: Experimental FTIR spectrum of TCE in liquid phase

Table 5.1: Infrared wavenumbers (cm^{-1}) of liquid TCE

Observed	Calculated	Literature			Description
		Frankiss & Harrison [1975]	Tanabe & Saeki [1972]	Stengle & Taylor [1970]	
		A_1 symmetric			
2833	3082	2939	2951	2943	C-H stretching
1383	1442	1378	1386	1384	CH_3 deformation
1033	1073	1070	1010	1070	C-C stretching
524	517	523	526	525	C-Cl stretching
------	345	344	344	343	CCl_3 deformation
		E Asymmetric			
2944	3168	3002	3013	3009	C-H stretching
1426	1510	1445	1455	1444	CH_3 deformation
1086	1117	1083	1088	1079	CH_3 rocking
714	691	712	724	711	C-Cl stretching
-----	344	344	303	343	CCl_3 deformation
-----	239	241	239	238	CCl_3 rocking

5.2.2. Raman spectrum

The observed and previously reported Raman absorption frequencies for TCE are recorded in table 5.2. The observed FT-Raman spectrum for TCE is given in figure 5.2. A broad peak at around 2886 cm^{-1} and small peak at 2742 cm^{-1} are believed to be overtone peaks, as overtone peaks are usually at about twice the wavenumber of a fundamental. The deformation bands are located at lower wavenumbers than stretching vibration bands because deformation in a molecule requires less energy. All reported and observed frequencies are comparable with each other.

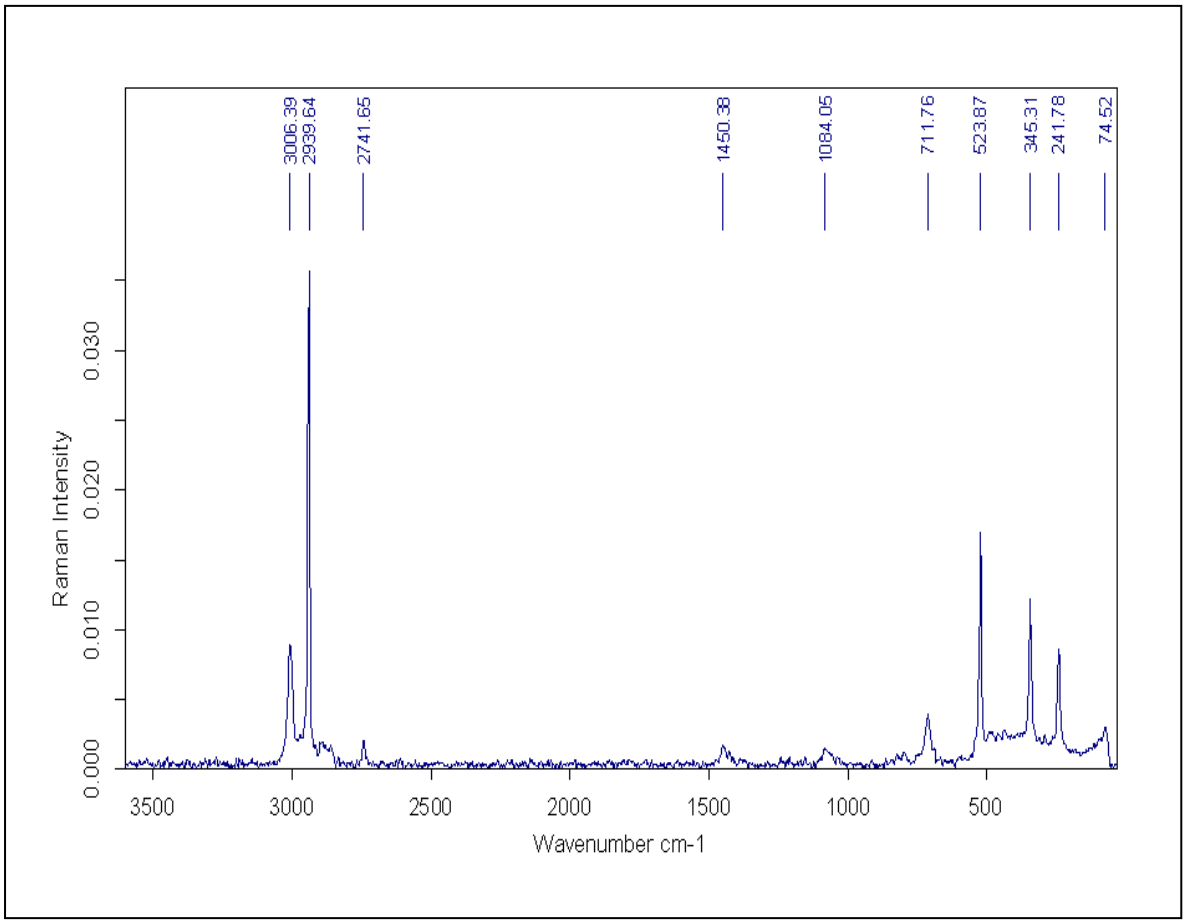

Figure 5.2: Experimental FT-Raman spectrum of TCE in liquid phase

Table 5.2: Raman absorption wavenumbers in cm^{-1} of liquid TCE

Evans and Bernstein [1955]	Stengle and Taylor [1970]	Frankiss and Harrison[1975]	Prystupa *et al*.,[1989]	Observed	Assignments
2943	2938	2940	2939	2940	v_1
1378	1384	1380	1375	1380	v_2
1067	1071	1070	1072	1069	v_3
				912	
521	525	523	521	524	v_4
343	343	346	340	345	v_5
3005	3009	3005	3003	3006	v_7
1436	1444	1448	1444	1450	v_8
				1420	
1081	1079	1082	1085	1084	v_9
712	711	710	710	712	v_{10}
343	343	341	341	345	v_{11}
239	238	241	238	242	v_{12}

5.2.3. UV-Vis spectrum

Figure 5.3 shows the liquid phase UV spectrum of TCE. The UV-Vis spectrometer used absorbs from 200 nm. There is noise observed below 200 nm and this was due to the glass (cuvette) absorbing in that wavelength or the lamp. The molecule TCE absorbs light strongly in the UV region and does not absorb in the visible region, as shown in the figure. The absorption wavelength depends on the presence of particular chromophores (absorbing groups) in a molecule. In this case, CCl_3 is the absorbing group. The CCl_3 in TCE has a sigma bonding and non-bonding electrons. This means that the electrons can be excited from sigma bonding to sigma anti-bonding orbitals, $\sigma \rightarrow \sigma^*$, and non-bonding to sigma anti-bonding orbitals, $n \rightarrow \sigma^*$, as shown in figure 5.4. The non-bonding orbital has a higher energy than sigma bonding orbital. This means that the jump from a chlorine lone pair into sigma anti-bonding orbital needs less energy. This implies that light of a lower frequency was absorbed

and therefore a higher wavelength. Thus TCE absorbs light at two different wavelengths:

1) the sigma bonding to sigma anti-bonding absorption peak, which is in the deep UV which was not observed as the spectrometer operates only from 200 nm; and
2) the non-bonding to sigma anti-bonding absorption peak, which is in the UV region.

The information obtained from the UV spectrum can be used in determining the energy of the electronic excitation state of the molecule which corresponds to the absorbing wavelength.

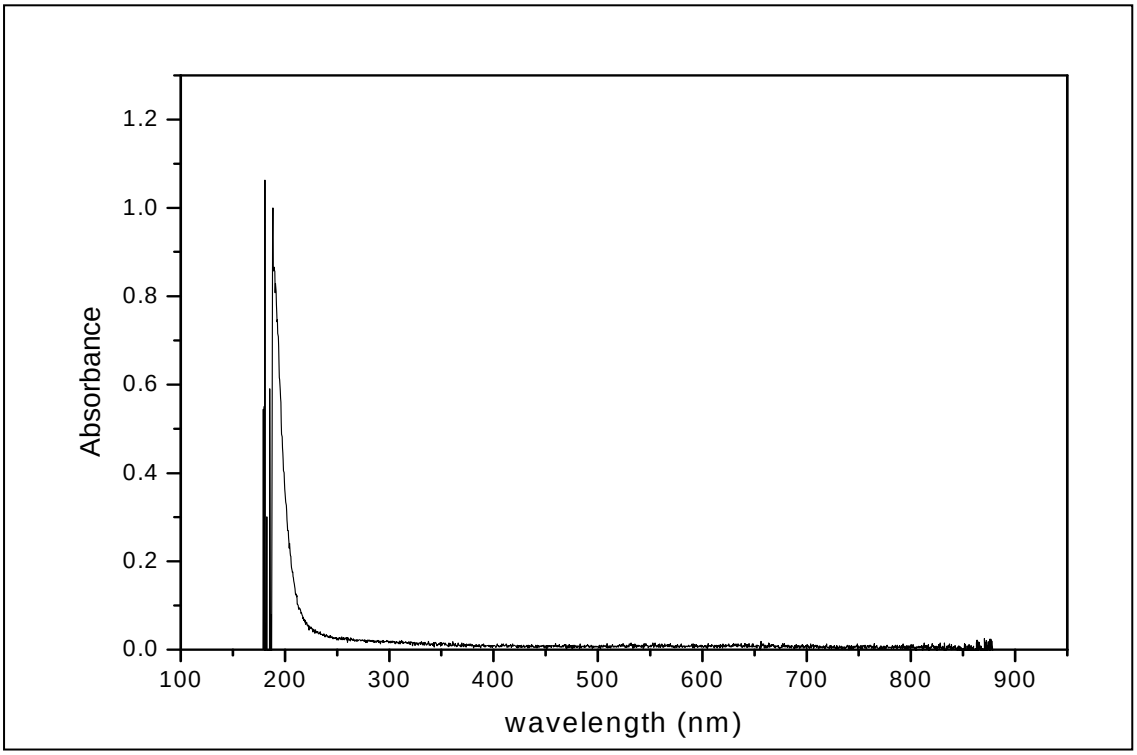

Figure 5.3: The measured ultraviolet spectrum of TCE in liquid phase.

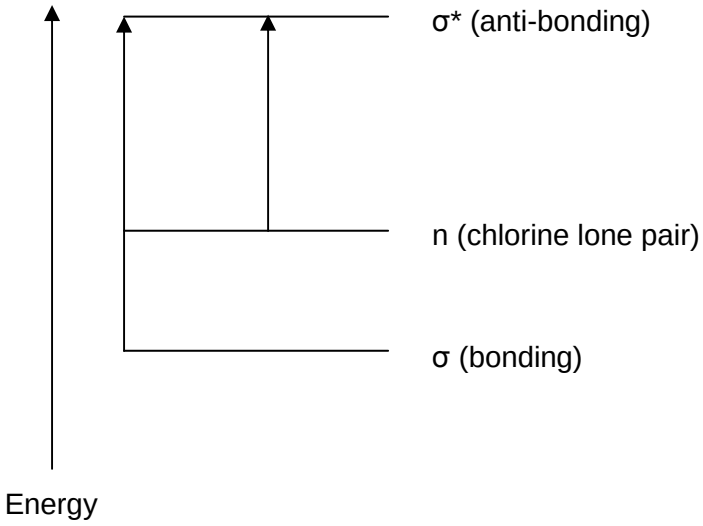

Figure 5.4: Assumed UV energy diagram for TCE (not to scale)

Chapter 6

Laser photoionization experimental procedures, results and discussions

6.1. Experimental Procedures

A reflectron Time of Flight Mass Spectrometer (TOF-MS) was used in all experiments to analyse product formation. The gas sample was introduced by a pulsed supersonic expansion valve (General Valves, Series 9) driven by a pulse driver (Iota One, General Valve Corporation). A delay / pulse generator (also known as a digital delay generator from Stanford Research Systems Inc., DG535) was used to trigger the laser, the pulse driver and a 200 MHz digitizing oscilloscope (Tektronix TDS, model 360). The delay time between the gas pulse and laser pulse was varied and the gas pulse duration was set to 180 μs. This delay between the time that the valve opens, releasing sample gas, and the time that the laser pulse is emitted, was controlled by suitably adjusting the delay generator.

A schematic diagram of the TOF-MS indicating the path of the ions is shown in figure 6.1. There are two vacuum pumps which are situated under the ionization chamber and flight tube which are not shown in the figure. The gas sample in the ionization chamber was irradiated by a pulsed laser to produce ions. The produced ions travel through the flight tube to the reflector and hit the detector as shown in the figure. A set of repeller plates was used to accelerate the ions into the flight tube. The generated atomic and molecular ions were extracted into the 70 cm flight tube. The ions formed were measured by a detector consisting of a microchannel plate

(Hamamatsu, model F1552-01) and electron multiplier (Hamamatsu, model R2362). The signals obtained were observed on the oscilloscope. Prior to observation on the oscilloscope, the signal was further amplified by an amplifier (Hamamatsu, model C5594). The system used is designed to accelerate positive ions to the detector, thus all ions observed are positive. The lighter ions will appear first and heavier ions appear last on the mass spectrum.

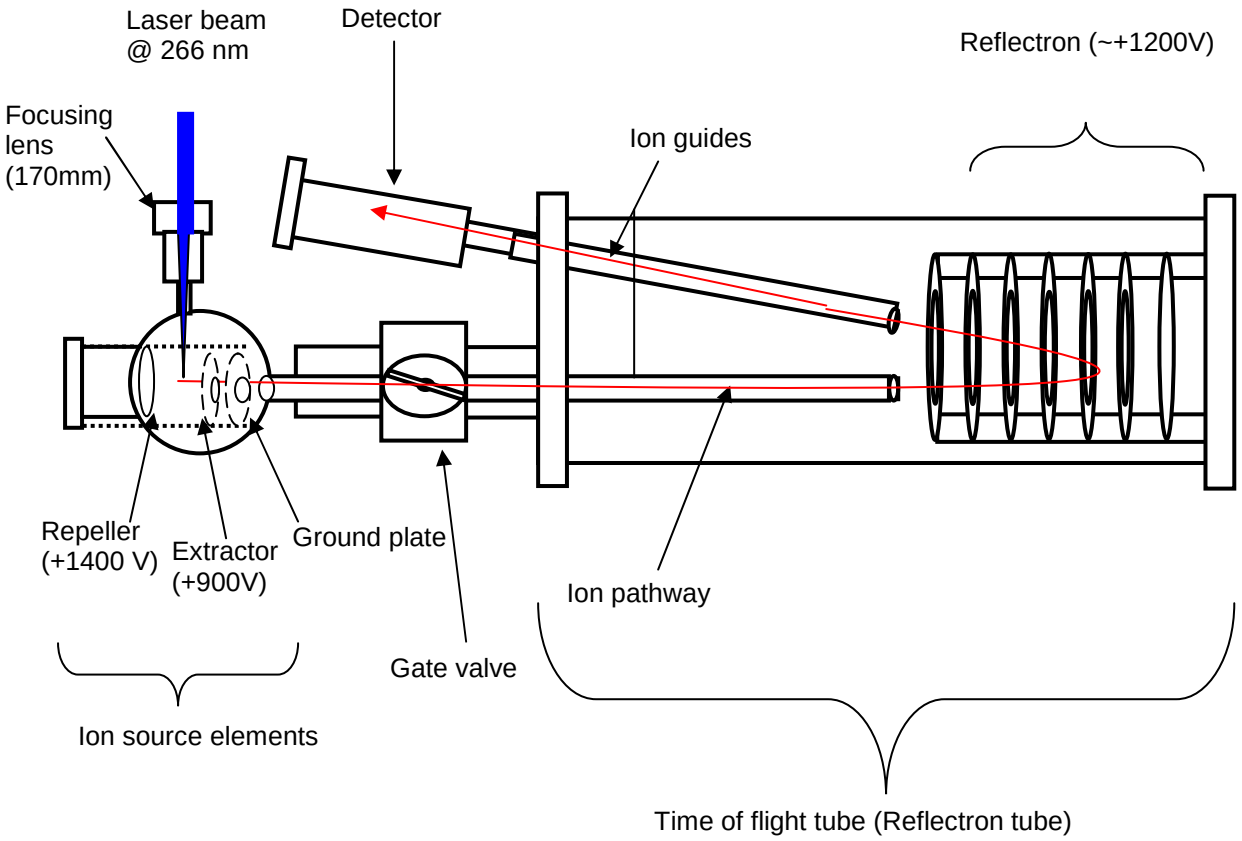

Figure 6.1: Schematic diagram of TOF-MS showing the path ions travel

Ions were formed in gas phase by multi-photon ionization by the laser in the centre of the ion source. Argon gas was used as a carrier gas for the gas sample. The vacuum pressure of the instrument was in the range of 10^{-6} to 10^{-5} torr. The ion source and flight tube were pumped by turbomolecular pumps backed by rotary vane pumps. Ion

gauges were used to measure the vacuum pressure. The data collected from the oscilloscope was used to plot the ion signal versus the flight time of the ions. Origin Software was used to process data for generation of the mass spectrum. Delay scans were obtained by observing the ion signal as a function of delay time between gas and laser pulses. As a characterization of the system, ion signals were observed as a function of focusing position of the lens, as a function of laser energy and as a function of carrier gas backing pressure for the nanosecond laser system only.

6.1.1. Experimental setup for the time of flight using nanosecond laser pulses

6.1.1.1 Introduction

A simple schematic diagram of the timing in the experimental setup for nanosecond laser ionization is shown in figure 6.2. A pulsed laser beam hits the gas sample molecules in the ion source of the TOF-MS system causing ionization. The gas sample was introduced by a pulsed gas jet and controlled by a pulse driver. The gas molecules will interact with the laser beam, which was triggered by a pulse generator. The ions that are formed with different masses are then detected by the detector. The mass spectrum of the sample was observed on the oscilloscope and the data was collected with the data system (Origin software).

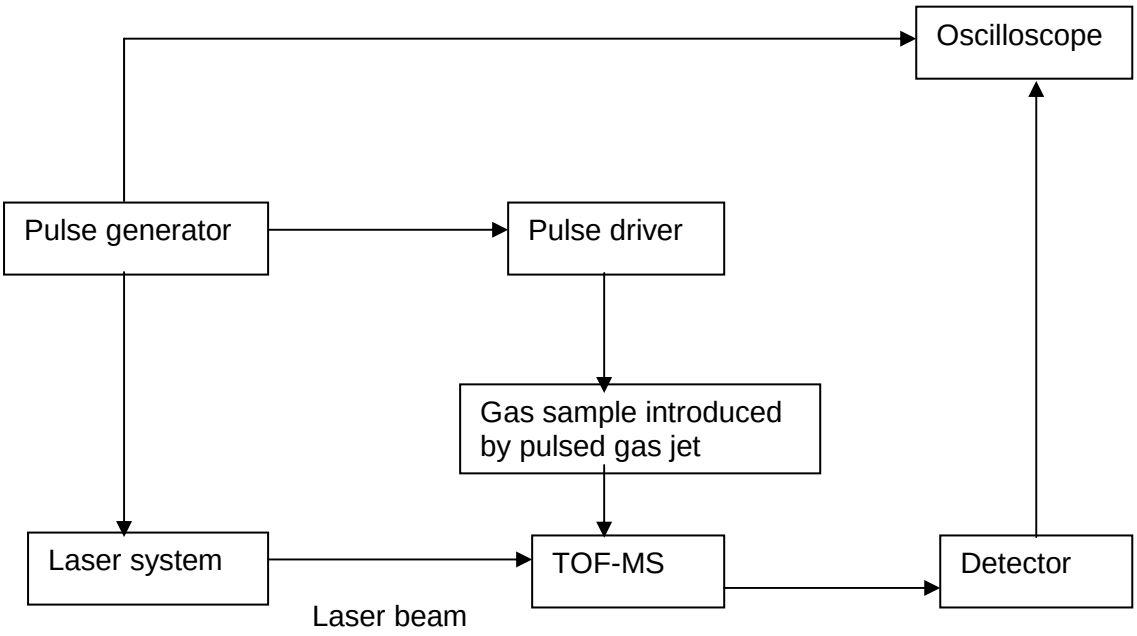

Figure 6.2: Schematic diagram of the timing in the experimental setup for nanosecond laser ionization

6.1.1.2. Experimental conditions

The wavelengths chosen for the nanosecond laser experiments were 1064 nm, 532 nm, 266 nm, 425 nm and 212.5 nm. The laser pulses were focused into the gas sample with a lens of 170 mm focal length. The pulse repetition rate for the Nd:YAG and the dye laser were set at 10 and 2 Hz, respectively. The Nd:YAG laser produced 6 ns pulses with energy of 2.9 mJ per pulse at a wavelength of 266 nm. The dye laser producing 6 ns pulses with energy of 150 μJ at wavelength 212.5 nm was also used for the ionization of TCE. All other conditions were kept identical, including the valve open time (gas pulse duration setting) of 180 μs and the laser pulses of 6 ns, except the delay times for the gas. The delay times were changed because there were no ion signals when the delay time was at 150 μs when using the Nd:YAG laser, and there were no ion signals when the delay time was at 350 μs when using the dye laser. This is an indication of differences in the time for laser pulse delivery

from the time of trigger signal due to the difference in operation of the two laser systems. Thus the optimal delay time was found in each case in order to observe the best ion signals of TCE ion fragments. The signal averaging used when taking the measurements on the oscilloscope was 32. The lasers used in this study for ionization of TCE were nanosecond and femtosecond lasers. The nanosecond lasers used were the dye laser (Lambda Physik 3400, Göttingen, W. Germany) and the Nd:YAG laser (Continuum Surelite, model SLI/10).

6.1.1.3. Nd:YAG laser

The Nd:YAG laser used for this study is the same as the one shown in figure 3.8. This laser was pumped by a flash lamp and it was operated in a pulsed Q-switched mode. The Q-switch was used in this laser to improve the pulse duration from 250 μs to 6 ns. A Brewster angle window was used to linearly polarize the laser output. The ½ λ plate was placed after the output coupler to change the horizontal polarization into vertical polarization because the output beam of the laser is horizontally polarized and the input beam to the 2^{nd} harmonic crystal needs to be vertically polarized.

The second and fourth harmonics were obtained by doubling and quadrupling the frequency as shown in figure 6.3. The 1064 nm was frequency doubled by using a frequency doubling crystal to produce both 1064 nm (near IR) and 532 nm (green light) beams and these beams were split, using a dichroic optical window (which selectively reflects one wavelength and transmits the other). The 1064 nm beam is dumped and the 532 nm is partially frequency doubled with a second frequency doubling crystal to produce a combined 532 and 266 nm beam. The combined 532 nm and 266 nm beam is split again, this time using a Pellin-Broca beam splitting

crystal to give a 532 nm beam, which is dumped and the 266 nm beam, which is focused with a lens of 170 mm focal length. This lens focuses the laser beam of 266 nm in the ionization chamber of the TOF-MS.

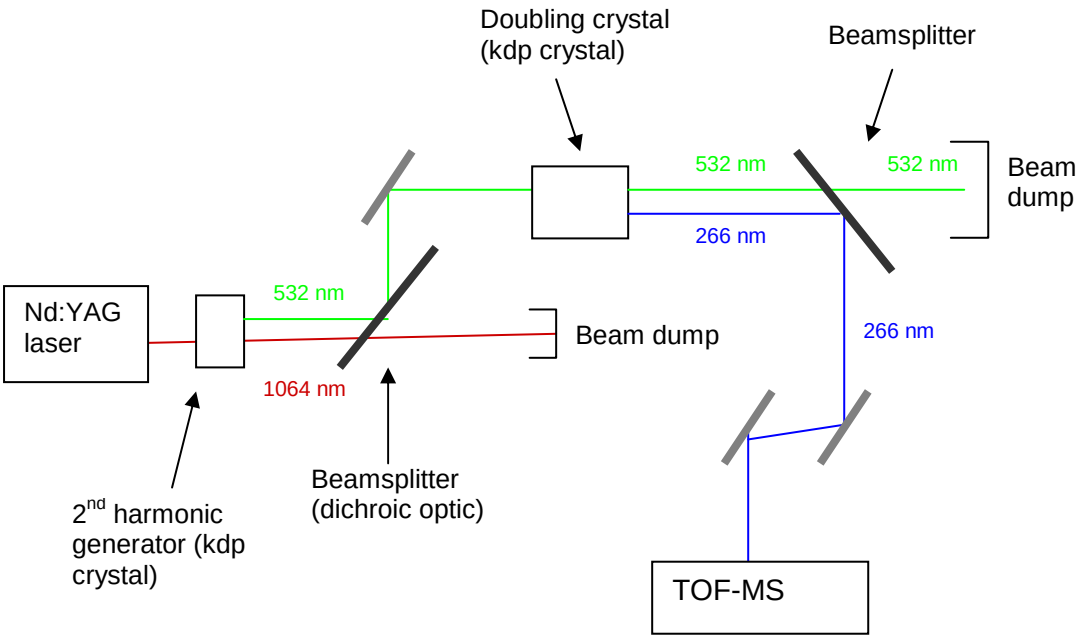

Figure 6.3: Schematic diagram showing the doubling and the quadrupling of the frequency of the Nd:YAG laser beam

6.1.1.4. Dye laser

The dye laser used for this study was operated in pulsed mode and was pumped by an excimer laser (XeCl Lambda Physik Model EMG 201). This laser is schematically presented in figure 6.4. There is a lens, used to minimise beam divergence, which is situated between excimer laser and dye laser not shown in the figure. The laser beam was sent to a BBO crystal, which is used to double the frequency to shorter wavelengths in the deep UV spectral region. A beamsplitter (Pellin-Broca crystal) was used to split the dye laser beam and the frequency doubled dye laser beam. This dye laser beam was dumped and the frequency doubled beam was focused

using a 170 mm focal length lens in order to excite the gas molecules in the ion source of the TOF-MS system. The grating was used in the laser cavity to perform selective tuning. However in this experiment one particular wavelength was selected. The dye used in the dye laser was Stilbene, which allows us to obtain the wavelength of 425 nm and the frequency doubled output at a wavelength of 212.5 nm.

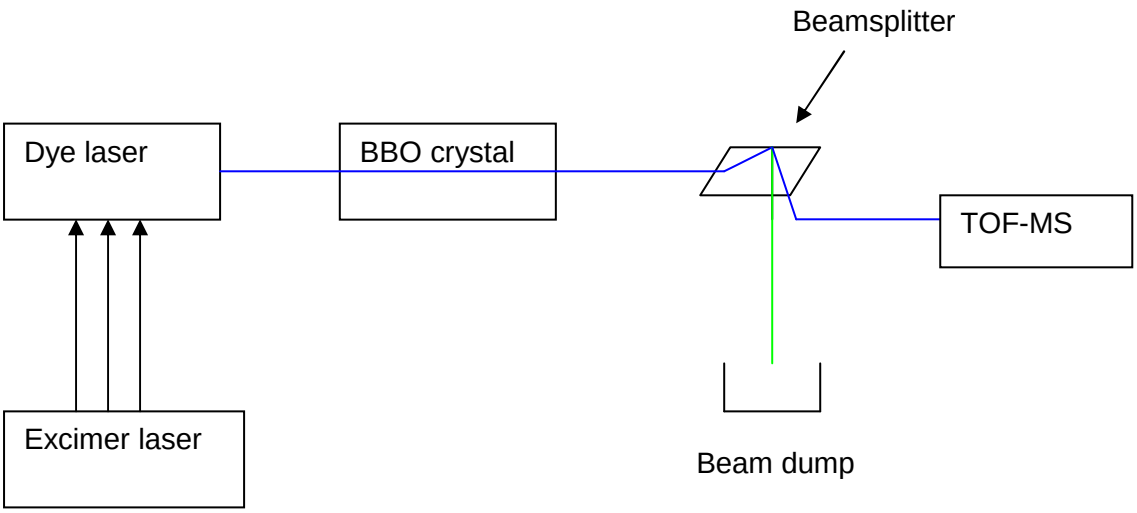

Figure 6.4: Schematic diagram showing the doubling of the frequency of the dye laser beam

6.1.2. Experimental setup for the time of flight using femtosecond laser pulses

A simple schematic diagram of the timing in the experimental setup for the femtosecond laser ionization is shown in figure 6.5. A photodiode, placed in front of the ionization chamber of the TOF-MS, was used to trigger the oscilloscope. The laser was triggered by a delay generator which is not shown in the figure. The laser beam ionizes the molecules in the ionization chamber of the TOF-MS. The ions are detected by the detector and the mass spectra will be observed on the oscilloscope.

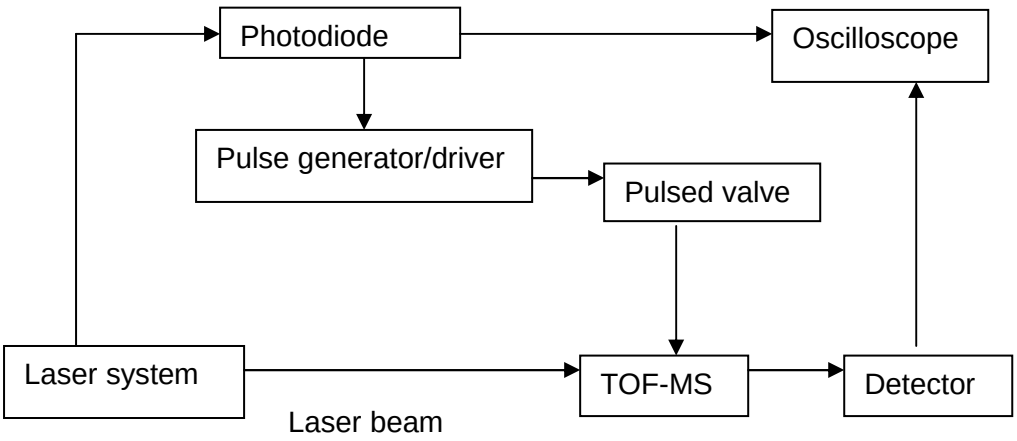

Figure 6.5: Schematic diagram of the timing in the experimental setup for the femtosecond laser system

The femtosecond laser (Coherent, Inc.) of 795 nm shown in figure 6.6 was used. This laser consists of an oscillator, regenerative amplifier, pump lasers, and optical parametric amplifier (OPA). The optical system used to generate the femtosecond pulses was a Ti:Sapphire oscillator (Mira oscillator), which is mode-locked and emits pulses of approximately 120 fs at a repetition rate of 76 MHz, coupled with a regenerative amplifier that is pumped by a Q-switched solid state laser. This pump laser delivers approximately 10 mJ per pulse of 250 ns duration at repetition rate of 1 kHz. The oscillator was pumped by the Verdi pump laser, which is a 5 W continuous wave Nd:YVO_4 laser. The laser pulse from the oscillator was sent into the amplifier which consists of the pulse stretcher, regenerative amplifier cavity and pulse compressor. The amplification of the oscillator pulse takes place in a Ti:Sapphire crystal. The amplified pulse was compressed to deliver short pulses of approximately 120 fs with high energy of 1 mJ per pulse at repetition rate of 1 kHz. The polarizer, which is placed before the BBO crystal, is used to attenuate the laser beam.

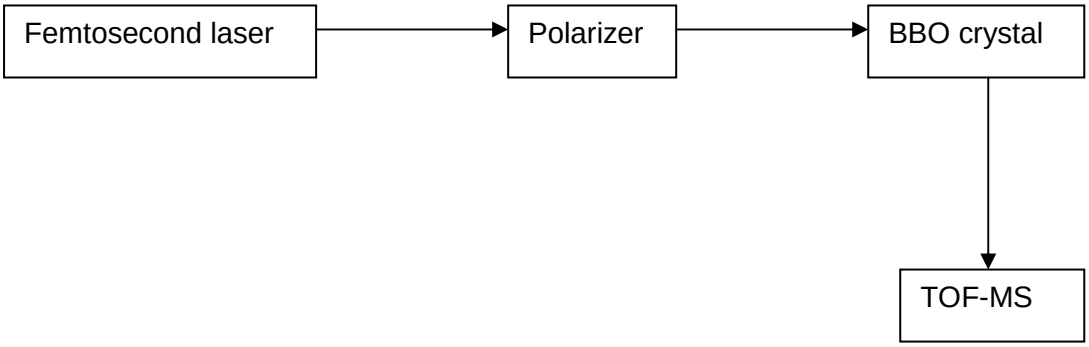

Figure 6.6: Schematic diagram showing the experimental setup for the time of flight using femtosecond laser beam for ionization of TCE

The second harmonic was obtained by doubling the frequency as shown in figure 6.7. The 795 nm beam was frequency doubled by using a frequency doubling crystal (BBO crystal) to produce both 795 nm (red light) and 397.5 nm (blue light) beams and these beams were split using dichroic mirrors, which selectively reflects one wavelength and transmits the other. The 795 nm beam was dumped and the 397.5 nm was focused with a lens of focal length 170 mm. The lens focuses the laser beam of 397.5 nm in the ionization chamber of the TOF-MS. There are also two broadband dielectric mirrors, which are not shown in the schematic diagram, which are used to direct the laser beam straight to the lens which focuses the laser beam into the ionization chamber. The BBO crystal used works at an optimal angle relative to the polarization of the laser beam, and this was optimized by rotating the BBO crystal.

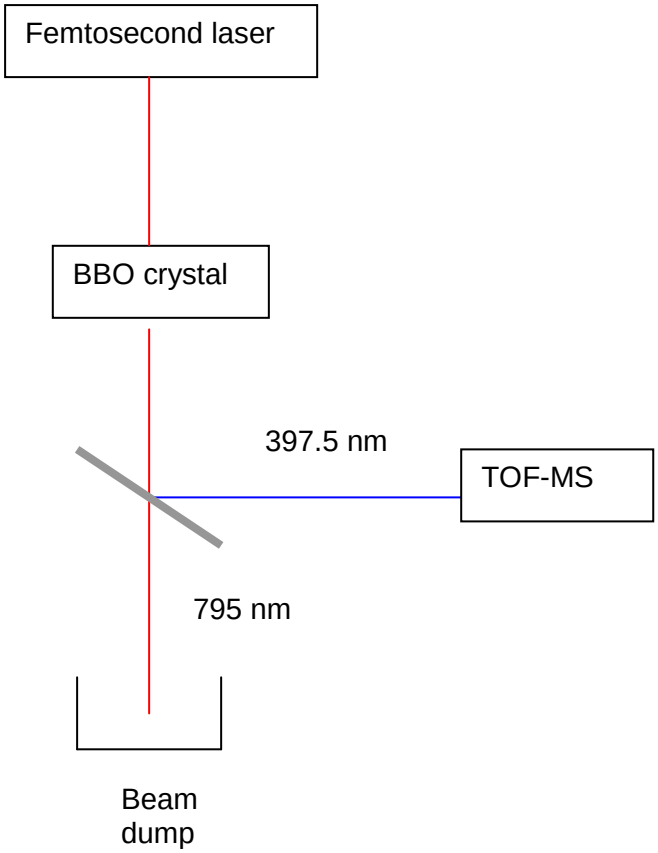

Figure 6.7: Schematic diagram showing the doubling of the frequency of the 795 nm laser beam

6.2. Results and discussions

6.2.1. Calibration of the time of flight system using nanosecond and femtosecond laser pulses

The instrument was calibrated by measuring the N_2O gas spectrum using femtosecond and nanosecond laser pulses. The recorded spectra are presented in figure 6.8 and summarized in table 6.1. This was used to determine the calibration factor, k. The data collected was converted from time values to mass values by using the mathematical equation, $t = k\sqrt{m}$, where t is the flight time of the ions, k is a

calibration constant specific to the system, and *m* is the mass of the ions (velocity is inversely proportional to the square root of mass) [http://www.thefreedictionary.com, 17 June 2008]. The mass spectra taken with the 266 nm nanosecond pulse ionization and 795 nm femtosecond pulse ionization of N_2O gas are comparable; that is, they both have O^+, N^+, and N_2^+ ion signals. The N_2O^+ ion signal (parent ion) was obtained when using femtosecond laser pulses but not with nanosecond laser pulses, as expected from the literature. There was a strong NO^+ ion signal that was observed when using nanosecond laser pulses and absent when using femtosecond laser pulse. All of the above implies that there is much less fragmentation occurring with the femtosecond laser at 795 nm. There was also a strong O_2^+ and water vapour ion signals present when using femtosecond laser pulse but absent when using nanosecond laser pulse due to the leakage in the system. The strong Ar^+ ion signal observed when using femtosecond laser pulses was due to the argon gas being used as carrier gas and the “easy” ionization taking place when using femtosecond pulses. The overshoot in the mass spectrum in the femtosecond regime was due to the peak being strong and the electronic mismatch of impedances in the amplifier system. It was observed that more ion signals were obtained when using femtosecond laser pulses.

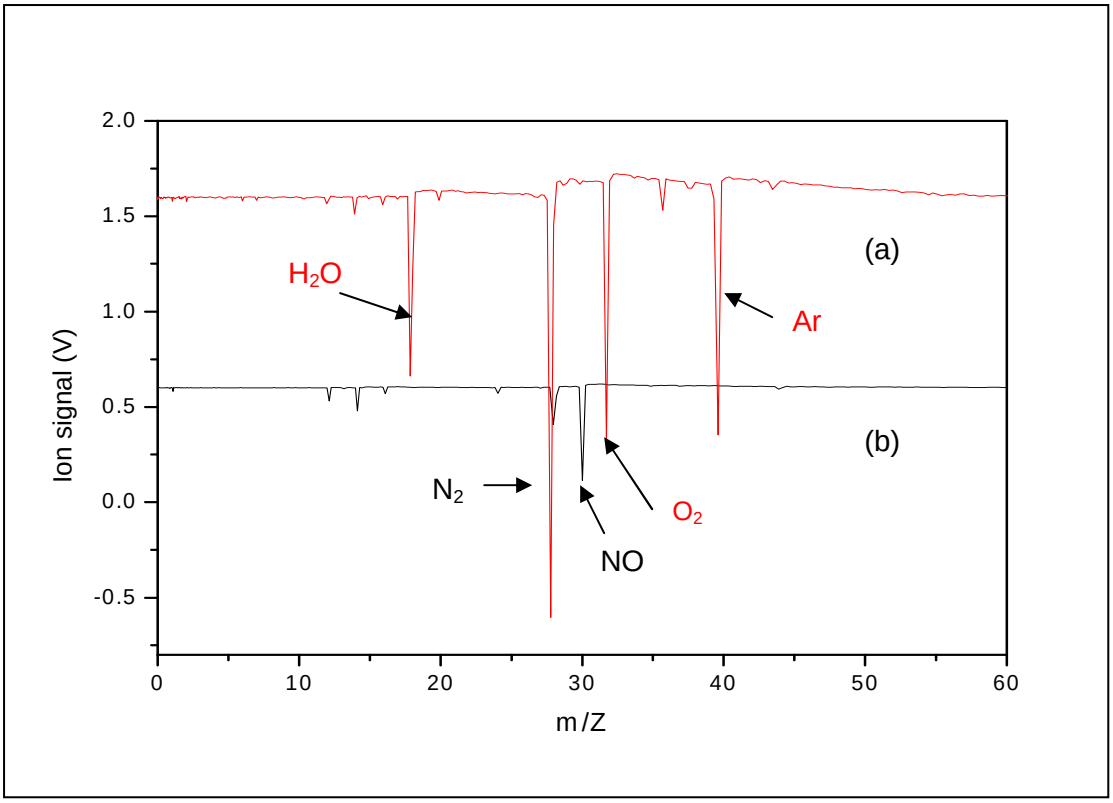

Figure 6.8: Measured time of flight mass spectra of N_2O gas (a) using femtosecond laser at 795 nm, 120 fs, 1 mJ and (b) nanosecond laser at 266 nm, 6 ns, and 2.9 mJ pulses

Table 6.1: Assigned ion signals of the N_2O gas mass spectra

Time (μs)		Masses (m/Z)	Ion peaks
Femtosecond	nanosecond		
16.3	16.4	12	C^+
17.7	17.7	14	N^+
18.9	18.9	16	O^+
20	-	18	H_2O^+
20.9	-	20	Ar^{++}
25	24.9	28	N_2^+
-	25.8	30	NO^+
26.7	-	32	O_2^+
29.5	-	40	Ar^+
31.2	-	44	N_2O^+

6.2.2. Conditions for optimization of TOF-MS system using nanosecond laser pulses

For the TOF-MS system to be optimised, and for the ions to be detected optimally, there are certain conditions that need to be considered. These conditions are the focusing position of the lens, the time delay between gas and laser pulses, the gas pulse duration, and the laser pulse energy. When adjusting these conditions, selected ion signals can be enhanced. The optimal conditions were determined using the nanosecond laser (Nd:YAG laser) at 266 nm and are discussed below. Four ion peaks in the mass spectrum shown in figure 6.9 ($^{35}Cl^+$, $C^{35}Cl^+$, $HC_2{}^{35}Cl^+$, and $H_2C_2{}^{35}Cl_2{}^+$) were selected for optimisation of the TOF-MS system because they appear as strong peaks during photoionization of TCE. One chlorine isotope $^{35}Cl^+$ was selected due to its environmental relevance – it is believed that the chlorine atom migrates to the stratosphere causing the depletion of the ozone layer (see section 1.1). The parameters that were changed include the defocusing position of the lens, the delay time between the gas and laser pulse, the laser energy and the backing pressure (carrier gas pressure).

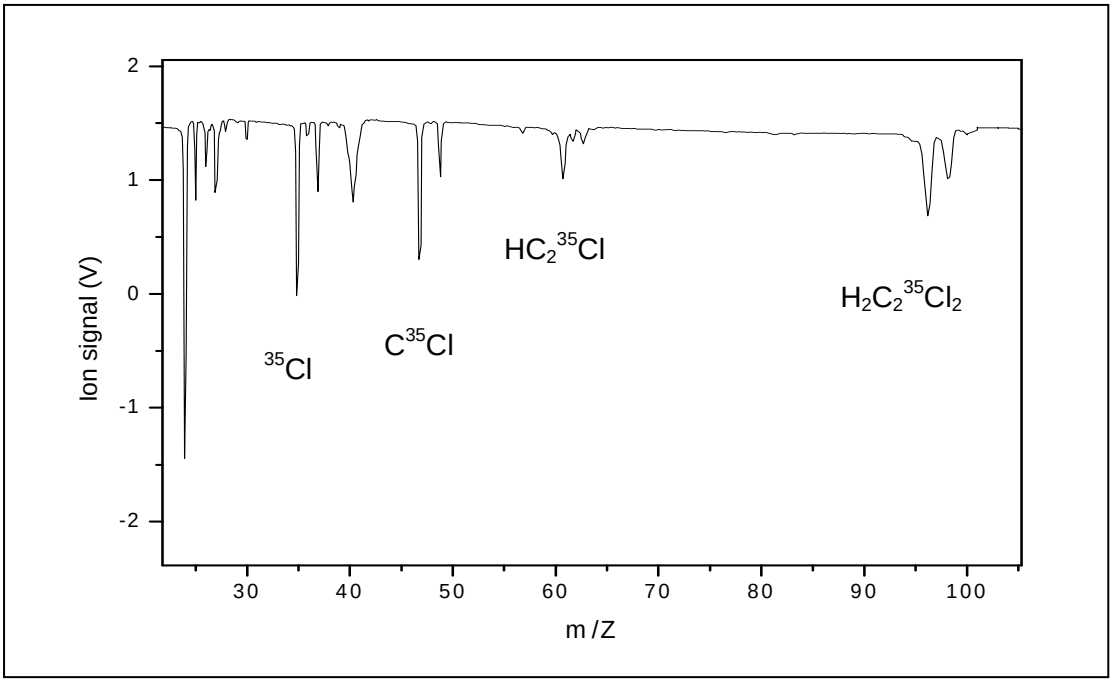

Figure 6.9: Time of flight mass spectrum of TCE using nanosecond laser ionization at 266 nm, 6 ns and 2.9 mJ pulses showing the selected peaks for optimization of TOF system

6.2.2.1. Defocusing position

Figure 6.10 shows the lens in front of the gas sample chamber. This lens was moved back and forth in order to find the best focusing position. When the lens is out of focus the degree of ionization decreases and therefore the mass peak sizes decrease. The graph in figure 6.11 shows the effect of defocusing on the ion signals for various molecular ions as indicated. The graph for the $^{35}Cl^{+}$ ion has an unexpected flat top profile. This was probably due to measurement errors, since the same trend was expected for all selected ion peaks. This result clearly shows where the optimal position of the lens is to maximise ionization and maximise mass peak signals. It also indicates that the focusing position is equally applicable for all

fragments and cannot be used to selectively enhance one peak (or ionization step) over another.

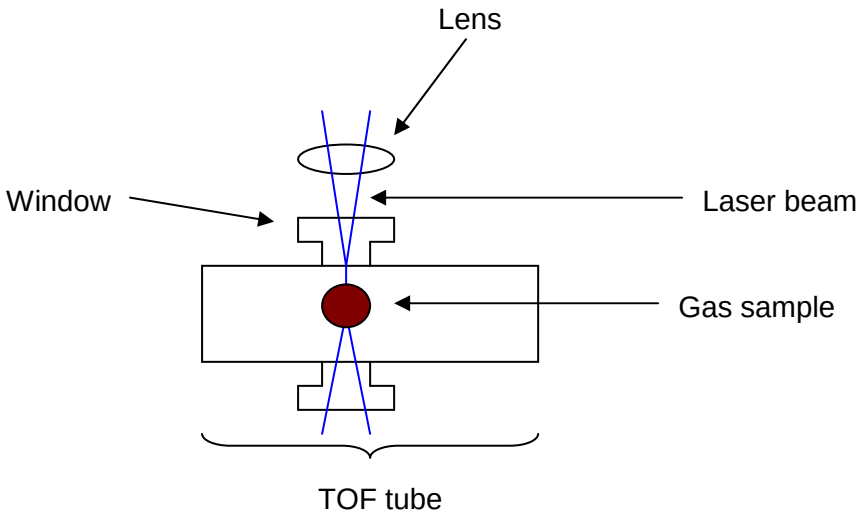

Figure 6.10: Focusing laser beam into gas sample chamber. The focus position is changed by moving the lens towards and away from the entrance window

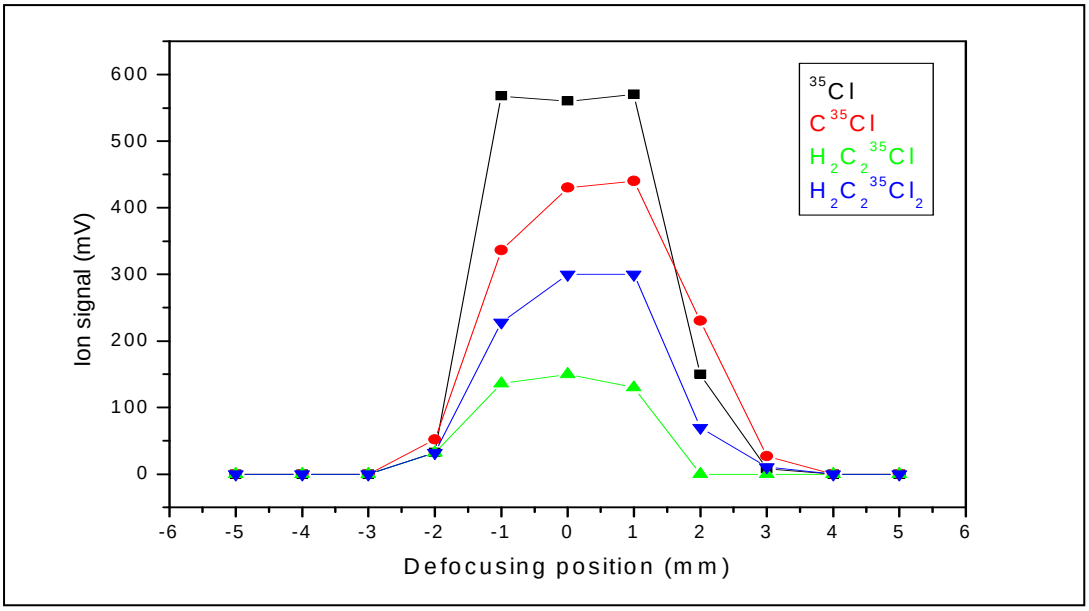

Figure 6.11: Graph showing the effect of defocusing of the lens on selected ion signals. This data is obtained by observing mass peak signals and varying the focus position with nanosecond laser pulses of 266 nm, 6 ns and 2.9 mJ

6.2.2.2. Delay scans

The degree of interaction between the gas and laser pulses was determined by the delay time between the gas pulse trigger and the laser trigger. Delay scans (delay between gas and laser pulses) were taken to determine the strength of selected ion signals at specific delay times. By taking delay scans from 100 to 1150 µs of different ion peaks, it was found that the peak signals in the mass spectra vary with delay times, as indicated in figure 6.12. The graph for the $^{35}Cl^+$ and $C^{35}Cl^+$ peak signals follow the same trend. The same applies for the $HC_2{}^{35}Cl^+$ and $H_2C_2{}^{35}Cl_2{}^+$ peak signals. These results indicate that the ionization of larger molecules occur in the range 220 to 850 *µ*s; thus a delay time of 350 µs was chosen for the mass spectrum of TCE taken at 266 nm to observe the larger molecules. The $^{35}Cl^+$ and $C^{35}Cl^+$ signal peaks start to appear at delay time of 110 µs and $HC_2{}^{35}Cl^+$ and $H_2C_2{}^{35}Cl_2{}^+$ peak signals starts to appear at delay time of 220 *µ*s. In this case we assume that the difference is mainly due to background gas in the vacuum chamber.

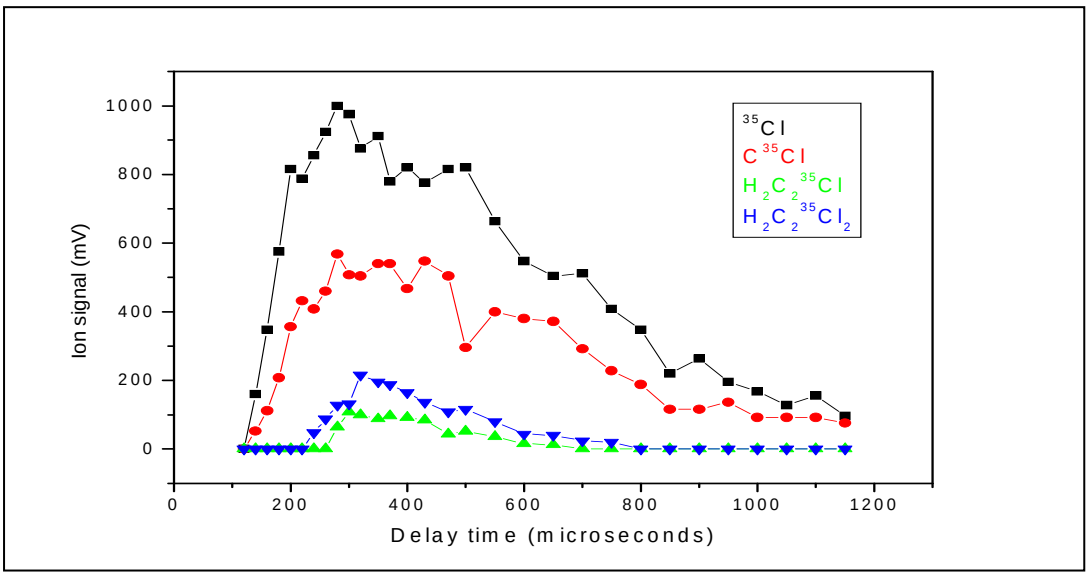

Figure 6.12: Delay scans of selected ion peaks at gas pulse duration of 190 µs with nanosecond laser at 266 nm, 6 ns and 2.9 mJ pulses. The optimal delay was found to be 350 µs

6.2.2.3. Laser energy

The selected mass spectra signals were observed as function of laser energy. The relationship between ion signals and laser energy could be found as shown in figure 6.13. This figure indicates saturation for the $^{35}Cl^+$ and $C^{35}Cl^+$ peak signals, while the signals obtained for $HC_2{}^{35}Cl^+$ and $H_2C_2{}^{35}Cl_2{}^+$ show that ionization of the large molecules increases sharply with laser energy above the value of approximately 1.4 mJ.

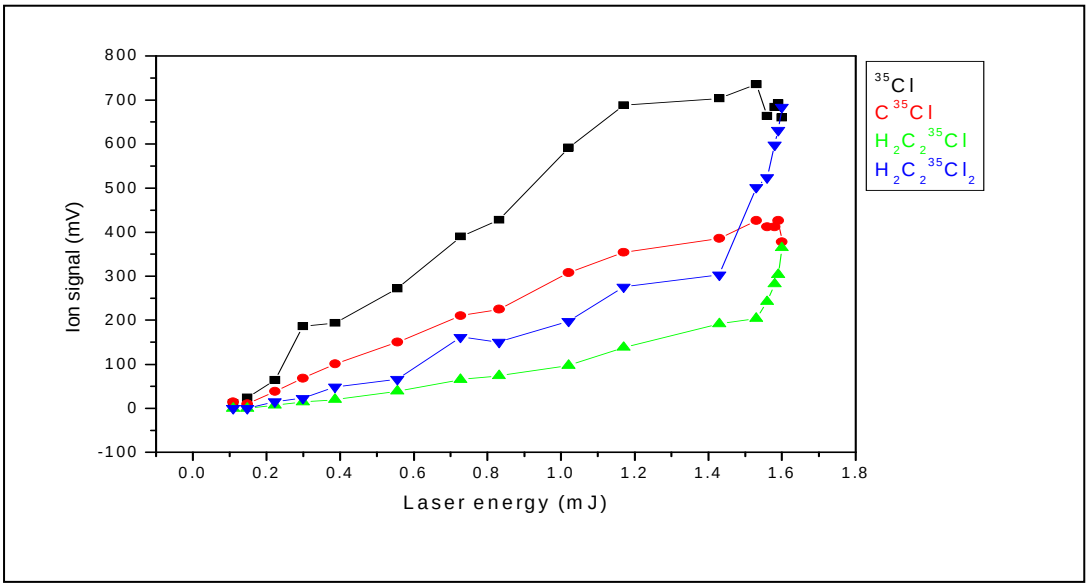

Figure 6.13: Ion signal versus laser energy at gas pulse duration of 190 µs and delay time of 350 µs with nanosecond laser at 266 nm, 6 ns pulses

6.2.2.4. Backing pressure (carrier gas pressure)

The backing pressure was varied to determine if it has an effect on the number of gas molecules in the ion source. The results in figure 6.14 shows a decrease in ion signal with an increase in backing pressure. An increase of the number of molecules with increasing backing pressure was expected. Therefore it can be observed that,

using no backing pressure, gives better signal; thus it is better not to use argon carrier gas at all under these experimental conditions.

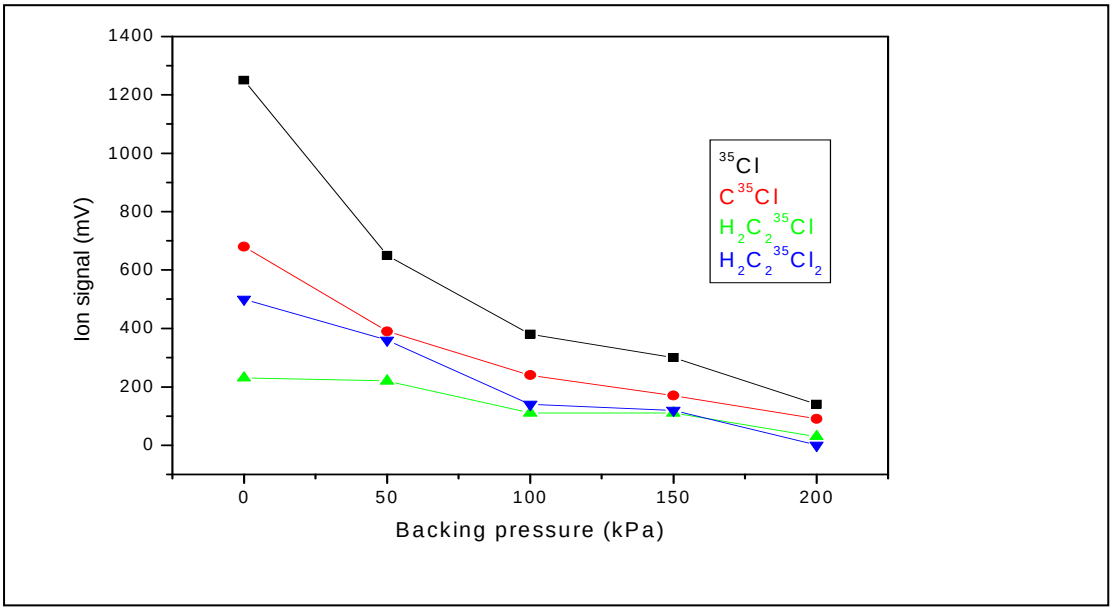

Figure 6.14: The relationship between selected ion signals and the backing pressure at conditions of 190 µs gas pulse duration and a delay time of 350 µs with nanosecond laser at 266 nm, 6 ns and 2.9 mJ pulses

6.2.3. TCE mass spectra obtained using the nanosecond and femtosecond laser systems

6.2.3.1. Nanosecond laser ionization mass spectra of TCE

The TOF mass spectra of TCE were obtained using nanosecond lasers at 212.5 nm, 266 nm and 425 nm wavelengths. The ion peaks observed are assigned and summarized in table 6.2. Pulse energies for 212.5 and 425 nm are 150 µJ and 4.4 mJ, respectively. The pulse energy obtained with 266 nm was 2.9 mJ. There were no peak signals observed for the wavelength of 425 nm with laser energy 4.4 mJ per

pulse. TCE was thus not ionized because of no absorption or resonant multi-photon ionization possible at this wavelength. The ion peaks obtained in both spectra shown in figure 6.15 (a) and (b) are comparable in the sense that all ion signals that are observed when using the dye laser, are present in the mass spectrum of TCE when using the Nd:YAG laser. However, there are larger molecular ions observed additionally with 266 nm which do not appear in the 212.5 nm spectrum. This was probably due to the considerably higher pulse energy used with the Nd:YAG laser. The reason why different delay times were used when measuring TCE mass spectra was already described in section 6.2.2.2. The larger molecular ions observed when using the Nd:YAG laser (and not visible in the dye laser mass spectrum) are $H_2C_2{}^{35}Cl^+$ (61 amu), $HC_2{}^{37}Cl^+$ (60 amu), $H_2C_2{}^{35}Cl_2{}^+$ (96 amu), and $C_2{}^{37}Cl_2{}^+$ (98 amu). The ion signals of singly ionized chlorine isotopes ($^{35}Cl^+$ and $^{37}Cl^+$ peak signals), together with singly ionized carbon and some singly ionized CH configurations (CH species from 13 to 32 amu), are clearly shown in the figure. The other products that formed with both the wavelengths of 212.5 and 266 nm are $CH_3{}^+$ (15 amu), $C^{35}Cl^+$ (47 amu) and $H^{35}Cl^+$ (36 amu).

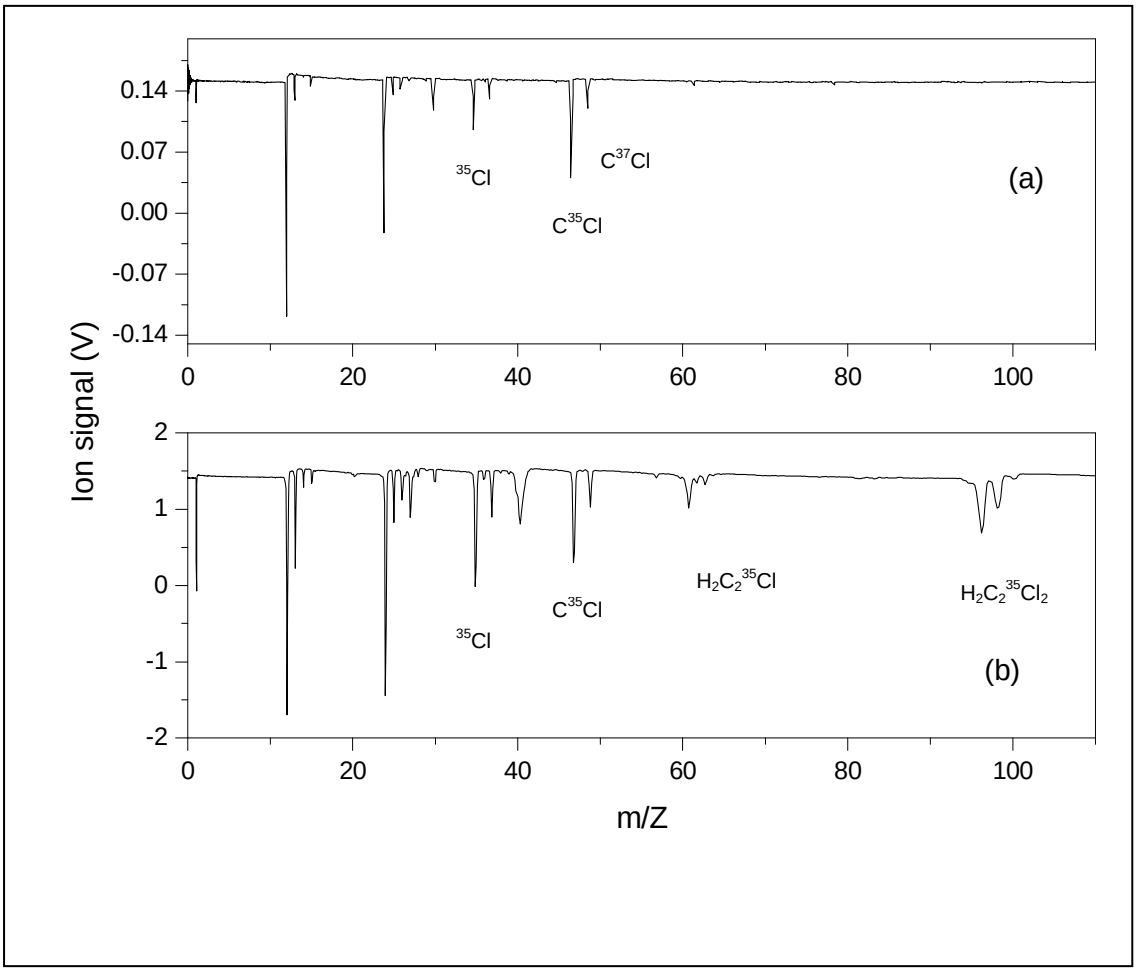

Figure 6.15: Laser photoionization mass spectra of TCE using nanosecond laser at (a) 212.5 nm, 6 ns and 150 µJ pulses, delay time of 150 *µ*s, and (b) 266 nm, 6 ns and 2.9 mJ pulses, delay time of 350 *µ*s

Table 6.2: Assignment of ionized fragments as in figure 6.15 for TCE (CH_3CCl_3)

Ions	Masses (amu)	Time of flight (μs)	
		Nd:YAG (266 nm)	Frequency-doubled Dye laser (212.5 nm)
H^+	1	4.85	4.75
C^+	12	16.4	16.3
CH_3^+	15	18.3	18.2
$^{35}Cl^+$	35	27.8	27.7
$H^{35}Cl^+$	36	28.3	28.3
$^{37}Cl^+$	37	28.6	28.5
Ar^+	40	29.9	-
$C^{35}Cl^+$	47	32.2	32.1
$C^{37}Cl^+$	49	32.9	32.8
$HC_2{}^{35}Cl^+$	60	36.6	36.5
$HC_2{}^{37}Cl^+$	62	37.4	-
$H_2C_2{}^{35}Cl_2^+$	96	46.2	-
$C_2{}^{37}Cl_2^+$	98	46.5	-
$H_2C_2{}^{37}Cl_2^+$	100	47.2	-

Possible products that can be formed during dissociation of TCE using nanosecond laser pulses are as follows:

$$CH_3CCl_3 + nh\nu \longrightarrow C_2 + 3HCl$$

$$CH_3CCl_3 + nh\nu \longrightarrow HC_2Cl + 2HCl$$

$$CH_3CCl_3 + nh\nu \longrightarrow CH_2CCl_2 + HCl$$

$$CH_3CCl_3 + nh\nu \longrightarrow H_3C_2Cl_2 + CCl$$

These dissociation pathways were speculated due to the ion signals observed in the mass spectra of TCE. Some of the reactions are similar to the reactions that were discussed in section 4.3. The strongest peak in both mass spectra is the C^+ ion, and this is followed by the C_2^+ ion. The reason why the $H_2C_2Cl_2$ ion signal was observed instead of the parent ion $H_3C_2Cl_3$, when using nanosecond laser pulses, was probably due to the immediate dissociation of the parent ion into $H_2C_2Cl_2$ and HCl.

It is clear from the expanded view of the TCE mass spectra for high mass fragments (figure 6.16) that the mass spectrum obtained with the Nd:YAG laser gives stronger signals than the mass spectrum obtained with the dye laser. This is mainly due to the difference in pulse energy used. The pulse energy for the dye laser was much less, thus less ionization took place. There is an ion signal at 78 amu when using the dye laser, which was not obtained when using the Nd:YAG laser. This ion peak corresponds to the benzene molecule which is a contaminant from the pumps used in the TOF-MS system. It is only observed when using the dye laser due to benzene having very strong absorption at 212.5 nm. The small temporal shift in peaks in the spectra (much less than 1 amu) was due to different settings used for triggering on the oscilloscope.

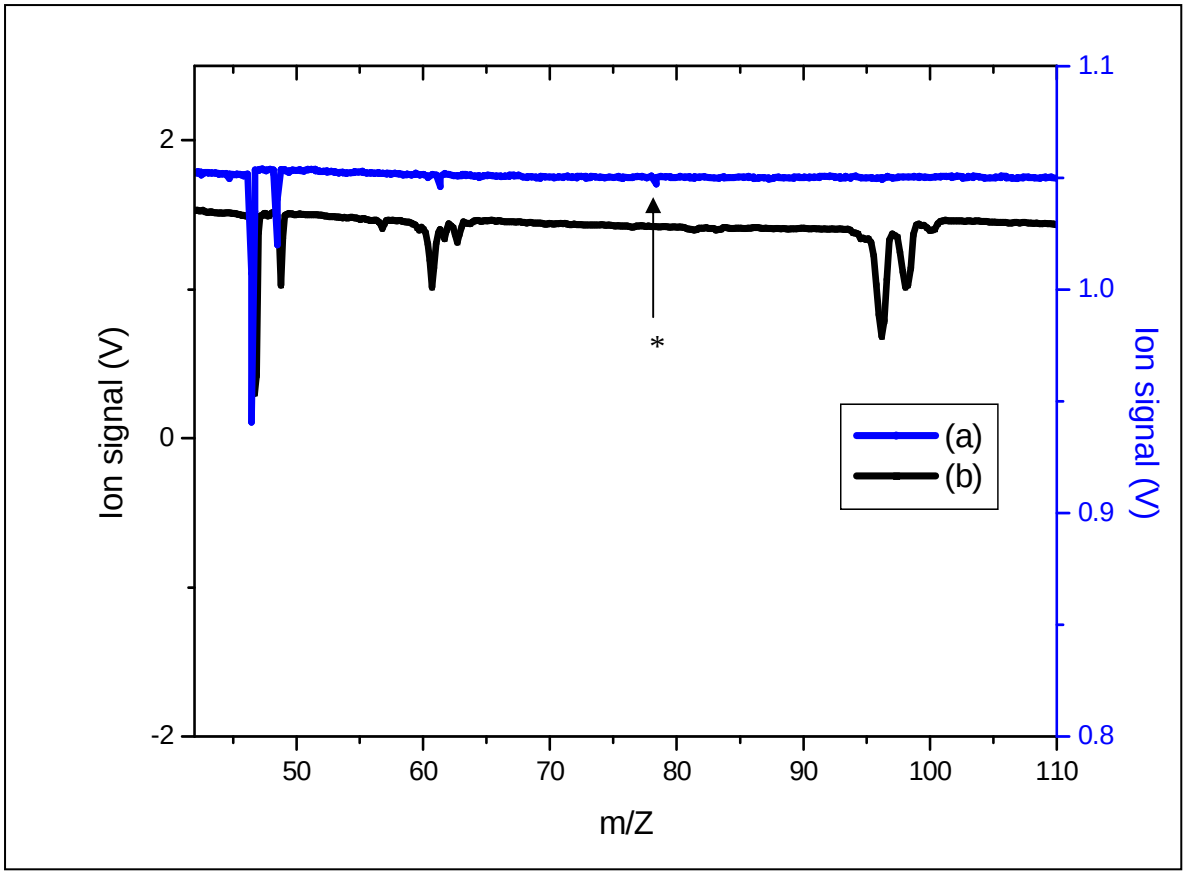

Figure 6.16: Expanded view of high mass fragments present in the TCE time of flight mass spectra between 40 and 110 amu with nanosecond laser (a) 212.5 nm, 6 ns, 150 µJ and (b) 266 nm, 6 ns and 2.9 mJ pulses. Benzene = *

6.2.3.2. Femtosecond laser ionization mass spectra of TCE

Figure 6.17 shows the mass spectrum of TCE taken at 795 nm, 120 fs and 1 mJ laser pulses. The observed ion peaks are summarised in table 6.3. The spectrum shows the ion signals of the products formed during ionization and dissociation of CH_3CCl_3, including the methyl ion CH_3^+ (15 amu), the hydrogen chloride ions $H^{35}Cl^+$ (36 amu) and $H^{37}Cl^+$ (38 amu), the carbon trichloride ions $C^{35}Cl_3^+$ (117 amu) and $C^{37}Cl_3^+$ (123 amu), and the dichloroethene ions $H_2C_2{}^{35}Cl_2^+$ (96 amu), $H_2C_2{}^{37}Cl_2^+$ (100 amu) and $H_3C_2{}^{35}Cl_2^+$ (97 amu). The overshoot in the mass spectrum directly after the

strong mass peaks is due to electronic mismatch of impedances in the amplifier system. The C-H combinations are observed in the figure from 13 to 32 amu. The parent ion was not observed.

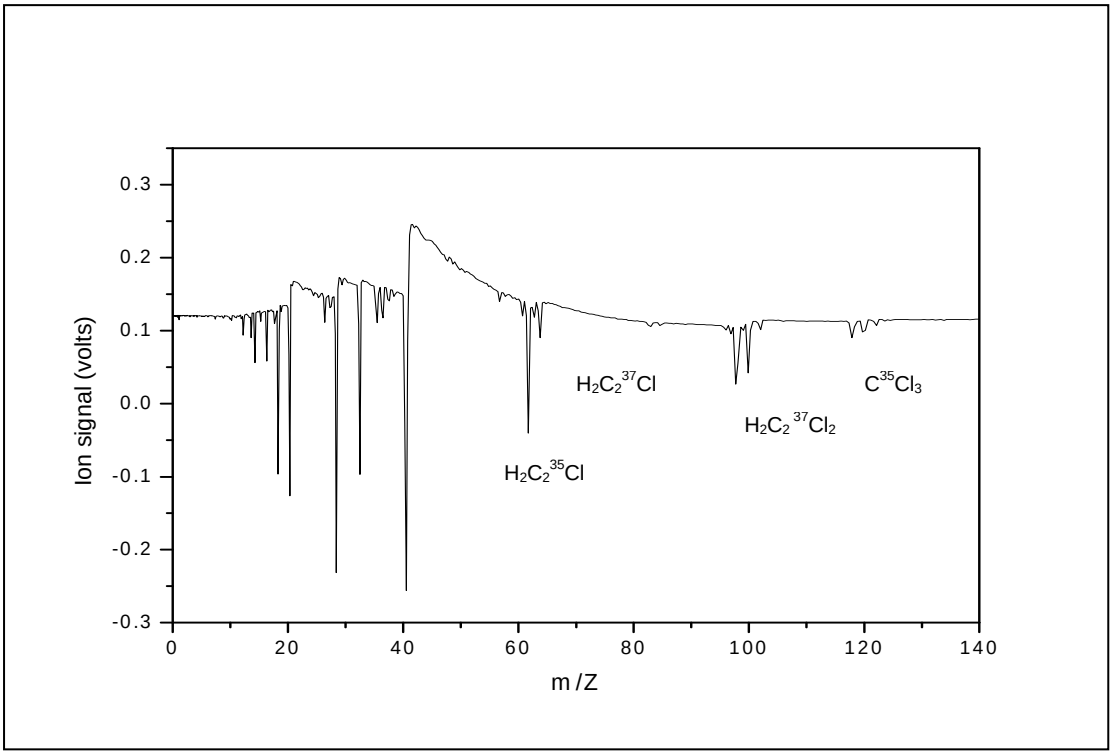

Figure 6.17: Laser photoionization time of flight mass spectrum of TCE using the femtosecond laser with 795 nm, 120 fs, 1 mJ pulses

The possible products formed during dissociation of TCE with femtosecond laser pulses are:

$$CH_3CCl_3 + nh\nu \longrightarrow CH_3 + CCl_3$$

$$CH_3CCl_3 + nh\nu \longrightarrow HC_2Cl + 2HCl$$

$$CH_3CCl_3 + nh\nu \longrightarrow CH_2CCl_2 + HCl$$

$$CH_3CCl_3 + nh\nu \longrightarrow H_3C_2Cl_2 + Cl$$

$$CH_3CCl_3 + nh\nu \longrightarrow H_2CCl_3 + CH$$

Table 6.3: Assignment of ion signals as in figure 6.17 of the mass spectrum of TCE

Time (μs)	Masses (amu)	Ion peaks
4.8	1	H^+
16.2	12	C^+
18.1	15	CH_3^+
20.9	20	Ar^{++}
27.6	35	$^{35}Cl^+$
28	37	$H^{37}Cl^+$
28.8	39	$H^{37}Cl^+$
29.5	40	Ar^+
36.1	60	$HC_2{}^{35}Cl^+$
36.4	62	$HC_2{}^{37}Cl^+$
36.7	63	$H_2C_2{}^{37}Cl^+$
37	64	$H_3C_2{}^{37}Cl^+$
45.4	96	$H_2C_2{}^{35}Cl_2{}^+$
45.8	97	$H_3C_2{}^{35}Cl_2{}^+$
46.8	100	$H_2C_2{}^{37}Cl_2{}^+$
50.3	117	$C^{35}Cl_3{}^+$
50.8	119	$H_2C^{35}Cl_3{}^+$
51.2	123	$C^{37}Cl_3{}^+$

The intensity of the laser was varied to see if the parent molecular ion could possibly be observed (see figure 6.18 and 6.19). Ion peak intensities in general appeared stronger with the laser energy ranging from 0.964 to 0.378 mJ (high intensity) and weaker when the laser energy was low (0.273 and 0.0813 mJ). It was also observed that the ion signals start to appear when the intensity is at 0.015 mJ, which seems to be the threshold for ionization in this experimental setup. The Ar^+ and larger molecule ion peaks appear broad at high laser energy. This broadening might be due to a very large amount of ionization, resulting in a large cloud of ions in the ionization region with ions travelling at different kinetic energies and therefore reaching the detector at different times. This could be enhanced further by collision ionization of argon ions colliding with TCE molecules and fragments. The same ion peaks appear narrow at lower laser energy. Thus, good resolution of the spectrum can be obtained by

lowering the laser intensity and under such experimental conditions sharp peaks will be observed. It can be observed from the figure that the Ar^+, $H_2C^{35}Cl_2^+$ and $HC_2^{35}Cl^+$ peaks are sharp with decreasing laser energy and the peak intensity also decreases.

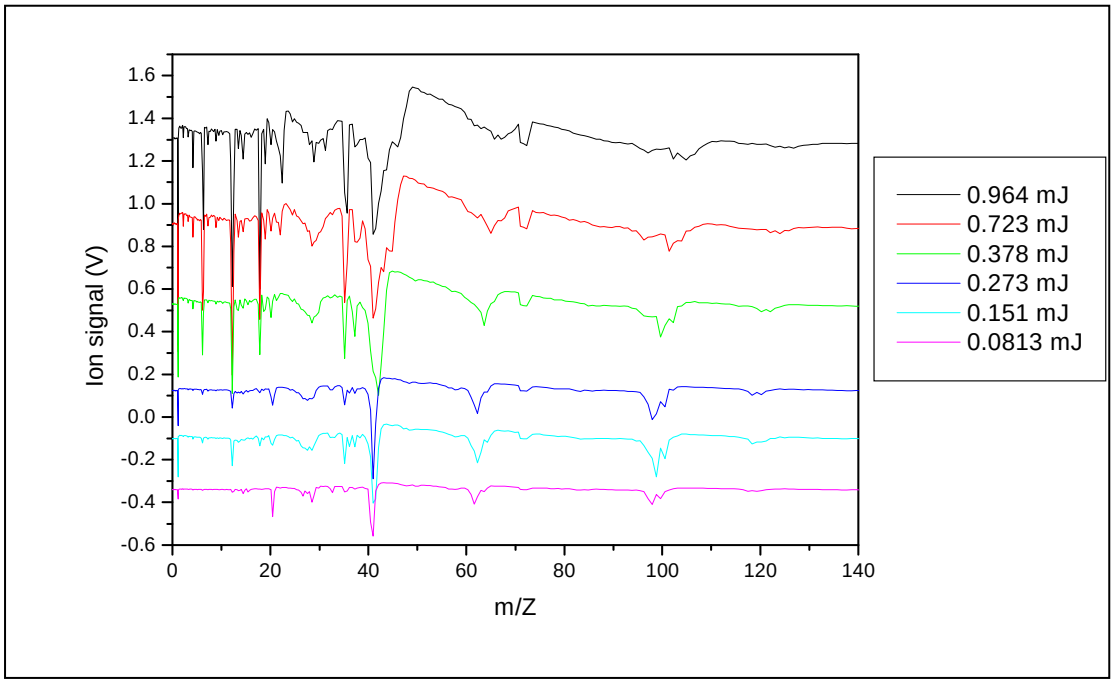

Figure 6.18: Laser photoionization time of flight mass spectra of TCE using femtosecond laser pulses at 795 nm with different laser energies

Figure 6.19 shows that the peak intensity increases with an increase in laser energy at 397.5 nm. The peaks in the range 60-65 amu are broad when the laser energy is 0.155 mJ and it is resolved when the laser energy is 0.128 mJ. The broadening of the peaks, as explained above, was due to the laser energy. If the laser energy is high, the ion peak becomes broad, and if the laser energy is low, the ion peak is resolved. It can then be concluded from these results that, in this experimental setup, the peak resolution improves with decrease in laser energy and the peak intensity decreases with decrease in laser energy.

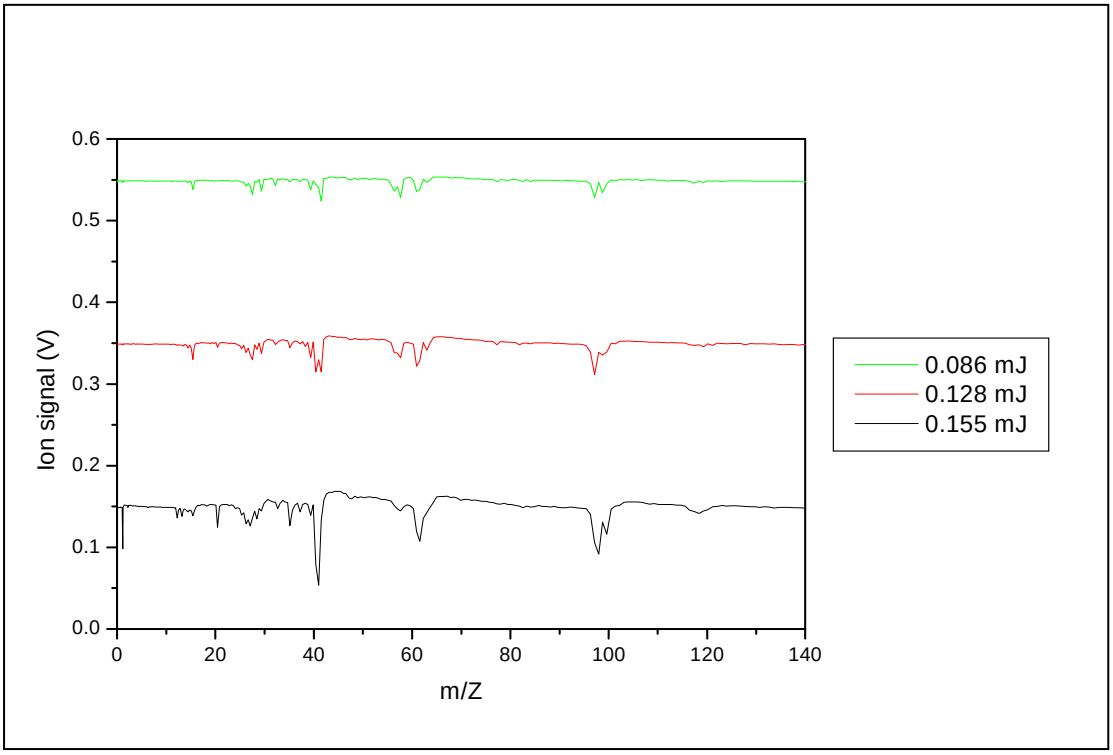

Figure 6.19: Laser photoionization time of flight mass spectra of TCE with femtosecond laser pulses at 397.5 nm and different laser energy

TCE was excited with 795 nm and 397.5 nm wavelengths with the same energy to observe if the femtosecond laser ionization of TCE is dependent on wavelength or not. The peak intensities of the mass spectrum taken at 795 nm are higher than the one taken at 395.7 nm by a factor of two to three. The small shift in peaks in figure 6.20 was due to the different settings used for triggering on the oscilloscope. There are peaks in the 795 nm mass spectrum that do not appear in the spectrum obtained using femtosecond laser pulse at 397.5 nm. These peaks are for C^{++} (6 amu) and CH_6^+ (18 amu). This might be due to the slightly different focusing used. A number of mechanisms can be active and contribute towards the observed mass spectra of TCE for the femtosecond ionization. The spectra in figure 6.20 confirm that there is not a considerable wavelength dependent ionization using the femtosecond laser system because the spectra are similar (and a shorter wavelength would be expected to cause more ionization due to the higher photon energies).

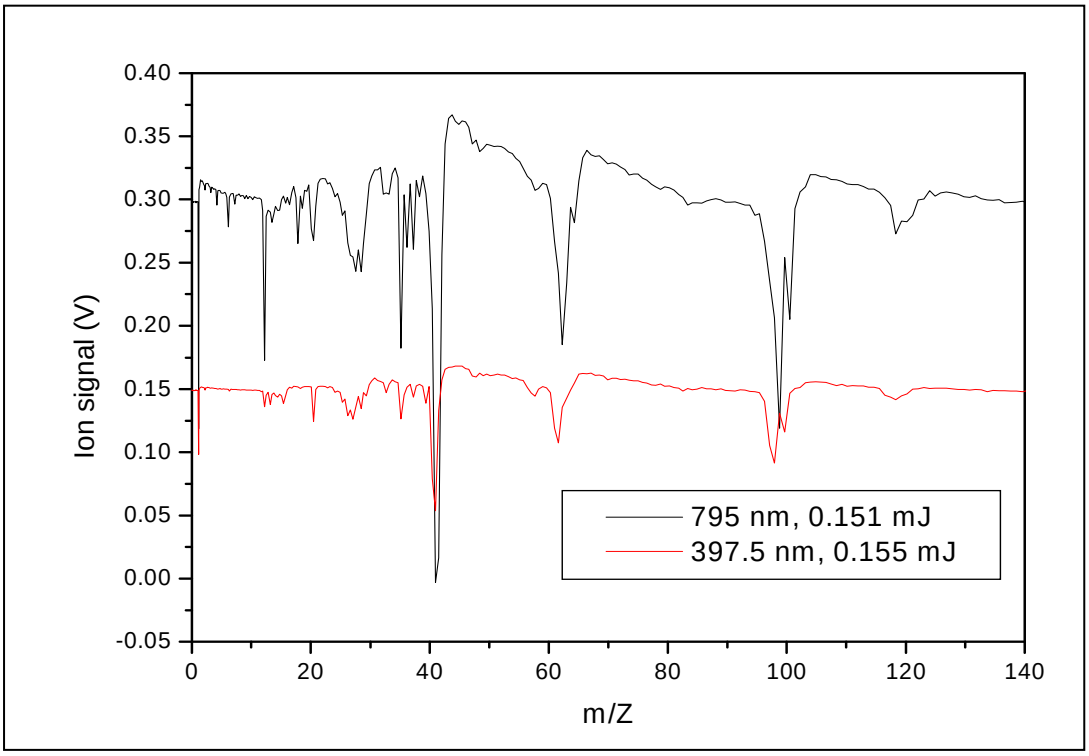

Figure 6.20: Laser photoionization time of flight mass spectra of TCE with femtosecond laser at 795 nm, 0.151 mJ and 397.5 nm, 0.155 mJ pulses

6.2.4. Comparison of TCE mass spectra obtained using nanosecond and femtosecond laser systems

Figure 6.21 was recorded to observe the differences in mass spectra of TCE when using nanosecond and femtosecond laser pulses. The figure shows that total ionization signals from TCE are stronger when using a nanosecond laser, with weaker peak signals for the femtosecond laser. It can also be observed that there is no parent ion when using both nanosecond and femtosecond laser systems. This means that TCE dissociates or ionises easily with both laser systems. The Ar^+ peak (at 40 amu) is present in both spectra because argon was used as a carrier gas. The broadening and the overshoot on argon peak are almost the same size in both mass spectra and this can be observed when the same scale is used for both. It was

observed that the TCE mass spectrum taken with nanosecond laser pulse at 266 nm lacks the carbon trichloride and other dichloroethene ion signals.

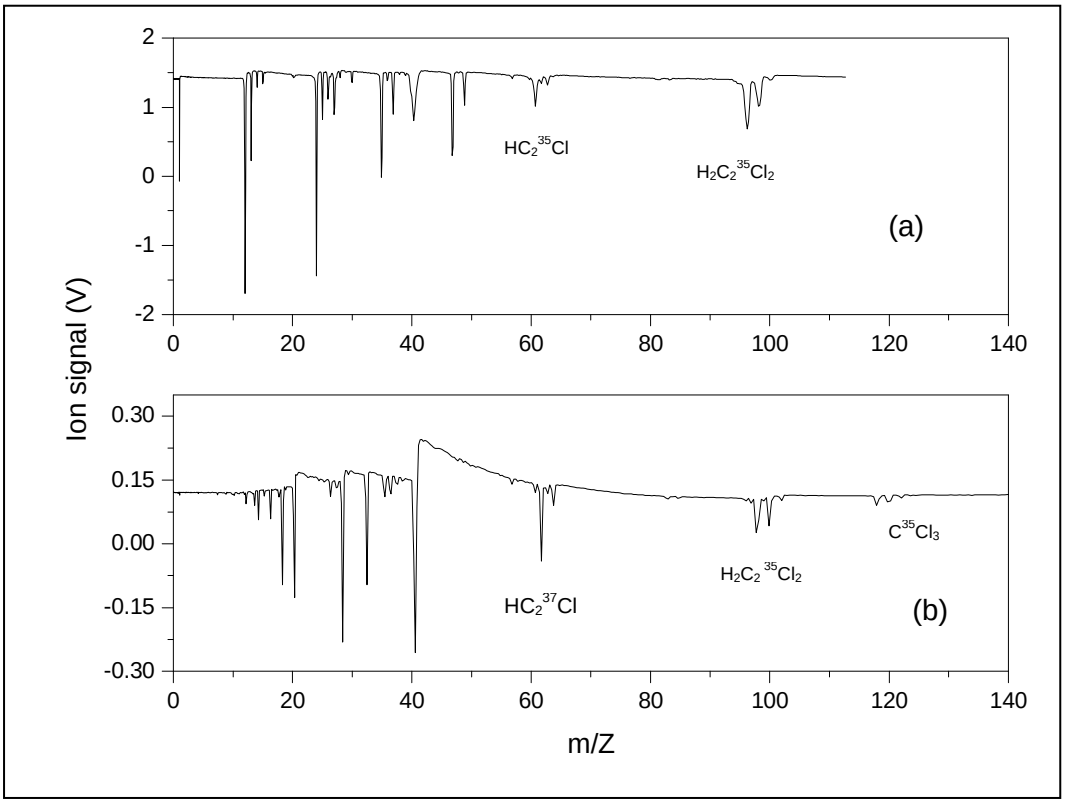

Figure 6.21: Laser photoionization mass spectra of TCE (a) using nanosecond laser at 266 nm, 6 ns, 2.9 mJ pulses, and (b) using femtosecond laser at 795 nm, 120 fs and 1 mJ pulses

Results from an ultraviolet spectrometer, as mentioned in section 5.2.3, indicate that TCE absorbs strongly in the deep ultraviolet and vacuum ultraviolet region with peak absorption at 180 nm. This information helped us in determining the wavelengths needed to excite TCE. It was mentioned that the carbon chlorine bond is one of the absorbing species. Excitation of this bond results in dissociation for the TCE molecule. Therefore the nanosecond and femtosecond laser ionization at non-resonant wavelengths 266 and 795 nm might have proceeded through an

intermediate state, which includes the activation of the C-Cl bond. The CCl_3 acts as a chromophore (as defined in section 5.2.3) for photon absorption. These account for the presence of the $C_2H_2Cl_2^+$ signals in both mass spectra. However, for the femtosecond laser ionization, a number of mechanisms might have been active and contribute to the observation of TCE mass spectra. The two dominant mechanisms that are used to explain multi-photon ionization of molecules were discussed in section 4.4. Based on how the mechanisms were explained, it is then believed that the mechanism that contributed towards observation of the mass spectra of TCE using femtosecond laser pulses, is ionization followed by dissociation, or ladder climbing, due to the pulse length being shorter than the lifetime of any intermediate states. The ladder climbing mechanism dominates at extremely short pulse lengths.

The strong absorption of TCE in the ultraviolet region was also confirmed by using the TOF-MS in conjunction with lasers in the deep UV region. The theoretical ionization energy of TCE is 11 eV [Rae systems, 1993]. This information helped in determining how many photons are required for the multi-photon ionization of TCE to take place. From the ionization energy of 11 eV, one photon can be absorbed at a wavelength of 112 nm. Alternatively, two photons can be absorbed at a wavelength of 224 nm. With a wavelength of 266 nm, three or more photons need to be absorbed in order to reach the ionization level, while with a wavelength of 212.5 nm, only two or more photons need to be absorbed. The number of photons needed to ionize TCE at 795 nm is seven, the photon energy of each photon being only 1.56 eV.

6.2.5. Comparison of TCE and MTS mass spectra using nanosecond and femtosecond laser pulses

It was mentioned in section 1.1 that TCE and MTS have a similar structure. Therefore time of flight mass spectra of both molecules were compared in order to observe if they behave in a similar manner when irradiated with laser photons. The mass spectra of TCE and MTS recorded in figure 6.22 and 6.24 are similar. The overshoot next to the strongest peak in figure 6.22 was observed in both spectra. The peak intensities of Cl^{+}, Ar^{++}, and Ar^{+} ions are relatively similar. The larger peaks for the MTS will not appear at the same time as TCE as they do not have the same masses. The parent ion was observed in the MTS mass spectrum, but not in the TCE mass spectra.

Figure 6.23 shows the expanded view of low mass fragments region of TCE and MTS. The broadening of peaks can be observed clearly. This broadening is believed to be due to the sample having too high density in the ionization region. Thus the sample needs to be diluted in order to get sharper ion peaks.

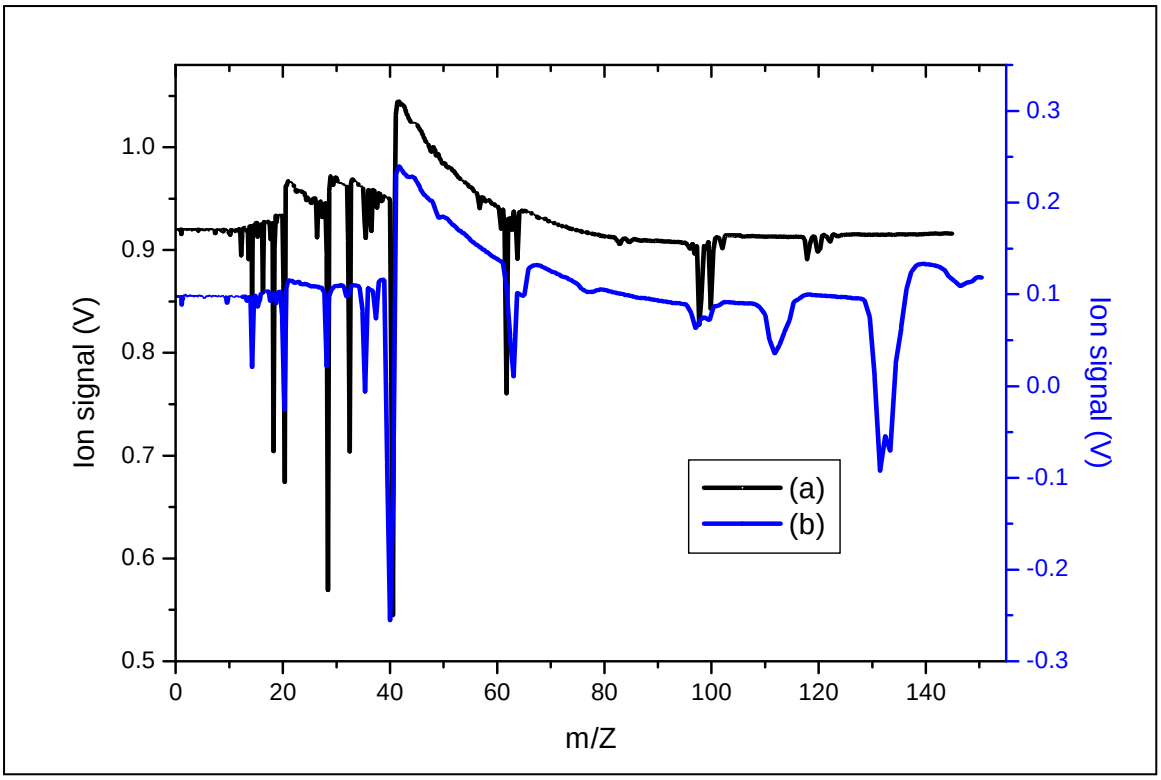

Figure 6.22: Laser photoionization mass spectra of (a) TCE and (b) MTS using femtosecond laser at 795 nm, 120 fs, and 1 mJ pulses

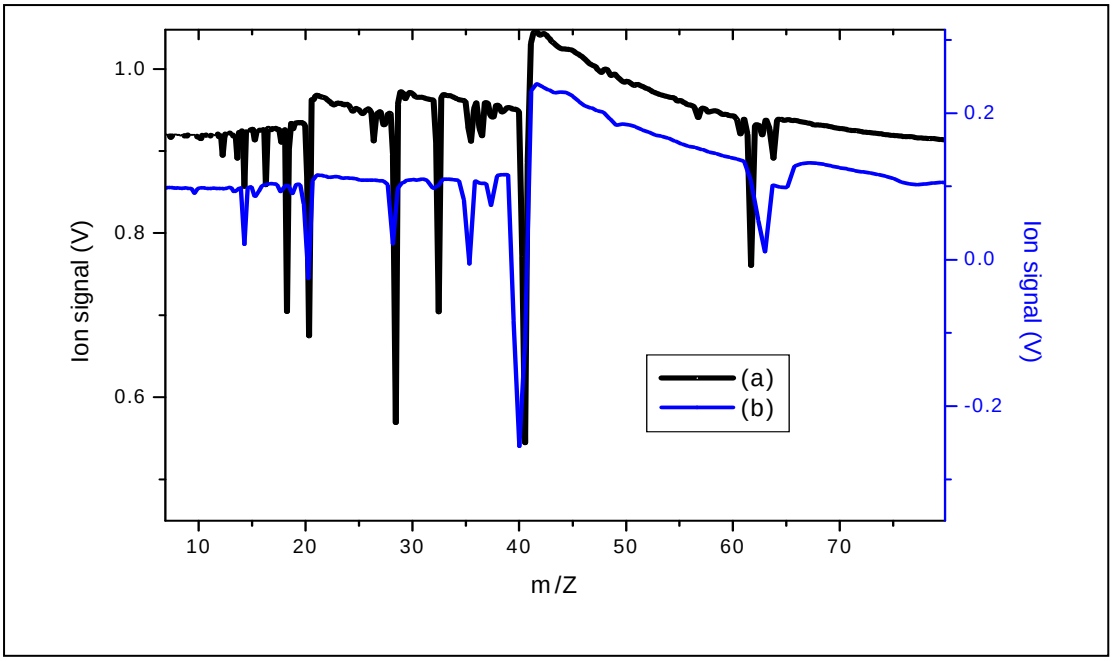

Figure 6.23: Expanded laser photoionization mass spectra of (a) TCE and (b) MTS using femtosecond laser at 795 nm, 120 fs, and 1 mJ pulses

Figure 6.24 shows mass spectra of TCE and MTS taken at room temperature with 266 nm, 6 ns and 2.9 mJ laser pulses, while figure 6.25 shows the expanded view of low mass region. There is no parent ion observed in both mass spectra. The fragmentation of the molecule is almost equal. Thus there is more fragmentation for both TCE and MTS when using nanosecond laser pulses. The mass spectra produced equivalent peak signals of chlorine ions. There is no argon peak observed in the MTS spectrum because argon was not used when taking these measurements.

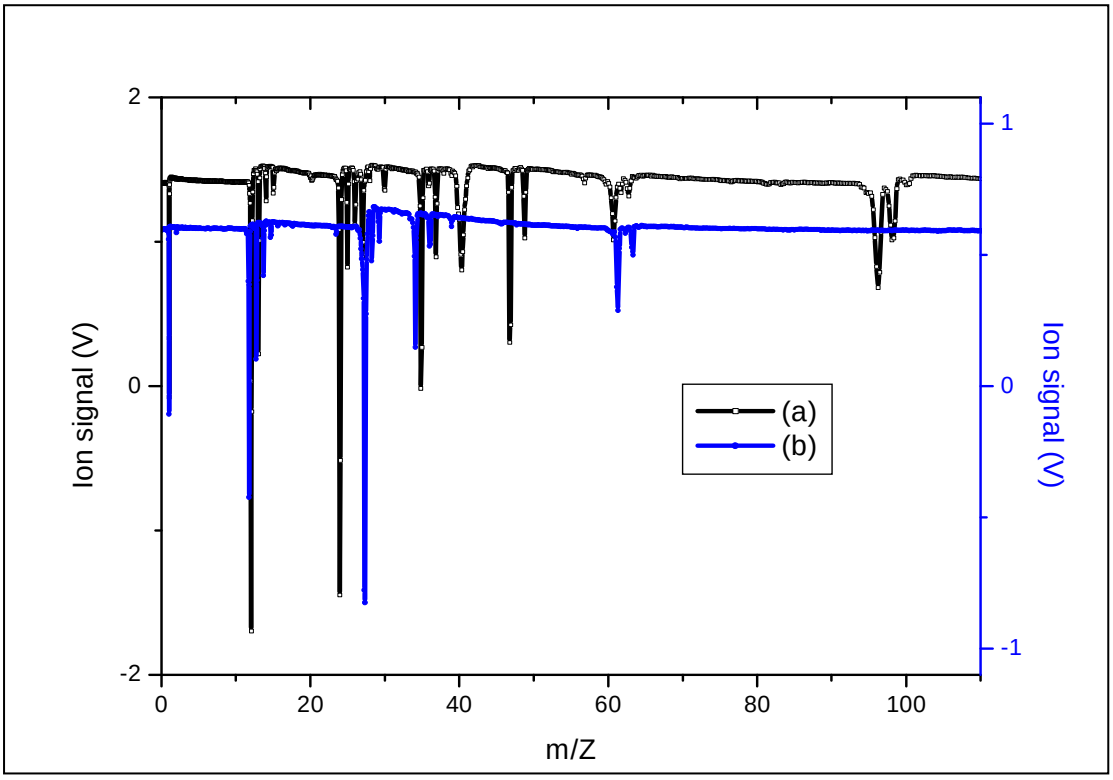

Figure 6.24: Laser photoionization mass spectra of (a) TCE and (b) MTS using nanosecond laser at 266 nm, 6 ns, and 2.9 mJ pulses

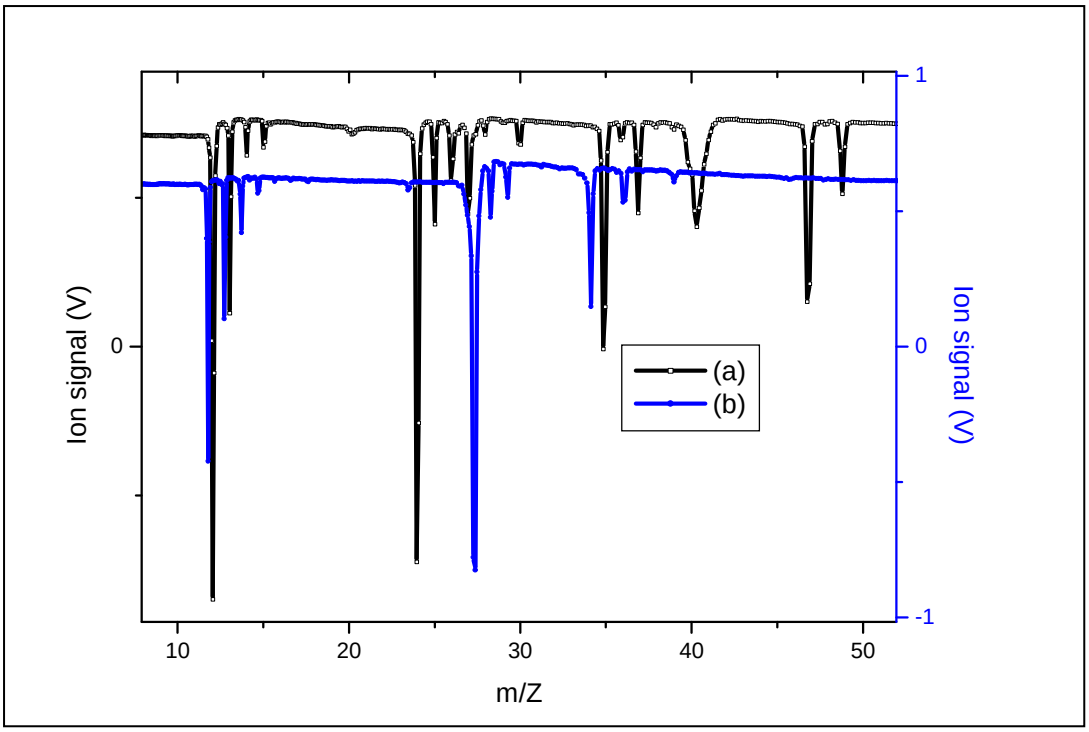

Figure 6.25: Expanded laser photoionization mass spectra of (a) TCE and (b) MTS using nanosecond laser at 266 nm, 6 ns, and 2.9 mJ pulses

It can be concluded from the comparative spectra using nanosecond and femtosecond laser pulses that the mass spectra of TCE and MTS are qualitatively similar. Ledingham and Singhal [1997] reported that the mechanisms that dominated during multi-photon ionization molecules are ladder switching and ladder climbing. This was confirmed by obtaining mass spectra of different molecules using femtosecond and nanosecond laser pulses. Similar results were found in the current study and the mass spectra of TCE and MTS reveals similarities which were previously documented. Thus it can be concluded that the mechanism that was dominant during multi-photon ionization of TCE and MTS using nanosecond laser pulses, was ladder switching, while the ladder climbing mechanism was dominant in the femtosecond regime.

Chapter 7

Conclusions

7.1. Conclusion

The molecular properties of TCE were investigated by calculating the structural parameters, dipole moment and infrared spectrum of TCE. Ab initio calculations showed that TCE belongs to the symmetry group, C_{3v}, and has a net dipole moment, stretching (symmetry and asymmetry) and bending (rocking) vibrations. Vibrational types, which were predicted for TCE by Herzberg [1945], were confirmed by using Spartan. The calculated, experimental and documented fundamental frequencies of TCE, of which all are active in the infrared region except the torsional vibration around the C-C axis, were compared to one another. These were in reasonable agreement with each other. The experimental FT-Raman spectrum of liquid TCE also confirmed the documented vibrational frequencies. The products formed during dissociation or decomposition of TCE were calculated with Spartan and obtained using femtosecond and nanosecond laser ionization. The recorded UV-Vis spectrum of TCE helped in determining the wavelength needed to excite TCE for ionization and dissociation processes. It also confirmed that TCE absorbs strongly in the UV region.

TOF mass spectra of TCE resulting from ionization and dissociation with nanosecond and femtosecond laser pulses were obtained experimentally. In nanosecond and femtosecond cases, many fragment ions are observed. In the femtosecond ionization experiment, using 795 nm, 120 fs and 1 mJ pulses, more larger fragments are observed compared to the nanosecond case. However, the parent molecular ion was

not observed in either case. The chlorine ions ($^{35}Cl^+$ and $^{37}Cl^+$) ratio when using nanosecond and femtosecond laser pulses are 4:1 and 2:1. The ratio for the larger fragment HC_2Cl isotopes when using both laser pulses is 1:2. The other larger fragment, $H_2C_2Cl_2$ isotopes ratio is 1:1 when using both laser pulses. According to Ledingham and Singhal [1997], multi-photon ionization can take place via two mechanisms – ladder climbing and ladder switching. Ladder switching is when a molecule is dissociated and then individual fragments are ionized by multi-photon ionization. Ladder climbing is when a molecule is ionized in its entirety and then the parent molecular ion fragments after ionization to produce both ions and neutrals. In the nanosecond regime, ladder switching is dominant, while in the femtosecond regime ladder climbing is dominant, according to Ledingham and Singhal [1997]. Our results confirm this in the sense that larger fragments are observed in the femtosecond case, and the mass spectrum is exactly the same for the 795 and 397.5 nm cases. This was confirmed by the presence of the CCl_3^+ ion peak that was observed when using femtosecond laser pulses. In the nanosecond case, strong wavelength dependence is observed, which is representative of ladder switching, as well as the observation of smaller fragment ions. No ion signals were observed when using the dye laser at a wavelength of 425 nm, or the Nd:YAG laser at 532 nm. For the femtosecond experiments, ionization seems to happen regardless of the laser wavelength (non-resonant). There was significant ionization with the 795 nm wavelength even though TCE does not absorb light in the visible or near IR region of the electromagnetic spectrum as confirmed by the UV-Vis spectrum reported in section 5.2.3.

In summary, the process that took place during the laser photoionization of TCE using femtosecond and nanosecond laser pulses was a non-resonant multi-photon ionization process. The multiphoton ionization of TCE leads to fragmentation by two

mechanisms, as described above. It was demonstrated that the numbers of different fragment ions can be increased or decreased using different laser parameters.

7.2. Future work

More studies may be conducted in attempts to control dissociation and ionization processes using a technique called femtosecond laser pulse coherent control. This technique will allow us to control ionization and dissociation products by changing laser parameters only. This can be used to optimise industrial processes and a laboratory demonstration of this will be of great value for the SiC coating process for example. This is because coherent control, although feasible technique that has been demonstrated before, has not yet been demonstrated before for any industrially relevant process such as this.

References

Anonymous (ANON), How the PBMR fuel works, Pebble Bed Modular Reactor (PBMR), 1999, http://www.pbmr.com/index.asp?Content=224, Date of access: 18 September 2008.

Atkins, P. and De Paulo, J., Physical Chemistry, , 2000, Oxford, 7th Edition, 453 – 468.

Australian Laser Manufacturer, MCE lasers, 2006, How does a laser work, MonoChromatic Engineering Pty Ltd, available online at http://www.mcelasers.com.au/lasers.php, Date of access: 15 July 2008.

Barton, D. H. R., and Onyon, P. F., The pyrolysis of 1,1,1-trichloroethane, *J. Chem. Soc*., 1950, **72**, 988-995.

Besmann, T. M., Sheldon, B. W., Moss, T. S., III, Kaster, M. D., Depletion effects of silicon carbide deposition from methyltrichlorosilane, *J. Am.Ceram.Soc*., 1992, **75**, 2899-2903.

Butler, J., STR Analysis by time of flight mass spectrometry, *Profiles in DNA*, 1999, 3-6.

Carley, R. E., Heesel, E., Fielding, H. H., Femtosecond lasers in gas phase chemistry, *Chem. Soc. Rev*., 2005, **34**, 949-969.

CIESIN, Ozone depletion processes, Columbia University, CIESIN thematic guides, 1997, http://www.ciesin.columbia.edu/TG/OZ/ozndplt.html. Date of access: 18 September 2008.

Codling, K., Frasinski, L. J., Dissociative ionization of small molecules in intense laser fields, *J. Phys. B: At. Mol. Opt. Phys*., 1993, **26**, 783-809.

Cotter, R. J., Time of flight mass spectrometry: instrumentation and applications in biological research, *Am. Chem. Soc.,* 1997, 19-44.

Dantus, M., and Lozovoy, V., Experimental coherent control of physicochemical processes, *Chem. Rev.*, 2004, **104**, 1813-1859.

Dobson, S., Jensen, A. A., Gilbert, M., 1990, 1,1,1-Trichloethane, world Health Organisation Geneva, http://www.inchem.org/documents/ehc/ehc/ehc136.htm. Date of access: 16 April 2007.

Durig, J. R., Craven, K. K., and Bragin, J. J., Low-frequency vibrations of molecular solids X CH_3CCl_3, CD_3CCl_3, CH_3CCl_2H, and CH_3CF_3, *J. Chem. Phys*., 1971, **54**, 479-487.

Ecelberger, S. A., Cornish, T. J., Collins, B. F., Lewis, D. L., and Bryden, W. A., Suitcase TOF: A Man-Portable Time-of-Flight Mass Spectrometer, *Johns Hopkins Apl. Technical Digest*, 2004, **25 (1)**, 14-19.

El-Sabban, M. Z., Meister, A. G., and Geveland, F. F., Substituted ethanes. III. Raman and Infrared spectra, assignments, force constants, and calculated thermodynamic properties for 1,1,1-trichloroethane, *J. Chem. Phys*., 1951, **19**, 855-59.

Evans, J. C., and Bernstein, H. J., Intensity in the Raman effect: IV. Raman intensity sum rules and frequency assignments for CH_3CN, CD_3CN, CH_3CCl_3 and CD_3CCl_3, *Can. J. Chem*., 1955, **33**, 1746-1755.

Frankiss, S.G., and Harrison, D. J., Thermodynamic properties of aliphatic halogen compounds. III. Vibrational spectra and thermodynamic functions of 1,1,1,-trichloroethane, *Spectrochimica Acta*, 1975, **31A**, 29-39.

Gerkens R.R., Franklin J.A., The rate of degradation of 1,1,1-trichloroethane in water by hydrolysis and dehydrochlorination, *Chemosphere*, 1989, **19**, 1919-1937.

Ghosh,S. N., Trambarulo, R., and Gordy, W., Microwave spectra and molecular structures of fluoroform, chloroform and methylchloroform, *J. Chem. Phys*., 1952, **20**, 605-607.

Gorjan, M., Femtoscience Seminar, University of Ljubljana, Faculty of Mathematics and Physics, Department of Physics, 2006, 1-16.

Gu, C. H., Li, H., Gandhi, R. B., and Raghavan, K., Grouping solvents by statistical analysis of solvents property parameters: implication to polymorph screening, Int*. J. Pharm*., 2004, **283**, 117-125.

Hatherly, P. A., Frasinski, L. J., and Codling, K., Multiphoton ionization of *n*-alkanes using an intense sub-picosecond laser, *Chem. Phys. Lett*., 1988, **149 (5)**, 477-481.

Herbert, P., Charbonier, P., Rivolta, L., Servais, M., Mensch, F., and Campbell, P., The occurrence of chlorinated solvents in the environment, *Chem. and Indus*., 1986, **24**, 861-869.

Herzberg, G., Infrared and Raman Spectra of Polyatomic Molecules: Molecular Spectra and Molecular Structure, 1945, New Jersey London, Chapter 1.

Hinchliffe, A., Molecular modelling for beginners, 2003, Wiley, Chapter 6.

Hua, L., Shen, H., Zhang, C., Cao, Z., and Zang, B., Photodissociation study of 1,2-C_2H_4BrCl at 234 and 267 nm by the ion-velocity imaging technique, *Chem. Phys. Lett*, 2008, **460**, 50-54.

Hubrich, C., and Stuhl, F., Ultraviolet absorption of some halogenated methanes and ethanes of atmospheric interest, *J. Photochem*., 1980, **12**, 93-107.

Le, V., Lasers in chemistry: dye lasers, 2002, available online at http://www.lasalle.edu/academ/chem/laser_web/index.htm. Date of access: 26 May 2008.

Ledingham, K. W. D., and Singhal, R. P., High intensity laser mass spectrometry-a review, *Int. J. Mass. Spec*., 1997, **163**, 149-168.

Livingstone, M., Lasers in chemistry: excimer lasers, 2002, available online at http://www.lasalle.edu/academ/chem/laser_web/index.htm, Date of access: 20 May 2008.

Margulés. L., Carvajal, M., Demaison, J., Rotational spectrum, structure and internal rotation in CH_3CCl_3, *J. Mol. Spec*., 2008, **247**, 160-166.

McMurry, J., Organic chemistry, 2000, Brooks/Cole, Chapter 1 and 12.

McParland, M., 1,1,1-trichloroethane, 1995, IPCSINTOX databank, monograph for UKPID, Date of access: 16 April 2007.

Møller-Plesset perturbation theory (MP), 2007, Wikimedia Foundation, Inc, U.S., available online at [http://en.wikipedia.org/wiki/M%C3%B8ller-Plesset_perturbation_theory]. Date of access: 10 February 2007.

Mullen, C., Huestis, D., Coggiola, M., and Oser, H., Laser photoionization of triacetone triperoxide (TATP) by femtosecond and nanosecond laser pulses, *Int. J. Mass. Spec*., 2006, **252**, 69-72.

Muller, S.R., Zweifel, H. R., Kinnison, D. J., Jacobsen, J. A., Meier, M. A., Ulrich, M. M., Schwarzenbach, R. P., Occurrence source and fate of trichloroacetic acid in Swiss waters, *Environ. Tox. Chem*., 1996, **15**, 1470-1478.

Nayak, A. K., Kurylo, M. J., and Fahr, A., UV absorption cross section of methylchloroform: temperature dependent gas and liquid phase measurements, *J. Geophy. Res*., 1995, **100 (D6)**, 11185-11189.

Osterhold, T. H., Allendorf, M. D., and Melius, C. F., Unimolecular decomposition of methyltrichlorosilane:RRKM calculations, *J. Phys. Chem*.,1994, **98**, 6995-7003.

PBMR Technology Programme, 2008, Femtochemistry and Laser Spectroscopy Research Project, Scope of Research Document 063492.

Pelle, M. B., An investigation into molecular properties of methyltrichlorosilane using laser spectroscopy, 2008, North West University (Dissertation-M.Sc), 104 pages.

Prystupa, D. A., Anderson, A., and Torrie, B. H., Raman and far-infrared study of crystalline 1,1,1,-trichloroethane and 1,1,1-trichloroethane-d_3, *J. Raman Spec*., 1989, **20**, 587-593.

Qtaitat, M. A., and Mohamad, A. B., Spectra and structure of silicon-containing compounds. XVII. vibrational and microwave spectra, molecular structure, barrier to internal rotation and *ab initio* calculations of methyltrichlorosilane, *Mol. Biomol. Spec*., 1994, **50 A**, 621-637.

Rae systems, correction factors, ionization energies, and calibration characteristics, Technical notes, 1993, available online at http://www.afcintl.com/pdf/rae/tn106.pdf. Date of access: 09 May 2008.

Reid, G. D. and Wynne, K., Ultrafast laser technology and spectroscopy, Encyclopedia of analytical chemistry, R.A.Meyer (Ed.), 2000, 13644-13670.

Rozgonyi, T., and Gonzalez, L., Control of the photodissociation of CH_2BrCK using few-cycle IR driving laser pulse and a UV control pulse, *Chem. Phys. Lett*., 2008, **459**, 39-43.

Rush, J. J., Cold-neutron study of hindered rotations in solid and liquid methylchloroform, neopentane, and ethane, *J. Chem. Phys*., 1967, **46**, 2285-2291.

Schlecht, M. F., Molecular modelling on the PC, Wiley-VCH New York, 1998, 1-19.

Siegman, A.E., Lasers, University Science Books, 1986, Chapter 1.

Simon, P. C., Gillotay, D., Vanlaethem-Meuree, N., and Wisemberg, J., Ultraviolet absorption cross-section of chloro and chlorofluoro-methanes at stratospheric temperatures, *J. Atm. Chem*., 1988, **7**, 107-135.

Sittert, C. G. C. E., and Lachmann, G., Molecular modelling, 2007, Potchefstroom, 43 pages (study guide).

Spartan, Getting started with Spartan, Wavefunction, Inc, Irvine, CA (USA) 2004.

Spartan '06 for windows and Linux, Tutorial and User Guide, Wavefunction, Inc, Irvine, CA (USA) 2006.

Steacie E. W. R., Atomic and Free Radical Reactions, Reinhold, New York, 1946.

Stengle, T. R. and Taylor, R. C., Raman spectra and vibrational assignments for 1,1,1-trichloroethane and their deuterium derivatives, *J. Mol. Spec*., 1970, **34**, 33-46.

Stephenson, J. L., and McLuckey, S. A., Ion/ions proton transfer reactions for protein mixture analysis, *Anal. Chem*., 1996, **68**, 4026-4032.

Tanabe, K., and Saeki, S., Calculation of infrared band intensities of various chlorinated ethanes, *Bull. Chem. Soc., Japan*, 1972, **45**, 32-38.

Telle, H. H., Ureña, A. G., and Donovan, R. J., Laser chemistry: spectroscopy, dynamic and applications, 2007, New York: Wiley, Chapter 3 and 4.

Vanlaethem-Meuree, N., Wisemberg, J., Simon, P.C., Ultraviolet absorption spectrum of methylchloroform in the vapor phase, *Geophys. Res. Letters*, 1979, **6**, 451–54.

Venkateswarlu, P., The infrared spectrum of methyl chloroform in the region 1.6μ-20μ, *J. Chem. Phys*., 1951, **19**, 298-302.

Yates, J. R. 3rd, Mass spectrometry and the age of the proteome, *J. Mass Spec*., 1998, **33**, 1-19.

Young, D., Introduction to computational chemistry, Cytoclonal pharmaceutics Inc,. 2001, available online at http://www.cd.net/cca/documents/dyoung/topics-orig/compchem-html. Date of access: 07 March 2007.

Zewail, A. H., laser femtochemistry, *Science, New series*, 1988, **242**, 1645-1653.

http://www.andor.com/leanr/applications/?docid=64, Raman Spectroscopy, Date of access: 28 March 2007.

http://www.raman.de, Fundamentals, technologies, and application of Raman spectroscopy, Date of access: 16 April 2007.

http://en.wikipedia.org/wiki/Bond_length, Bond length. Date of access: 05 May 2007.

http://chemistry.ncssm.edu/book/chap9DFT.pft, A chemistry educator's guide to molecular modeling. Date of access: 10 June 2007.

http://en.wikipedia.org/wiki/Infrared_spectroscopy, Infrared spectroscopy. Date of access: 12 June 2007.

http://www.cem.msu.edu/~reusch/VirtualText/Spectrpy/InfraRed/infrared.htm, Infrared spectroscopy. Date of access: 10 June 2007.

http://teaching.shu.ac.uk/hwb/chemistry/tutorials/molspec/uvvisab1.html, UV-Vis absorption spectroscopy. Date of access: 28 March 2008.

http:www.chemguide.co.uk/analysis/uvvisible/radiation.html, Electromagnetic radiations. Date of access: 21 February 2008.

http://www.chemguide.co.uk/analysis/uvvisible/spectrometer.html, A double beam UV-visible absorption spectrometer. Date of access: 22 February 2008.

http://www.chemguide.co.uk/analysis/uvvisible/bonding.html, Essential bonding theory for UV-visible absorption spectrometry. Date of access: 25 February 2008.

http://www.chemguide.co.uk/analysis/uvvisible/theory.html, UV-visible absorption spectra. Date of access: 26 February 2008.

http://www.chemsoc.org/pdf/LearnNet/rsc/UV_text.pdf, UV/visible spectroscopy. Date of access: 28 March 2007.

http://en.wikipedia.org/wiki/Nd:YAG_laser, Nd:YAG laser. Date of access: 20 May 2008.

http://www.phy.davidson.edu/StuHome/sethvc/Laser-Final/NdYag.htm, The Nd:YAG laser. Date of access: 20 May 2008.

http://en.wikipedia.org/wiki/Dye_laser, Dye laser. Date of access: 20 May 2008.

http://elchem.kaist.ac.kr/vt/chem-ed/ms/tof.htm, Time of flight mass spectrometry. Date of access: 23 May 2008.

http://www.fastcomtec.com, Basics of time of flight mass spectrometry. Date of access: 09 June 2008.

http://www.rp-photonics.com/yag_laser.html, Encyclopedia of laser physics and technology. Date of access: 17 June 2008.

http://www.thefreedictionary.com/time-of-flight+mass+spectroscopy, Time-of-flight mass spectroscopy, *The free dictionary*. Date of access 17 June 2008.